SPACE SCIENCES LABORATORY

[redacted]

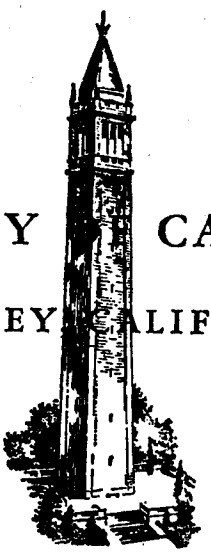

UNIVERSITY OF CALIFORNIA

BERKELEY, CALIFORNIA

Space Sciences Laboratory
University of California
Berkeley, California 94720

RADIATION ANOMALIES ON THE LUNAR SURFACE

by

David Buhl

A Technical Report on NASA Grants
NsG 101-61 and NsG 243-62

Series No. 8, Issue No. 1

Submitted in partial satisfaction
of the requirements for the degree of

DOCTOR OF PHILOSOPHY

Department of Electrical Engineering
University of California, Berkeley

January 20, 1967

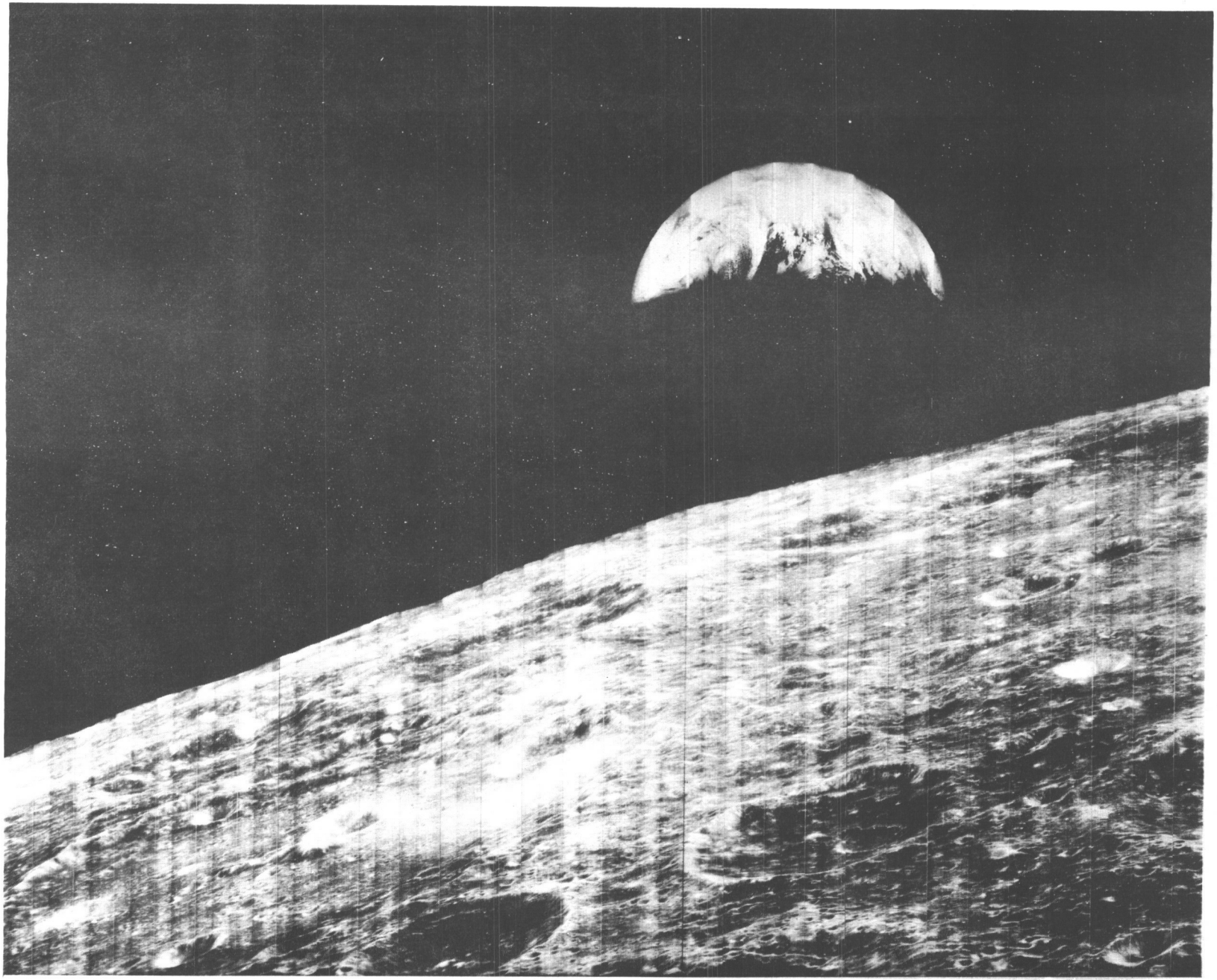

Orbiter I view of lunar landscape (sky and telescope, Dec. 1966)

NASA
L-66-7825

CONTENTS

ILLUSTRATIONS

RADIATION ANOMALIES ON THE LUNAR SURFACE

David Buhl

ABSTRACT

A model of the Moon, which consists of a large number of centimeter and millimeter size craters distributed over the surface, is proposed to account for several of the anomalous results of infrared observations. These observations have shown that the temperature of the subsolar point depends on the angle of observation. In addition, thermal hot spots appear during a lunar eclipse. Such anomalous observations are interpreted as indicating the presence of small craters.

In calculating the effect of small scale cratering on observations of the illuminated and eclipsed Moon, a number of physical processes are considered. A detailed calculation of the effect of radiation interchange within the crater is made. Curves are plotted of the infrared brightness of the illuminated crater as a function of the angle of the observer, taking into account the effects of reradiation, local incidence and emission angles, and shadowing. These curves are shown to be similar to those observed for the Moon. By interpreting the anomalous radiation curves as being the result of small craters a relative crater density of 0.3 and a depth to diameter ratio of approximately 0.5 are obtained for the millimeter scale cratering and roughness on lunar surface. A calculation is also made of the cooling curves for a crater both during an eclipse and during the lunar night. The effects of reradiation within the crater and excavation of heat from the deeper layers are shown to produce an anomalous cooling curve. For example an area which is covered with craters whose depth to diameter ratio is 2.0 will be 70° K warmer than a smooth area during an eclipse. From this it is suggested that centimeter scale craters may be responsible for the observed thermal

anomalies. Several measurements are suggested which would provide more information on the small scale craters. These measurements would also help to eliminate some of the models which have been suggested to explain the thermal anomalies.

ACKNOWLEDGMENTS

The author would particularly like to thank Professor William J. Welch for his many helpful suggestions during the course of the research and for considerable aid in writing this thesis. I am also indebted to Dr. Donald G. Rea for suggesting the original idea and for a number of subsequent stimulating discussions. The help of Professor Diogenes J. Angelakos in reading the manuscript is also acknowledged. During the period of this investigation much encouragement and cheer was provided by my wife, Pauline, and my daughter, Erica. Finally, the cooperation of the Moon during the microwave experiment was greatly appreciated.

I. INTRODUCTION

Photographs and visual observations of the Moon provide much material for speculation about the history of the lunar surface. However, even with the success of orbiting and landing satellites many questions remain to be answered. The resolution of photographs taken with Earth-based telescopes is of the order of a kilometer. Recent satellite pictures that have been transmitted to Earth represent an enormous improvement over telescope photographs; for example, the approximate resolutions for three of the U. S. satellites are: Orbiter (100 m), Ranger (1 m), Surveyor (1 mm). The most striking feature of the Moon's surface as seen in these photographs is the large number of craters on the lunar landscape. This is particularly evident in the pictures taken by the Orbiter satellite. There is some debate about whether these craters are of volcanic or meteorite origin; nevertheless, the evidence from studies of dimensions of the craters strongly suggests that most of the craters have been created by meteorite impacts with the surface (Baldwin 1963). The biggest craters have diameters exceeding 100 km and depths less than 5 km, making them relatively shallow. In many of these craters there appears to have been some filling due to erosion processes (Jaffe 1966). Even the immense dark maria regions are thought to have been large crater basins that were subsequently filled by lava (Baldwin 1963). As an alternative hypothesis, Gold (1955) suggested that the maria are enormous dust flows whose depth might be as much as 300 feet. Recent high-resolution photographs in the region of Flamsteed,

where the Surveyor landed, suggest a fine particle surface that is weakly cohesive; however, little is known about the subsurface. The presence of dust and the possibility of volcanoes on the lunar surface are just two of many problems that have not yet been resolved by recent photographs.

Several statistical studies of lunar craters have been made using lunar photographs. One of the most comprehensive was a study by Baldwin (1963) of the depth, diameter, and rim height of lunar and terrestrial craters. He was able to show that the relationship between depth and diameter for lunar craters is very similar to that for meteorite and explosion craters on Earth. Subsequently, he found that a slight modification was needed in the relationship in order to fit the data on the smaller craters shown in the Ranger photographs (Baldwin 1965). As one goes to smaller and smaller craters the depth-to-diameter ratio increases and the flat bottom shape of the larger craters gives way to a spherical shape (Fig. 2). In addition, the number of craters increases at a rate greater than one over the square of the diameter, so that the percentage of the area of the Moon covered by the craters increases as the crater diameter decreases (Brinkmann 1966). An indirect way of obtaining the possible distribution of crater sizes on the Moon is to do a count of meteorite falls on the Earth. Brown (1960) has shown that the number of meteorites increases very rapidly as the mass decreases. Baldwin (1963) has used these statistics, along with his own studies of the relationship of the mass of the meteorite to the diameter of the crater produced, to derive the distribution of crater diameters. Such a distribution predicts a very

large number of small micrometeorite craters. If such craters exist, many of them must be beyond the present limits of resolution, even for the Ranger and Surveyor satellites. Detecting such small craters and roughness requires a more indirect approach.

A number of investigators have made observations of the intensity of visible light reflected from the lunar surface (Minnaert 1961). In one study the intensity as a function of the angle of reflection was measured by observation of various regions that have the same solar angle of incidence (Fig. 3). In another observation the reflected intensity as a function of the angle of incidence for a single region was observed (Sitinskaja and Sharanov 1952). These measurements of the photometric function show that the reflected intensity is sharply peaked in the direction of illumination. Theoretical and laboratory studies of reflection from various surfaces indicate that very complicated structures are required to produce this strong backscattering (Hapke 1963, Warren 1963, Van Diggelen 1960).

In explaining these structures one must consider the extreme environmental conditions on the Moon. Because the Moon lacks an atmosphere, its surface is subjected to intense ultraviolet radiation from the Sun and continual bombardment by micrometeorites and solar wind particles. Several suggestions have been made as to how such processes could produce the structuring of the surface needed to explain the photometric function. These include: impact melting and cooling, solar wind sputtering, porosity caused by volcanic outgassing, or "fairy castles" built by electrostatic forces between dust grains. Most of these mechanisms produce a very complex

geometrical structure whose dimensions are on the order of a few microns. Because of the small size, we will refer to the scale of these structures as being microscopic. Their complex geometry causes shadowing that results in a reflection characteristic similar to that of the lunar surface. The results of observations of the percent polarization of the reflected sunlight and studies of the Bond albedo of the lunar surface are also an indication of roughness. Thus the visual reflection data on the Moon can be interpreted as the result of an extremely rough surface on a microscopic scale.

One very important area of lunar research was begun in the 1920's when Pettit and Nicholson first made measurements of the infrared emission from the surface. Their measurements were made in the 8 — 12 micron telluric window using a thermocouple detector and a filter consisting of a glass slide and water cell. The infrared radiation from the lunar disc is approximately given by the difference between the readings taken with and without the filter. The equipment was mounted at the focus of the Mt. Wilson 100" telescope and used to detect the thermal emission from the surface during the night and eclipse periods, as well as from the illuminated Moon. In one of the observations Pettit and Nicholson (1930) measured the emission from the subsolar point as a function of the angle of the observer with respect to the surface normal (or direction of incidence). The intensity they measured showed a sharp drop at large observing angles. The observation was subsequently repeated by Sinton (1962), who obtained essentially the same result (Fig. 9a). Pettit and Nicholson also observed the intensity of emission of the full Moon from the center out to the limb. Instead of the expected cosine

variation that would be predicted for a smooth lambert sphere, they found $(\cos \theta)^{\frac{3}{2}}$ for the variation in brightness (Fig. 9b). Pettit and Nicholson made a calculation of a roughness model composed of spheres that gave results somewhat similar to the full Moon data. Another model that consists of rectangular corrugations has been recently proposed by Gear and Bastin (1962), but no calculations were made. The interpretations of the Pettit and Nicholson data have generally involved a qualitative discussion of roughness, but no thorough study of theoretical models has been done as in the case of the photometric data. As a result of their detailed consideration of the absolute calibration of the equipment, they were able to obtain a maximum apparent temperature of 407° K for the subsolar point. Pettit and Nicholson then used their data on the emission from the subsolar point to calculate a temperature of 391° K corresponding to the mean spherical intensity. Later measurements indicate about 389° K (Sinton 1962). Such high values indicate that the subsolar point temperature is determined by a simple balance of absorbed solar radiation and thermal emission. However, any interpretation of the radiation emitted from the subsolar point in terms of a temperature for the Moon should take into account the angular dependence of the emission characteristics observed by Pettit and Nicholson.

Observations of the infrared emission from the Moon's surface were also made during the lunar night and during an eclipse. Pettit and Nicholson made an attempt to measure the midnight temperature of the Moon and obtained an upper limit of 120° K. As the sensitivity of infrared detectors has improved it

has become possible to actually measure the nighttime emission from the lunar surface. Murray and Wildey (1964) have observed the cooling of the Moon at night by making scans across the terminator. These showed an upper limit to the midnight temperature of about 105° K. Subsequent measurements by Low (1966) indicate temperatures that are less than 70° K. This is an extremely low temperature, considering that the subsolar point temperature is about 390° K, and it shows that the lunar surface is a very good insulator. Another important observation that Pettit and Nicholson made was to record the surface temperature during the lunar eclipse of June 14, 1927. As the Earth's shadow passed over the lunar disc, they found that the surface cooled very rapidly to around 180° K and continued to decrease slowly during the totality, which lasted for about 2.5 hours. This demonstrates that the Moon is a good insulator for both transient and long period changes in the solar flux.

It was over 20 years after Pettit and Nicholson observed the temperature variation during a lunar eclipse that Wesselink developed a correct theoretical treatment to explain the eclipse cooling curve. In the absence of sunlight, the heat radiation from the surface is just equal to the flux of the heat from the lunar interior. Thus the calculation of the cooling curve must take into account heat diffusion as well as the non-linear surface radiation. In order to solve this non-linear boundary value problem, Wesselink (1948) assumed a smooth, homogeneous surface for the Moon and developed a numerical method that transformed the diffusion equation into a finite difference equation. The theoretical surface temperature could then be calculated numerically for a lunation by assuming a half-wave sinusoidal

variation for the solar flux. Wesselink also calculated the cooling curve for an eclipse and compared his results with those of Pettit and Nicholson (1930) and Pettit (1940). He showed that the thermal parameter of the surface that controls the amount of cooling is the reciprocal thermal inertia $(k\rho c)^{-\frac{1}{2}}$. When the theoretical cooling curves were compared with the observed eclipse temperatures, very high values for the reciprocal thermal inertia were obtained for the Moon (approximately 1,000, as compared with 20 for ordinary rock). Wesselink also derived a value of 650 from the upper limit of 120° K for the midnight temperature obtained by Pettit and Nicholson. Such a large value for $(k\rho c)^{-\frac{1}{2}}$ indicates either an extremely low thermal conductivity (k) or density (ρ) (or both) for the lunar surface since the specific heat is approximately the same for most materials (0.20 — 0.25 g-ca 1/g° K). Later Jaeger and Harper (1953) showed that the theoretical curves for an eclipse match the data better if a smooth layered surface is used. However this model of a dense base covered by an insulating dust layer conflicts with some of the radio measurements.

A much more comprehensive observation of a lunar eclipse has been made recently by Saari and Shorthill (1963) at 10 — 12 μ. They have been able to make temperature maps of the surface during an eclipse by using a scanning detector (Fig. 20). Some regions of the Moon's surface are observed to cool more slowly than the rest, giving rise to hot spots. These thermal anomalies appear to remain as much as 50° K warmer than the surrounding areas during the eclipse, and are generally associated with craters. In addition, several

maria, such as Mare Humorum, etc. are observed to have a slightly elevated temperature. The associations of the thermal anomaies with various features are given by Shorthill and Saari as (Fudali 1966):

FEATURES	% ANOMALIES ASSOCIATED WITH FEATURE
Rayed craters	19.4
Craters with bright interiors at full moon	41.8
Craters with bright rims at full moon	23.3
Bright areas with much smaller craters	3.6
Bright areas associated with features like ridges	3.9
Bright areas not associated with any features	1.2
Craters not bright at full moon	0.6
Position unidentified or questionable	6.3

The interpretations of the thermal anomalies observed by Shorthill and Saari are somewhat uncertain at the present time. The study by Wesselink shows that the cooling during an eclipse, under the assumption that the surface is essentially plane and has unit emissivity is dependent on the reciprocal thermal inertia $(k \rho c)^{-\frac{1}{2}}$. The Moon in general has a rather high value of $(k \rho c)^{-\frac{1}{2}}$.

To account for the anomalous cooling Saari and Shorthill (1963), Winter (1965, 1966), Fudali (1966), and Bastin (1965) have proposed several possible explanations that are listed here:

1. The bulk material in the neighborhood of the anomaly has a lower value of $(k \rho c)^{-\frac{1}{2}}$ than the surrounding area.
2. The lunar surface consists of a dense substrate covered by a layer of dust, and the dust layer is thinner in the anomalous region.
3. There are steeper slopes in the anomalous regions uncovered by dust, and the exposed bare rock has much lower values of $(k \rho c)^{-\frac{1}{2}}$, lowering the mean value of this quantity over the anomalous region.
4. The surface is composite, consisting of base rocks strewn over an otherwise porous surface in the neighborhood of the anomalies.
5. The surface emissivity is lower near the anomaly.
6. There is subsurface heating in these regions.
7. The surface layers in the anomalous region are more transparent in the infrared, allowing the warmer substrate to radiate.
8. The surface is substantially rougher in the neighborhood of the anomaly than over the surrounding area.

Interpretation 1, an increase in k or ρ for the bulk material in the vicinity of a thermal anomaly, is most generally accepted. Explanation 8, which concerns the effect of surface roughness on the

material making up the thermal anomaly, is an important alternative. Wesselink's study of eclipse cooling assumes the surface to be smooth and homogeneous. Several models have shown that roughness can strongly affect the cooling of an otherwise homogeneous material. Winter (1965) proposed a model, which consisted of infinitely deep cracks in the surface, and calculated cooling curves for his model. Both of these studies indicate that anomalous cooling may possibly be caused by surface roughness. It appears at present that any of the mechanisms suggested could produce the anomalous cooling. Therefore, the exact nature of the thermal anomalies will remain an unsolved problem until some experiment can be devised to discriminate between the various models.

Laboratory simulation and testing of materials yields considerable information on the possible physical composition of the lunar surface. Most of the laboratory studies have tried to simulate the lunar environment. Thermal measurements of the Moon have shown that for the lunar surface layer either the thermal conductivity, density, or both, are very low. To account for this large difference between the lunar surface materials and those ordinarily found on Earth, it has been suggested that the lunar surface materials are porous. Sifting of very fine dust particles under vacuum conditions produces a porous structure with low thermal conductivity (Hapke 1963). Materials with various densities and thermal conductivities have been made by sintering (Glasser and Wechsler 1965).

THERMAL PROPERTIES OF FOAMED AND POWDERED MATERIALS

Material	Porosity	Density[a] (gm/cm^3)	Specific heat ($cal/gm\,^{\circ}C$)	Thermal[b] conductivity ($cal/cm\,sec\,^{\circ}C$)	$(k\rho c)^{-\frac{1}{2}}$ $\left(\frac{cm^2 sec^{\frac{1}{2}}\,^{\circ}C}{cal}\right)$
Pumicite	49	1.27	0.22	140×10^{-6}	160
Basalt lava	25	2.08	0.20	530	68
Sintered perlite (open cells)	88	0.31	0.21	59	510
Perlite, loose 200-μ particles	97	0.08	0.21	5.5	3300
Olivine < 70-μ particles	35	2.0	0.19	3.2	910
Granodiorite < 20-μ particles	63	1.0	0.19	7.2	850

[a] Density measured in air.

[b] Thermal conductivity measured in vacuum $<10^{-4}$ Torr

Under a high vacuum many of these samples can be made to have a reciprocal thermal inertia of about 1,000. However, the porosity varies over a wide range from 35 % for pumice to 88 % for sintered perlite. The porosity is related to the density by:

$$P = 1 - \frac{\rho}{\rho_o}$$

where ρ_o is the density of the parent material. The reciprocal thermal inertia $(k\rho c)^{-\frac{1}{2}}$ for the Moon is well known if one accepts Wesselink's smooth, homogeneous model. The problem is that while we know the product of k and ρ, we do not know their ratio, which is necessary in order to determine them independently. The porosity is related to the density as we have shown. A decrease in density means an increase in porosity. Also, since we have fixed the product of k and ρ, this also means an increase in k. In an indirect way the thermal conductivity gives a measure of the cohesiveness, since a higher conductivity means larger contact or strength between particles. Hence, because we have fixed the value of $(k\rho c)^{-\frac{1}{2}}$, we see that an increase in porosity for the lunar surface also means an increase in cohesiveness.

Some additional information about the material properties of the deeper layers on the Moon can be obtained from microwave measurements. The first observations were done by Piddington and Minnet (1949) at a wavelength of 1.25 cm. Using an antenna with a beam width of 0.75°, they obtained the variation in disk brightness temperature over the period of a lunation. The variation was approximately sinusoidal, with a peak amplitude of about 52° K and a phase delay in the maximum of about 45° with respect to the full moon. Since the radiation in the microwave range is emitted by all the substrate material from the surface down to a depth equal to the electrical skin depth, the measurement reveals temperature information about the subsurface material. Piddington

and Minnet, using a smooth homogeneous lunar surface model similar to Wesselink, showed that both the amplitude and phase shift depend on a parameter δ, the ratio of the electrical skin depth to the thermal depth. The thermal depth, which is the depth of penetration of the thermal wave from the periodically heated lunar surface, is directly related to the diffusivity ($k/\rho c$). Hence if one knew the microwave skin depth, the measurement would then give the value of the diffusivity for the substrate. Infrared measurements have fairly well determined the thermal inertia ($\sqrt{k \rho c}$), so that we can obtain independently the values of k and ρ. This is extremely important in determining the porosity as we have discussed. In Piddington and Minnet's model the microwave phase shift approaches a maximum of 45° when the ratio of electrical to thermal penetration depths approaches infinity. Since they actually observed a delay of 45°, they proposed a more complicated model for the substrate, one in which a surface layer of one kind of material overlies a different material. They found that their data were consistent with a model in which a dust layer less than 1 cm in thickness covers a more dense material.

Since the pioneering work of Piddington and Minnet, many more refined microwave observations and interpretations have been made. Summarizing many of these, Troitsky (1965) and Sinton (1962) concluded that most of the observations are consistent with a homogeneous substrate. In addition, recent measurements of microwave cooling during an eclipse (Welch et al. 1965 , Troitsky 1965) provided information about the composition of the material very

near the lunar surface. For example, Welch et al. calculate from their observations and other data the following probable material parameters:

COMPOSITION OF THE LUNAR SURFACE MATERIAL

WELCH ET AL. 1965

Density (ρ)	0.75	g/cm^3
Conductivity (k)	1.25×10^{-5}	cal/^{o} K cm sec
Heat capacity (c)	0.2	cal/g^{o} K
Reciprocal thermal inertia $(k \rho c)^{-\frac{1}{2}}$	700	$cm^2\ ^{o}K\ sec^{\frac{1}{2}}/cal$
Dielectric constant (ϵ)	2.2	
Porosity	75 %	
Microwave skin depth	43	cm

Like the early models of Piddington and Minnet, these more recent models still take the lunar surface to be smooth. A calculation of the effect of roughness on the observed microwave temperature is needed and might help to resolve the debate between the homogeneous model and the layered model. Another relevant observation is that the variation in brightness temperature at microwave wavelengths has a pole darkening given by $(\cos \theta)^{\frac{1}{2}}$, whereas one would expect

it to be $(\cos \theta)^{\frac{1}{4}}$ if the surface were a regular Lambert law surface. No explanations for this effect have been given.

The determination of the dielectric constant of the Moon is one of the important results of radio observations. These are the only observations that permit determination of the density independently of the thermal inertia. The Russian investigations have been summarized by Troitsky (1965), who obtains a probably value of $\epsilon = 1.5$ from several types of measurements. In one study, for example, the center-to-limb variation of the polarization of the radio emission was studied and interpreted in terms of the Fresnel coefficients for a slightly rough surface. Depending on the roughness model used, dielectric constants ranging from 1.1 to 2.0 are obtained (Rea and Welch, 1963). Assuming that the surface is basically silicate rocks, a dielectric constant of 1.5 yields a density of $\rho = 0.5$ (g/cc), which indicates a porosity of about 80 %. Radar determinations of dielectric constant give higher values ($\epsilon \cong 2.8$) (Pettengill and Henry 1962a). Again the choice of model for the surface roughness influences the derived dielectric constant (Rea et al. 1964), but the values obtained are generally higher than those derived from passive observations. Troitsky (1965) finds an average $\epsilon = 2.25$ from a large number of radar measurements, giving a density of $\rho = 1.0$ (g/cc), at least for the deep layers.

Many radar observations have been primarily concerned with characterizing the roughness of the lunar surface. By plotting the radar returns as a function of the delay, one obtains

the amount of reflection in the direction of the source as a function of the tilt of the surface. Using a gaussian distribution for heights and an exponential autocorrelation function to represent the centimeter scale roughness of the Moon's surface, Evans and Pettengill (1963) have obtained an average slope of 1 in 7 from 3.6 cm radar returns. Rea et al. (1964) used geometrical optics to obtain the slope function directly from 68 cm radar data. They found the average slope to be between 11° (1:5) and 14° (1:4). Most of the roughness on the Moon appears to be due to cratering. Hence the Moon's surface appears to have an average depth-to-diameter of about 1:10 for the roughness at a scale in the range 10 — 100 cm.

High-resolution radar studies (Pettengill and Henry 1962b) have shown that the rayed craters Tycho and Copernicus return radar echoes many times more effectively than their surroundings. This has been interpreted as evidence of more dense materials in these craters. This would agree with the idea advanced by Saari and Shorthill (1963) that the thermal anomalies associated with these craters have a lower value of $(k \rho c)^{-\frac{1}{2}}$ for the bulk material. An alternative interpretation of the radar data is that these craters are rougher than their surroundings. To date no single observation has been made that clearly distinguishes between the alternatives of varying roughness or varying density of the lunar surface.

Although in the years since the first observations of Pettit and Nicholson, a great deal has been learned about the physical nature of the Moon, many uncertainties remain in the interpretations of the various observations. A number of discrepancies

exist among the results of the various studies, as for example between the bulk dielectric constant as determined by radiometric and radar studies, and there are competing explanations for some phenomena, such as the thermal anomalies observed by Shorthill and Saari during an eclipse. We suggest that a poor understanding of the effect of roughness of the lunar surface may lie at the root of many of these uncertainties, and we wish to propose a specific model for the roughness to explain some of the observed phenomena, particularly those observed in the infrared.

II. PROPOSAL

1. A Study of the Effects of Lunar Cratering on Infrared Observations

The anomalous infrared measurements of the Moon have been interpreted by a number of authors as being the result of roughness on the lunar surface. Pettit and Nicholson (1930) and Gear and Bastin (1962) suggested this as an explanation for the peculiar infrared emission pattern of the illuminated Moon. The anomalous cooling curve during a lunar eclipse for some of the bright rayed craters has also been interpreted as being due to an increase in roughness in the crater (Winter 1965, and Bastin 1965). Most of the evidence indicates that the roughness of the lunar surface is primarily due to meteorite craters. As has been indicated here, the smaller craters have a larger depth-to-diameter ratio and also are much more numerous. Hence, micrometeorite craters may have a large effect on the infrared measurements.

In this study the effects of small-scale cratering on the emission from the illuminated and dark Moon will be investigated. When illuminated by the Sun, these craters will have temperature variations in them due to local geometry. This is contrary to the usual assumption of a uniform temperature over a small region. Such a non-uniform temperature distribution will produce anomalous radiation patterns. Hence for the illuminated Moon, the effect of cratering may be an important factor in interpreting the measurements of Pettit and Nicholson. During an eclipse there are two physical processes to consider. A deep crater will be heated by its own infrared radiation causing an elevation in

temperature. In addition, there is excavation of heat because the crater exposes deeper layers. The combination of these two will result in an anomalous cooling curve, which may possibly explain the thermal anomalies observed by Shorthill and Saari. As will be shown, the small meteor craters have an important effect on the infrared emission characteristics of the Moon.

III. THEORETICAL ANALYSIS

1. Model of a Cratered Lunar Surface

1.1 Description of a Model Lunar Crater

The shape of the shadow boundary for the smaller craters that can be seen in the Ranger photographs indicates an approximately spherical geometry. From this evidence and studies made of the Surveyor photographs, it has been proposed that the craters are the result of a high-velocity impact in a homogeneous non-cohesive medium (Gault 1966). Hence most of the lunar craters appear to be of meteorite origin. For this study the shape of a lunar crater has been taken to be a section of a sphere. This represents a good physical approximation, as well as making an exact mathematical solution possible. The parameter that is used in our model of a lunar crater is the depth-to-diameter ratio, since the absolute size of the crater does not enter into the mathematics of the solution. In order to define the spherical section that represents the crater, the angle subtended by the crater at the center of the sphere has been chosen, the angle increasing as the crater gets deeper. Hence a hemispherical crater subtends 180° and has a depth-to-diameter ratio of $\frac{1}{2}$ (Fig. 1). The crater angle is related to the depth-to-diameter ratio by

$$d/D = \frac{1 - \cos \gamma/2}{2 \sin \gamma/2} \qquad (1)$$

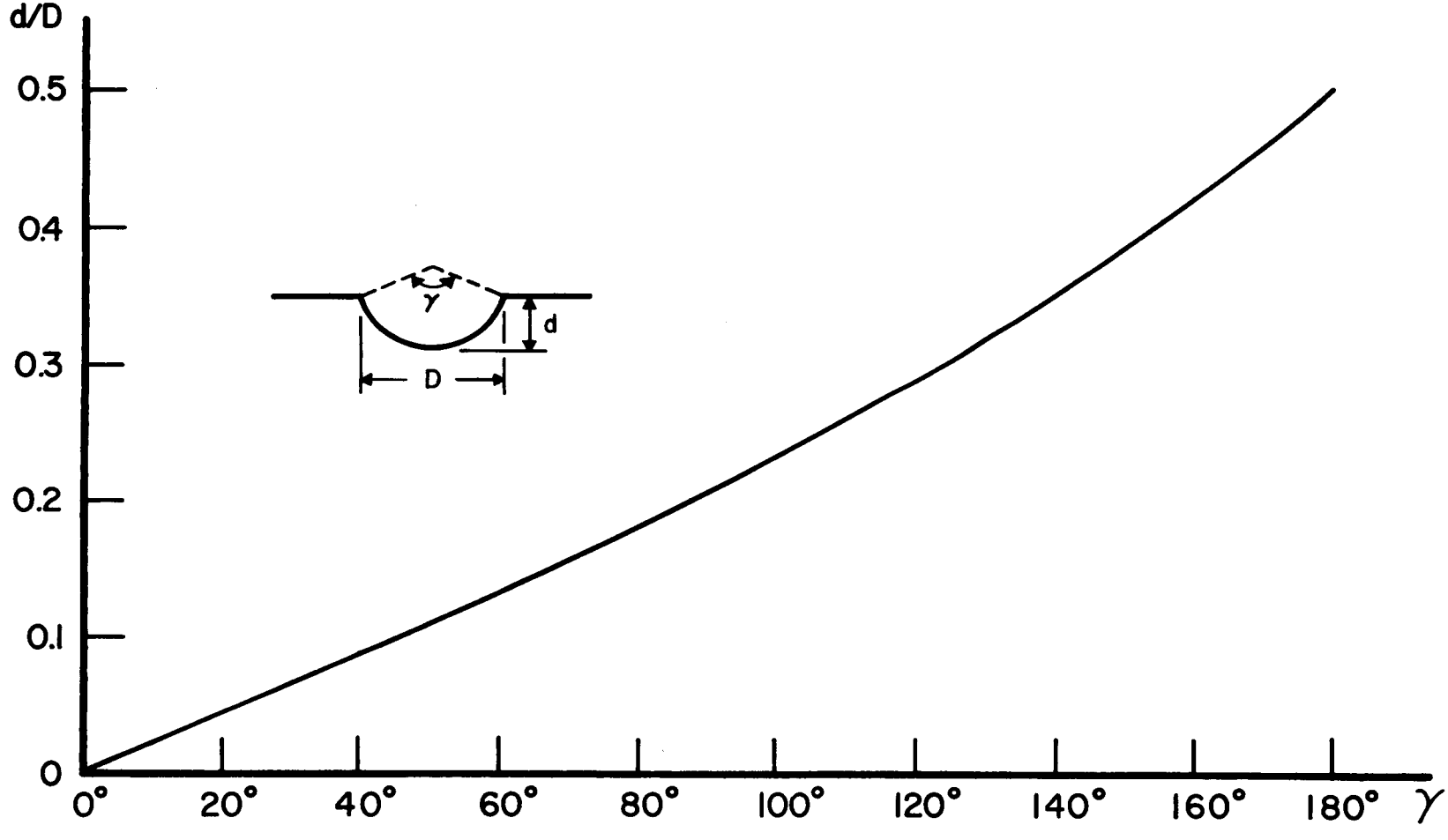

FIGURE I

DEPTH TO DIAMETER RATIO
FOR A SPHERICAL CRATER

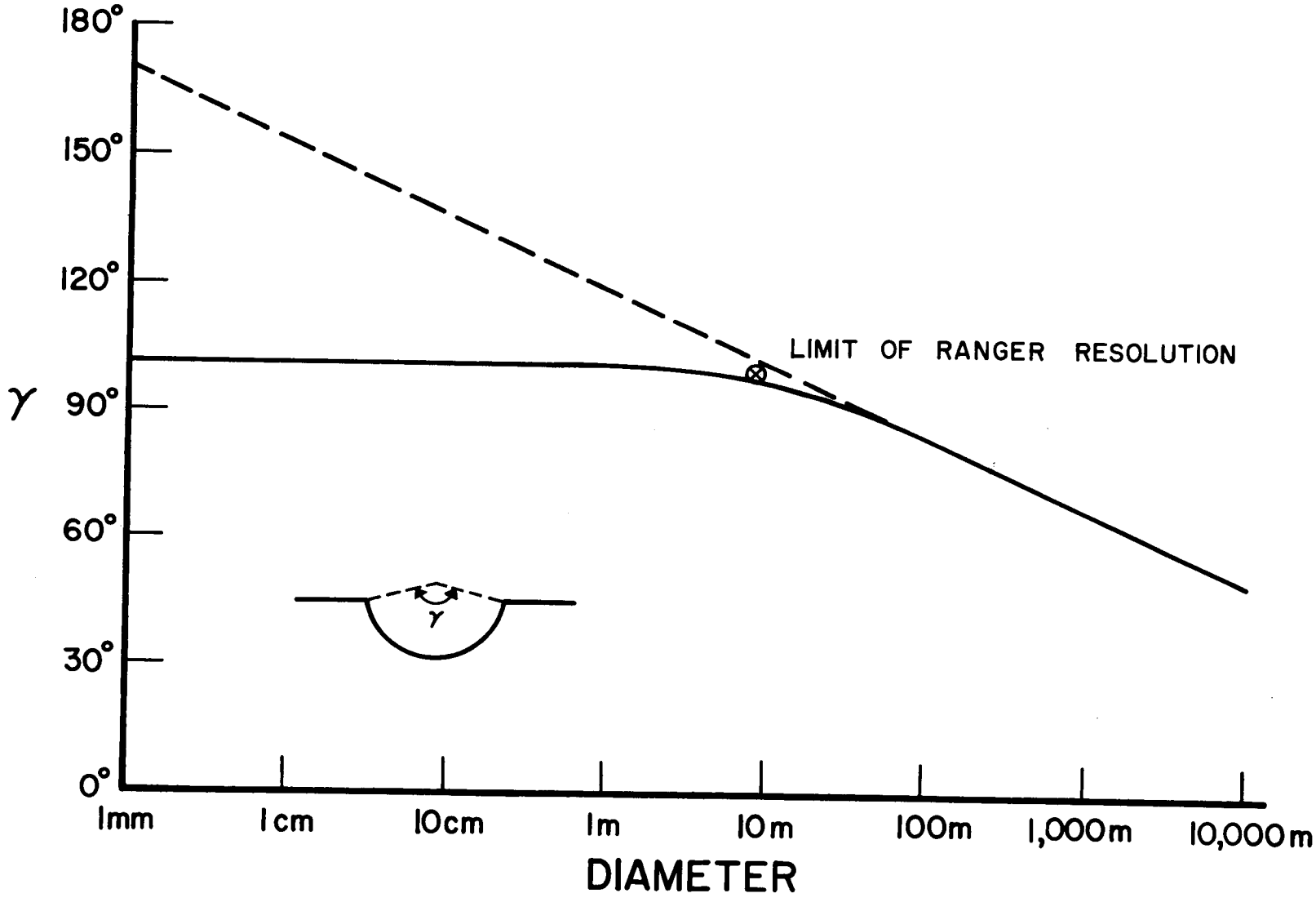

FIGURE 2
DATA ON LUNAR CRATERS (BALDWIN 1965)

From a study of lunar and terrestrial meteor craters Baldwin (1965) was able to derive an empirical relationship between depth and diameter for a lunar crater. This relation, which has been plotted in Fig. 2, indicates the the depth-to-diameter ratio or crater angle increases as the diameter of the crater decreases. In the smaller craters one reaches a limit and craters with diameters less than a few meters apparently all have the same depth-to-diameter ratio. It is interesting that the limit of resolution for the Ranger photographs occurs right at the breakpoint in the curve. If one extrapolates the linear slope of the curve to very small diameters, one obtains hemispherical craters at a diameter of about 1 mm. The data for the craters whose diameters are less than the limit of the Ranger resolution were obtained from explosion craters on the Earth. One reason for the lack of any increase in crater angle above 100° for craters less than a few meters in diameter may be the slumping of material after the crater is formed. The angle of repose on the Earth is between 30° and 40° (Baldwin 1963). Since this is about the average slope for a 100° crater, one would not expect to be able to form a deeper crater in loose material on the Earth. This factor may have an effect on the formation of the smaller craters on the Moon, where the angle of repose is probably larger than on the Earth.

It is also possible that the small lunar craters are deeper than those made in the Earth because the surface material may be entirely different. Experiments with high-velocity impacts show that very deep craters can be formed in porous cohesive material

(Gault 1966). There is some evidence that the lunar surface is very porous (Troitsky 1964 and Kuiper 1966). In one Surveyor photograph there is a clear picture of a practically vertical hole made by the footpad during the landing. Although the spacecraft did not approach the surface with the same velocity as a meteorite, it is interesting that one can produce a steep-walled crater in lunar material. As a result one might expect to find craters with large depth-to-diameter ratios on the Moon. One of the parameters to be determined by our study is the depth-to-diameter ratio or crater angle γ for the small-scale lunar craters.

1.2 Assumptions Made Concerning the Surface of a Crater

The reflection, absorption, and emission characteristics of each element of area in the crater are assumed to be isotropic. This is on the scale of a few microns, which will be referred to as the microscopic scale of the crater. Such an approximation is equivalent to saying that the individual surface elements obey Lambert's law, i.e. the absorption of radiation is proportional to the cosine of the angle of incidence, and the reflection and emission of radiation are proportional to the cosine of the angle of the observer with respect to the local surface normal:

$$I_r \sim I_i \cos\theta_i \cos\theta_r$$

where

I_i = intensity of the incident flux

I_r = intensity of the reflected or reradiated flux

θ_i = angle of incidence

θ_r = angle of reflection or emission

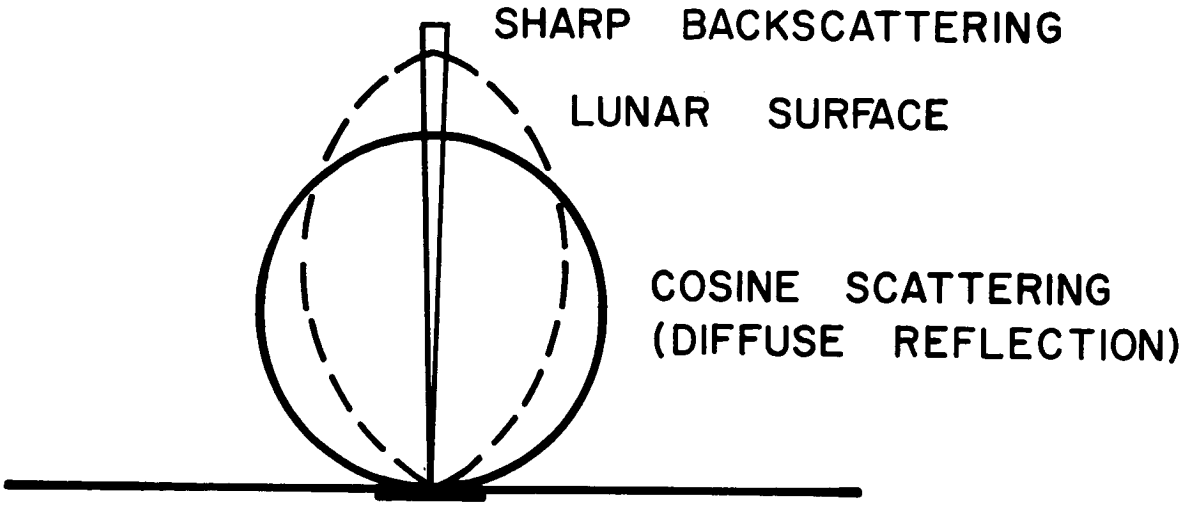

APPROXIMATIONS TO THE LUNAR PHOTOMETRIC FUNCTION

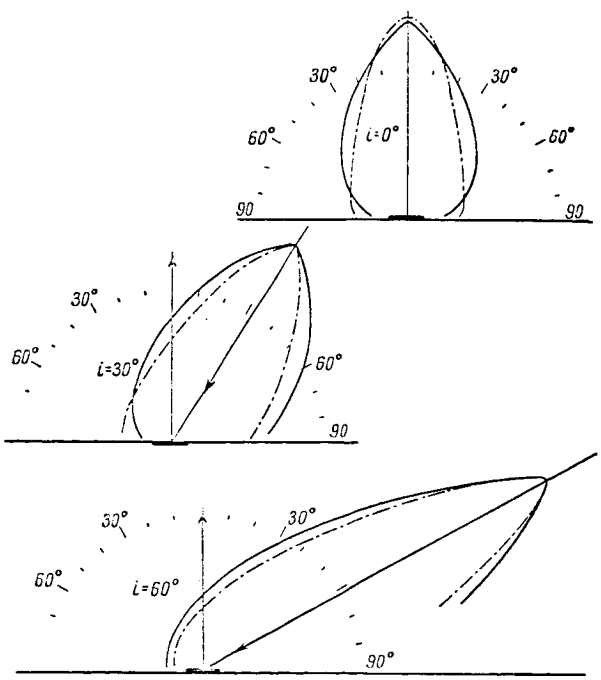

Indicatrices of reflection for the lunar maria (dashed lines) and terrae (solid lines). These are polar plots of the radiation scattered at various angles for fixed angles of incidence. The points chosen were on the lunar equator. The angle of incidence is denoted by *i*.
(After ORLOVA, 1956).

FIGURE 3

OPTICAL BACKSCATTERING FOR THE MOON

The assumption has been made that the microscopic behavior of the individual surface element is isotropic. In fact the Moon's surface deviates somewhat from the cosine reflection law due to the optical backscattering (Fig. 3), but a cosine approximation is sufficient since the amount of reflected light is very small (Appendix I). The Bond albedo (total reflected light integrated over a hemisphere/incident light) is taken as 0.1, a mean value for the Moon's surface (Harris 1961 and Minnaert 1961). The infrared albedo is taken to be zero. This introduces at most a small error since the infrared albedo is, in general, smaller than the optical albedo. The emissivity of the surface is thus assumed to be 1.0 in the infrared. On a larger macroscopic scale, it is assumed that the dimensions of the crater are sufficiently large that geometric optics can be used.

The heat conducted into the deeper layers is assumed to flow normal to the local surface. This approximation breaks down only for very small craters. To determine the limiting size for which the approximation is valid one must calculate the tangential flux for both the illuminated and dark crater. This will be discussed in detail in Sections 3.8 and 4.5.

1.3 Consideration of Radiation and Reradiation in a Lunar Crater

In describing the behavior of a crater on the lunar surface, one must take account of a number of factors. The theory developed must be valid for the day and night periods of a lunation as well as capable of prediciting the transient response of the crater during

a lunar eclipse. This requires the inclusion of the effect of heat conducted between the surface and the deeper layers, which, while negligible during the illuminated periods, is dominant on the dark side or during an eclipse. The Wesselink method of making a finite difference diffusion calculation is well suited for solving this latter problem numerically.

Consider a spherical lunar crater that is illuminated by the Sun (Fig. 5). The amount of solar flux received by an element of area in the crater is proportional to the cosine of the angle of incidence with respect to the local surface normal. For an albedo of 0.1, 10 % of this flux is reflected and the rest of it is absorbed. The absorbed energy is in turn emitted from the surface as thermal radiation except for a small amount that is conducted down into the surface. At night the heat is conducted up from the deeper layers and radiated out of the surface as thermal radiation. This process is then repeated in the next lunation. Due to the shape of the crater, certain regions will be in shadow for part of the day and hence receive no direct insolation. It is clear that each point in the crater receives a different illumination as a function of time. Therefore the calculation of the temperature history of a point in the crater must take into account the effects of shadowing and local incidence angle. In addition, during an eclipse all parts of the crater will experience an attenuation of the solar flux as the Earth passes in front of the Sun.

In setting up the problem, the radiation interchange within the crater must be studied in detail. There are two processes that will be considered. Both of these involve the absorption of

radiation from other parts of the crater. The most important effect is that some of the infrared radiation emitted by an element of area in the crater is intercepted by the rest of the crater. Thus the flux absorbed at a point has a term that is a function of the amount of infrared radiation being emitted by all other points in the crater in addition to the direct solar flux term. A smaller effect is produced by the multiple reflection of the solar radiation within the crater. However, this optical reflection is very quickly absorbed due to the low visual albedo (0.1). It has been assumed that both the processes of emission and diffuse reflection have a cosine dependence. Since they have the same functional dependence, they will have the same spatial distribution throughout the crater. In the process of multiple reflection most of the visible radiation is converted into infrared radiation by absorption and re-emission. As a result the crater is unable to distinguish between the two, and hence both will be referred to as the reradiation flux term.

To show this in detail an area of the crater illuminated by the Sun will be considered (Appendix I). Neglecting the amount of flux that is conducted down into the surface, 90% of the solar flux is absorbed and then radiated away from the surface in the infrared, while 10% is reflected in the visible. A fraction of this reradiation flux will be intercepted in some other region of the crater where all of the infrared flux will be absorbed since it has been assumed that the infrared albedo is zero. Again 90 % of the optical flux will be absorbed and 10 % reflected, however the optical flux is only 10 % of the total reradiation flux. Hence, 99 %

of the total reradiation flux is absorbed. What has been shown here is that for each element of area the amount of direct solar radiation absorbed is reduced by 10 % due to the albedo, while the amount of reradiation flux absorbed is only reduced by 1 %, i.e. the square of the albedo. The main effect of the albedo on the reradiation is to change the ratio of the visible component to the infrared component. It has been demonstrated here that reradiation within a crater is virtually independent of the value of the surface albedo when the albedo is small. This is general, and it does not depend on the shape of the lunar crater.

1.4 Density of Lunar Craters

As an approximation to the actual small scale lunar surface, one can imagine that the Moon is covered by a large number of spherical craters distributed at random across a flat surface. The fraction of the area which is covered by such craters is defined as the relative crater density. The relative crater density can be expressed as:

Relative Crater Density + Density of Flat Area = 1.0

Hence we have made a model of the lunar surface which consists of a certain density of spherical craters with constant depth to diameter ratio spread out across an otherwise flat surface. The two parameters of this model are the depth to diameter ratio (or crater angle) and the relative crater density. There will be some statistical distribution of these two parameters which will vary from point to point. The full Moon and subsolar point measurements of Petit and Nicholson represent an average of the surface characteristics because each data point is

is taken from a different part of the surface. This suggests that the data contains information on the average statistical distribution of crater angles and density. The parameters we have chosen each represent a mean value for the distribution. This is obviously an idealization, however it provides as elaborate an indication of the small scale lunar surface as can be obtained with present data.

In this study of the behavior of a crater on the lunar surface, a number of physical processes are considered. During half of the lunation the crater is illuminated directly by the Sun. In determining the intensity of the isolation, the effects of local incidence angle, shadowing, and albedo are important. Accounting for the flux conducted down into the surface is necessary in giving the dark side behavior of the crater. In addition a large amount of flux within the crater is due to the effects of reradiation. In the following sections a theory will be developed that will describe the temperature and radiation in a lunar crater consistent with the physical processes that have been discussed.

2. Mathematical Analysis of the Temperature Distribution

2.1 The Integral Equation for a Spherical Crater

One of the important effects that we have discussed concerns the radiation interchange within a lunar crater. Essentially this reradiation represents the interaction between various parts of the crater. The mathematical statement of a problem involving radiation interchange is an integral equation. The solution to such an integral equation will then describe the balance of radiation in a lunar crater. There are a number of physical processes that must be accounted for in setting up the integral equation. The flux balance at an element of surface area in the crater is shown in Figs. 4 and 5. The amount of incident solar flux that is reflected by the element of area is determined by the albedo. In addition to the solar flux there is a certain amount of reradiation flux illuminating the element of area. We have discussed the assumption that, while all of the reradiation flux is absorbed, only a fraction of the solar flux, equal to one minus the albedo, is absorbed (Appendix I). Conservation of energy requires that all of the energy absorbed must be either conducted into the surface or emitted as thermal radiation in the infra-red. This can be expressed as a flux balance for the element of area as follows:

$$\sigma T^4 = (1 - a) f_s \cos \psi + f_r + f_c \quad \text{Illuminated region}$$

$$\sigma T^4 = f_r + f_c \quad \text{Dark or shadowed region} \qquad (2)$$

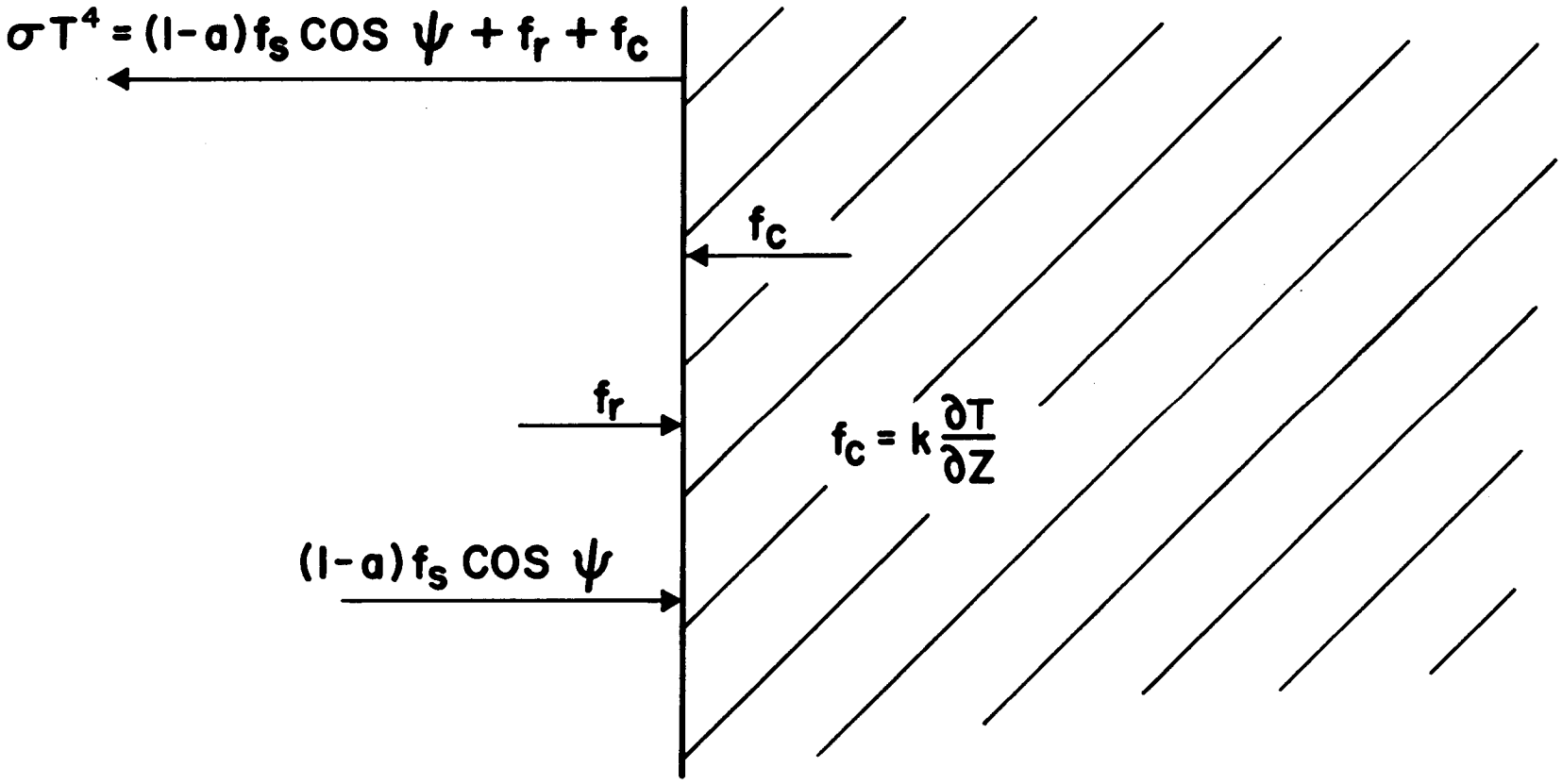

FIGURE 4

FLUX BALANCE AT AN ELEMENT OF SURFACE IN THE CRATER

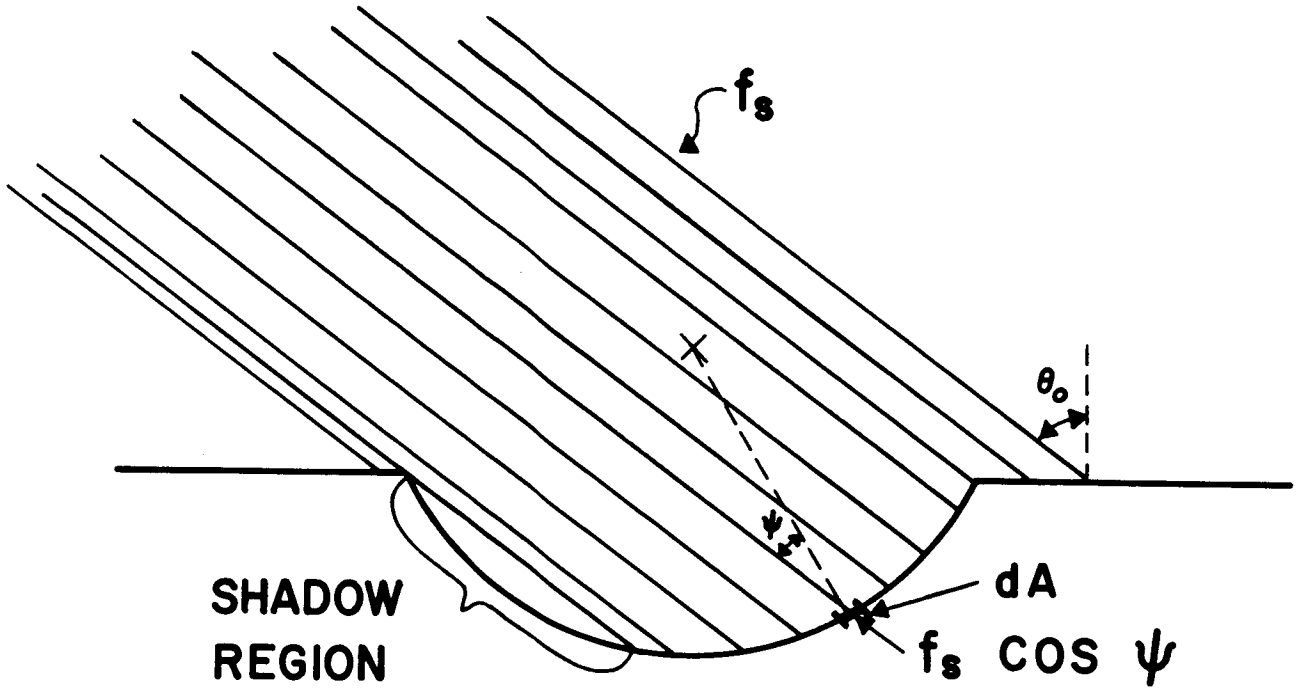

FIGURE 5

SOLAR FLUX INCIDENT
ON A SPHERICAL CRATER

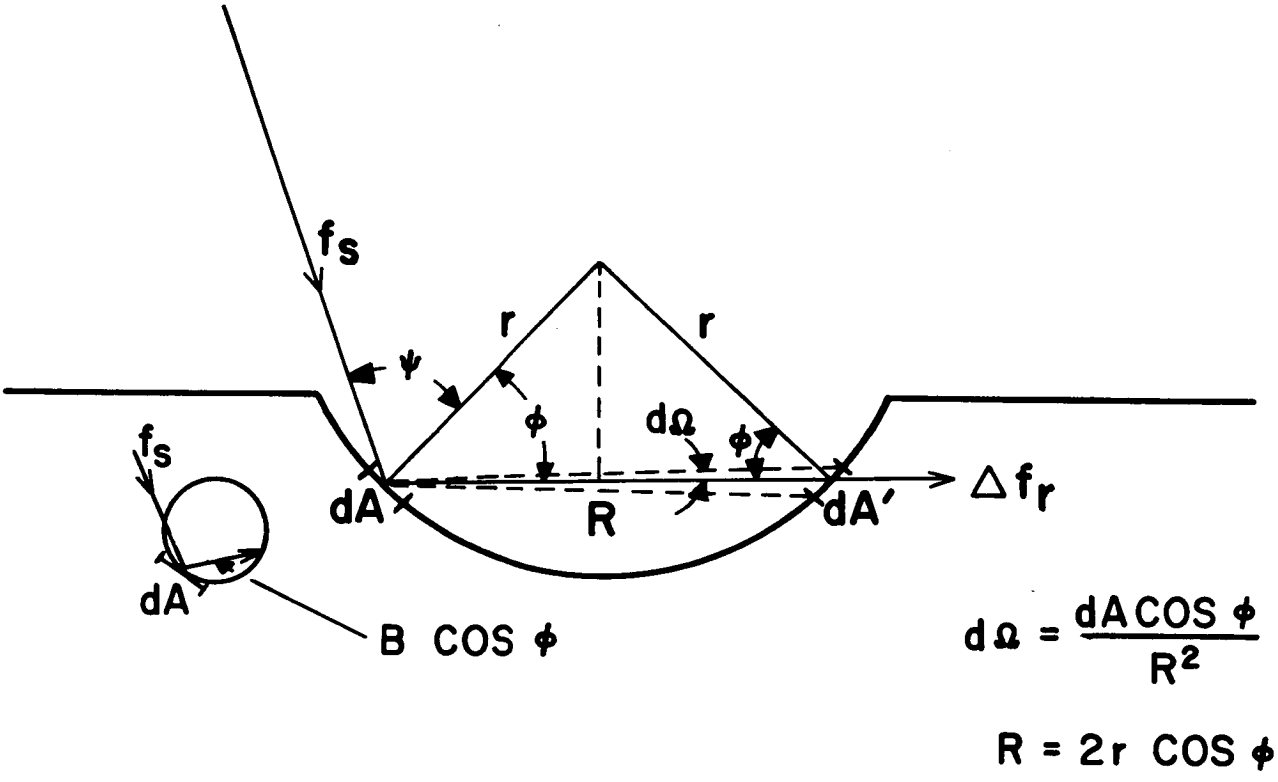

FIGURE 6
GEOMETRY FOR CALCULATING
RERADIATION FLUX AT dA'

where:

σ	=	Stefan Boltzman constant = 1.36×10^{-12} g cal/cm^2 sec$^{\circ}$ K^4
T	=	Temperature of the element of area
a	=	Visual albedo = 0.1
f_s	=	Solar constant = 0.033 g cal/cm^2 sec
f_r	=	Reradiation flux
f_c	=	Conducted flux
ψ	=	Incidence angle with respect to local surface normal

Thus the temperature of a point within the crater is dependent on three quantities: the direct solar illumination, the reradiation flux and the conducted flux.

In order to calculate the infrared reradiation flux we consider an element dA radiating into an element dA′ (Fig. 6). The flux from dA is assumed to radiate in a cosine pattern about the surface normal. From the spherical geometry chosen for the crater it is obvious that the normal to the surface is just the radius of the sphere that passes through dA. For any two arbitrary points dA and dA′ on the sphere defining the crater we consider the plane containing dA, dA′, and the center of the sphere. In this plane the two radii that are the surface normals to dA and dA′ then form an isosceles triangle with the chord that connects the two areas. This triangle has two sides equal to r, the radius of the sphere, and two equal angles that we call ϕ. Note that ϕ is also the angle of the reradiation flux with respect to the local surface normals of dA and dA′. The third side of the triangle is R, the distance between the two elements of area, and simple trigonometry shows that:

$$R = 2 r \cos \phi \tag{3}$$

The brightness of the area dA is related to its temperature by:

$$B = \frac{1}{\pi} \sigma T^4 \qquad \frac{g\ cal}{cm^2\ sec\ steradian} \tag{4}$$

To find the amount of power radiated from dA to dA′, we must multiply this brightness by the cosine of the angle of emission, the solid angle subtended by dA′, and the element of area dA.

$$dP = B \cos \phi \ d\Omega \ dA \tag{5}$$

The infrared reradiation flux at dA′ is then just this power divided by the element of area dA′:

$$\Delta f_r = \frac{dP}{dA'} = B \cos \phi \ \frac{d\Omega \ dA}{dA'} \tag{6}$$

It should be emphasized that we are only calculating the infrared component of the reradiation. By definition the incremental solid angle $d\Omega$ is the projection of the area dA′ in the plane perpendicular to R divided by the square of the distance, i.e.

$$d\Omega = \frac{dA' \cos \phi}{R^2} \tag{7}$$

We can now write the reradiation flux from dA by using Eq. 4 for B, Eq. 7 for $d\Omega$, and Eq. 3 for R, which when substituted into Eq. 6 gives:

$$\Delta f_r = \frac{\sigma T^4 \cos\phi}{\pi} \quad \frac{dA' \cos\phi \, dA}{(2 r \cos\phi)^2 \, dA'}$$

$$\Delta f_r = \frac{\sigma T^4}{4\pi r^2} \, dA \tag{8}$$

Note that the cosine of the angle ϕ has dropped out of the expression for the reradiation flux indicating that the amount of reradiation flux from dA depends only on the temperature of dA and not on its position in the crater or distance from dA′. This simplification is a direct result of the spherical shape of the crater and allows us to obtain an exact solution for the reradiation term. The contribution of the reradiation flux at dA′ from the entire crater can be obtained by integrating the amount of flux from the arbitrary area dA. Thus the reradiation term is just the integral over the crater floor of Eq. 8,

$$f_r = \int_{A_c} \frac{\sigma T^4 (\theta, \phi)}{4\pi r^2} \, dA \tag{9}$$

A_c = Crater floor area (Appendix II)

(θ, ϕ) = Spherical coordinates giving position on the crater surface

where only T is a function of position within the crater.

Substituting the expression for the infrared reradiation flux (Eq. 9) back into the original flux balance relation (Eq. 2), we obtain the integral equation for the temperature distribution in the crater:

$$\sigma T^4 = (1 - a)\, f_s \cos\psi + \frac{\sigma}{4\pi r^2} \int_{A_c} T^4\, dA + f_c \quad \text{Illuminated region}$$

$$\sigma T^4 = \frac{\sigma}{4\pi r^2} \int_{A_c} T^4\, dA + f_c \quad \text{Dark or shadowed region} \tag{10}$$

The reradiation term can be seen to be independent of position within the crater, being only a function of the integral or average of the fourth power of the temperature. Hence, the reradiation flux is constant throughout the crater resulting in a rather unique form of integral equation for the temperature in which the kernel is unity. This is due to the spherical geometry chosen for the crater. A cylindrical structure (Eq. 36) or other shape would require a much more complex integral equation.

2.2 Equations Describing the Temperature History of a Crater

In solving the integral equation it is useful to define a symbol representing the integration over the crater surface. Therefore we will use a bar over a quantity to indicate a spatial average over the crater:

$$\overline{T^4} \equiv \frac{1}{A_c} \int_{A_c} T^4\, dA$$

$$A_c = \int_{A_c} dA = \text{crater floor area} \tag{11}$$

Note that this is not the average temperature to the fourth power but the average of the fourth power of the temperature. With this notation the integral equation becomes

$$\sigma T^4 = (1 - a) f_s \cos \psi + C\sigma \overline{T^4} + f_c \quad \text{Illuminated region}$$

$$\sigma T^4 = C\sigma \overline{T^4} + f_c \quad \text{Dark or shadowed region} \tag{12}$$

where:

$$C = \frac{A_c}{4\pi r^2} \quad \text{(Appendix II)}$$

It should be emphasized here that while the temperature varies for different positions within the crater the reradiation term is not a function of position within the crater. Hence it is possible to integrate the integral equation over the crater floor. The integral of the reradiation term is just the integral of a constant and therefore it can be removed from underneath the integral sign:

$$\int_{A_c} \sigma T^4 \, dA = \int_{A_c} (1 - a) f_s \cos \psi \, dA + C\sigma \overline{T^4} \int_{A_c} dA + \int_{A_c} f_c \, dA \quad \text{Illuminated or shadowed region}$$

$$\int_{A_c} \sigma T^4 \, dA = C\sigma \overline{T^4} \int_{A_c} dA + \int_{A_c} f_c \, dA \quad \text{Dark region} \tag{13}$$

Having integrated the flux balance relation (Eq. 2) over the crater surface, we must realize that the first of Eq. 13 applies to the entire crater during the lunar day and the second equation applies during the

lunar night. The lefthand side of the equation contains the average fourth power of the temperature discussed previously. The last term on the right is a similar spatial average. In performing the integral of the solar flux term we must be careful to realize that the solar flux is zero in the shadowed region. In addition, if we consider that cos ψ dA is the projected element of area of the crater floor in the direction of the incident solar flux, it is obvious that the integral of this area over the illuminated region times the solar constant is just the total power entering the crater (Fig. 5).

$$\int_{A_c} f_s \cos \psi \, dA = f_s A_a \cos \theta_o = P \tag{14}$$

where:

A_a = Aperture or crater opening area (Appendix II)

θ_o = Incidence angle on a flat area with respect to the local surface normal

P = Solar power entering the crater

Using our previous notation we can rewrite Eq. 13 in the following form:

$$\sigma \overline{T^4} A_c = (1 - a) f_s \cos \theta_o A_a + C\sigma \overline{T^4} A_c + \overline{f}_c A_c \quad \text{Illuminated region} \tag{15}$$

$$\sigma \overline{T^4} A_c = C\sigma \overline{T^4} A_c + \overline{f}_c A_c \quad \text{Dark region}$$

Dividing by A_c and collecting terms we have:

$$\sigma\,\overline{T^4}\,(1 - C) = (1 - a)\, f_s \cos\theta_o \,\frac{A_a}{A_c} + \bar{f}_c \quad \text{Illuminated region}$$

$$\sigma\,\overline{T^4}\,(1 - C) = \bar{f}_c \quad \text{Dark region} \tag{16}$$

Some trigometric integration will show that for a sphere (Appendix II):

$$\frac{A_a}{A_c} = \left(1 - \frac{A_c}{4\pi r^2}\right) = (1 - C) \tag{17}$$

Hence substituting this in Eq. 16 and dividing by $\frac{A_a}{A_c}$ we finally obtain:

$$\sigma\,\overline{T^4} = (1 - a)\, f_s \cos\theta_o + \frac{A_c}{A_a}\,\bar{f}_c \quad \text{Illuminated or shadowed region}$$

$$\sigma\,\overline{T^4} = \frac{A_c}{A_a}\,\bar{f}_c \qquad \text{Dark region} \tag{18}$$

Note that:

$$f_r = C\,\sigma\overline{T^4}$$

Therefore, what we have obtained in integrating the integral equation is an expression for the reradiation flux in the crater. It is important to point out that this represents only the infrared component of the reradiation. Thus Eq. 18 corresponds to the case where only infrared reradiation is present. There would be no visible component if all the relected solar flux were very sharply backscattered out of the crater and did not intersect the walls of the crater. However, the actual reflection function is better approximated by the Lambert cosine law. We have shown that with a cosine law reflection the total reradiation flux is virtually independent of the visual albedo (Appendix I).

This has the effect of removing the (1 — a) factor from Eq. 18 when we consider both the visible and infrared components to the radiation. Thus the reradiation expression for cosine law reflection is:

$$\sigma \overline{T^4} = f_s \cos\theta_o + \frac{A_c}{A_a} \bar{f}_c \quad \text{Illuminated or shadowed region}$$

$$\sigma T^4 = \frac{A_c}{A_a} \bar{f}_c \quad \text{Dark region} \tag{19}$$

The relations that we have derived describe the radiation balance at the surface of the crater. In order to account for the flux conducted down into the surface we must consider the heat diffusion equation:

$$\nabla^2 T - \frac{1}{K} \frac{dT}{dt} = 0$$

$$K = \frac{k}{\rho c} \tag{20}$$

where K is the diffusivity. In addition we need the relation between the flux and temperature for a bulk material:

$$f = k \nabla T \tag{21}$$

We will assume a one-dimensional diffusion problem with the heat flux flowing perpendicular to the local surface. The Wesselink procedure is appropriate for solving this type of diffusion problem on a computer. The equations necessary for describing the complete

temperature history of a crater are the integral equation (Eq. 12), the expression for the reradiation flux (Eq. 19), the diffusion equation (Eq. 20), and the conductivity relation (Eq. 21). We summarize these again to emphasize their importance. (Note that Eqs. 22a and b apply to the illuminated region, Eqs. b and c to the shadow region, and Eqs. c and d to the dark region.)

$$\sigma T^4 = (1 - a)\, f_s \cos\psi + C\sigma\overline{T^4} + f_c \quad \text{Illuminated region} \tag{a}$$

$$\sigma\overline{T^4} = f_s \cos\theta_o + \frac{A_c}{A_a}\,\bar{f}_c \quad \text{Illuminated or shadowed region} \tag{b}$$

$$\sigma T^4 = C\sigma\,\overline{T^4} + f_c \quad \text{Dark or shadowed region} \tag{c}$$

$$\sigma\,\overline{T^4} = \frac{A_c}{A_a}\,\bar{f}_c \quad \text{Dark Region} \tag{d}$$

(22)

$$f_c = k\,\frac{dT}{dz} \tag{e}$$

$$\bar{f}_c = k\,\frac{d\bar{T}}{dz} \tag{f}$$

$$\frac{d^2T}{dz^2} - \frac{1}{K}\,\frac{dT}{dt} = 0 \tag{g}$$

$$\frac{d^2\bar{T}}{dz^2} - \frac{1}{K}\,\frac{d\bar{T}}{dt} = 0 \tag{h}$$

The averaging in Eqs. 22f and h is over the crater surface, not over the variables z or t. Section 3 will concern only the behavior of the illuminated crater, and therefore diffusion of heat

into the surface can be neglected (Wesselink 1948). In this case the integral equations and the expression for the reradiation flux (Eq. 22a – c) are sufficient to describe the temperature distribution in the crater. The section following this (4) will explore the eclipse and lunation cooling of a lunar crater and will employ all of the Eqs. 22 in a numerical diffusion calculation. It should be noted that, except for the assumptions presented in Section 1.2 and the approximation made in Section 4.2, these equations represent an exact solution for the thermal behavior of a spherical lunar crater.

3. Daytime Study of the Moon

3.1 The Experiments of Pettit and Nicholson

Infrared observations of the illuminated Moon were made almost 40 years ago by Pettit and Nicholson (1930). Their equipment consisted of a thermocouple that was used as a radiation detector and a glass slide and water cell for the filter. In spite of the primitive nature of this equipment in comparison with the cooled semiconductor detectors and interference filters used today, they were able to obtain excellent data on the illuminated and eclipsed Moon. This is partly due to the extreme care that they used in reducing their data. The transmission of the atmosphere and filters were worked out in detail. It is remarkable that they were able to obtain a minimum detectable temperature of 120 $^{\circ}$ K. Present sensitivities in the 8 — 14 μ telluric water vapor window are around 105° K. The equipment was mounted at the focus of the Mt. Wilson 100" telescope. The data on the illuminated Moon were obtained from two kinds of experiments: scans across the full moon and tracking of the subsolar point. The results obtained do not agree with a smooth Lambert sphere model for the Moon. In this section we will show that the anomalous results obtained by Pettit and Nicholson can be interpreted as the result of micrometeorite craters covering the lunar surface.

The first experiment that Pettit and Nicholson performed on the illuminated Moon was to scan across the equator during a full moon (Fig. 7a). Essentially this was equivalent to a laboratory experiment where the source and detector are fixed at the same angle

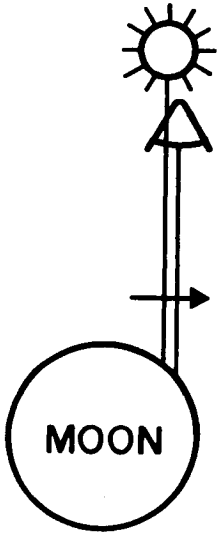

SCAN ACROSS THE FULL MOON

(a)

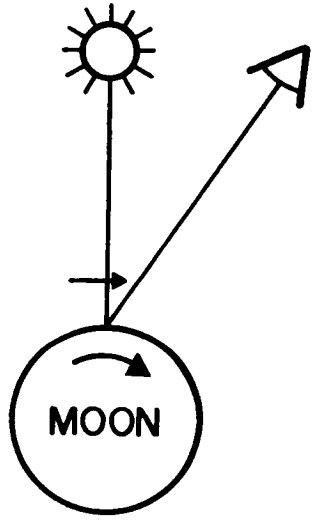

TRACKING SUB-SOLAR POINT

(b)

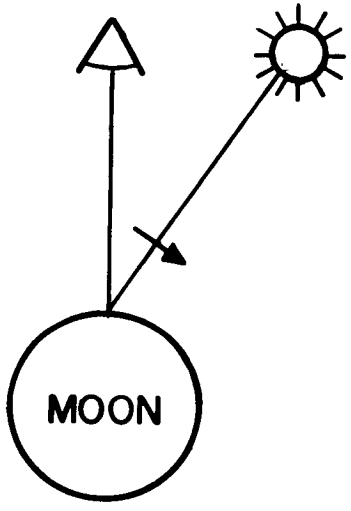

OBSERVATION OF THE SUB-EARTH POINT DURING A LUNATION

(c)

INFRARED EXPERIMENTS ON THE ILLUMINATED MOON

FIGURE 7

and the tilt of the surface is varied. The results of this measurement showed an apparent limb brightening over that predicted by a smooth Lambert sphere. Thus the lunar surface emits in the direction of the source more thermal radiation at oblique incidence than a Lambert surface.

In the second experiment they followed the sub-solar point for half a lunation (Fig. 7b), thus giving data on the radiation pattern of the surface under normal illumination. This was equivalent to maintaining the source fixed normal to the surface and rotating the detector. The measurement revealed a sharp decrease in the radiation tangential to the surface compared with a Lambert area. Hence the thermal emission from the lunar surface is peaked in the direction of illumination for both normal and oblique incidence.

3.2 The Temperature Distribution in an Illuminated Crater

The amount of heat flow into the lunar surface is extremely small when compared with the solar flux. Wesselink (1948) calculates that the conducted flux is 1% of the radiation flux at the sub-solar point. This means that the daytime temperatures on the Moon are determined almost entirely by the radiation balance at the surface. This radiation dominated temperature distribution can be calculated directly from Eqs. 22 without the need of a computer. The reradiation flux is given by Eq. 22b where the conduction term is neglected

$$\sigma \overline{T^4} = f_s \cos \theta_o \qquad (23)$$

The temperature of a point in the crater is given by Eqs. 22a and 22c again neglecting the conduction term:

Illuminated region:

$$\sigma T^4 = (1 - a) f_s \cos \psi + C\sigma \overline{T^4} \qquad (24)$$

Shadowed region:

$$\sigma T^4 = C\sigma \overline{T^4}$$

We can directly substitute Eq. 23 into Eqs. 24 and immediately obtain the temperature distribution:

Illuminated region:

$$\sigma T^4 = (1 - a) f_s \cos \psi + C f_s \cos \theta_o \qquad (25a)$$

Shadowed region:

$$\sigma T^4 = C f_s \cos \theta_o \qquad (25b)$$

This is a simple analytic expression for the temperature in a lunar crater and only requires the knowledge of the solar incidence angle with with respect to a flat area (θ_o) and with respect to the local element of area in the crater (ψ) as shown in Fig. 5. It should be noted that

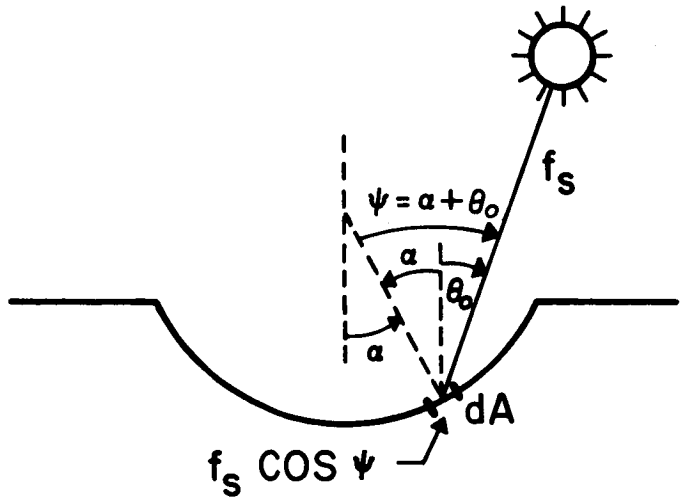

GEOMETRY OF THE SOLAR FLUX

FIGURE 8a

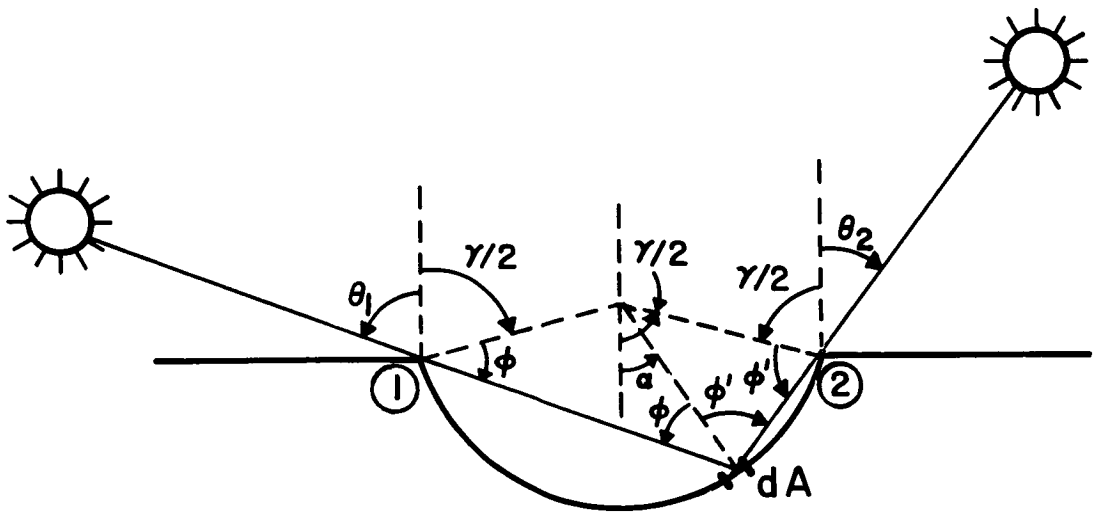

(θ_o=0 IS NOON, ALL ANGLES OF θ_o BEFORE NOON ARE NEGATIVE)

SHADOWING OF dA OCCURS FOR $\theta_o < \theta_a$, $\theta_o > \theta_b$ SHADOWING ANGLES

FIGURE 8b

$$\theta < \theta_a = -90 + \gamma/4 - \alpha/2$$

or (26)

$$\theta > \theta_a = 90 - \gamma/4 - \alpha/2$$

These shadow limits are derived in Appendix III. Effectively the Sun rises late and sets early due to the crater walls.

3.4 The Angular Distribution of Radiation from a Crater

The inhomogeneous temperature distribution in the crater, which is expressed in Eq. 25, raises the question of whether or not the crater as a whole radiates according to the Lambert cosine law. Pettit and Nicholson plotted the distribution of planetary heat (radiation pattern) about the sub-solar point and found the lunar surface to deviate significantly from a Lambert surface (Fig. 9a). To show that such a deviation from a Lambert surface can be explained by the presence of small, unresolved craters, we calculate the radiation pattern of various craters.

Up to now we have only been interested in the total flux or Poynting vector (watts/m^2) at a surface and the integrations performed have been rather easy. The radiation pattern involves calculating the average brightness of the surface in a particular direction (watts/m^2/steradian). In effect this means integrating the brightness (multiplied by the Lambert cosine law) over the crater surface and dividing by the crater aperature area. We assume the Sun to be directly overhead, since this is the sub-solar point, and vary the angle of the observer. We must be careful in the integration only to

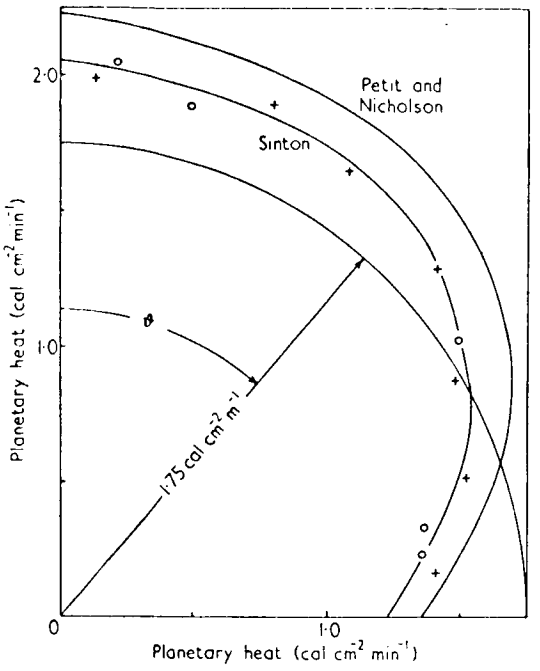

Polar diagram showing the heat emitted by the subsolar point of the Moon as a function of the angle ϑ from the normal to the surface. Crosses and circles designate measurements before and after full Moon, respectively.

FIG. 9a. Radiation pattern for the sub-solar point (Sinton 1962).

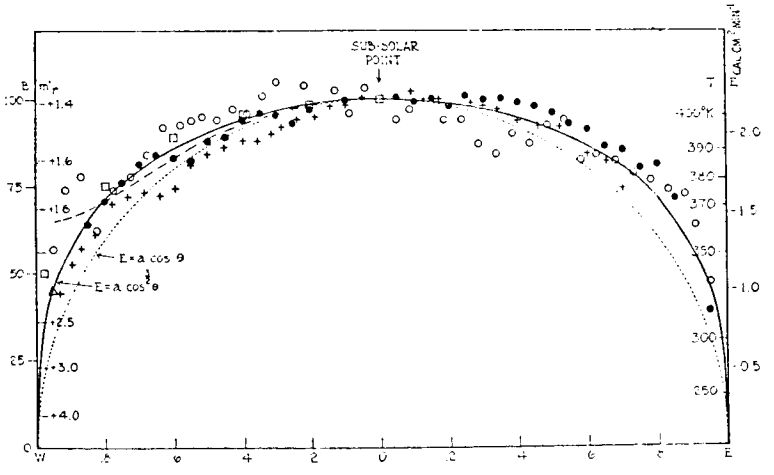

—Distribution of planetary heat over the disk at full moon

FIG. 9b. Scan of the full Moon (Pettit and Nicholson 1930).

integrate over the part of the crater seen by the observer and not the whole crater. Since the Sun is directly overhead there is no solar shadowing, but there is this effective shadowing by the observer.

The situation is shown in Fig. 10. The Sun is at an angle ψ with respect to the surface normal at P. Similarly the observer is at an angle ψ'. The temperature of the point P is given by Eq. 25a, where the Sun is at the zenith ($\theta_o = 0$) so that the whole crater is illuminated:

$$\sigma T^4 = (1 - a) f_s \cos \psi + C f_s \tag{27}$$

$$C = \frac{A_c}{4\pi r^2}$$

The point P radiates according to the Lambert cosine law, giving the brightness of P in the direction of the observer as:

$$B \cos \psi' = \frac{\sigma T^4}{\pi} \cos \psi' = \frac{(1 - a) f_s}{\pi} \cos \psi \cos \psi' + C \frac{f_s}{\pi} \cos \psi' \tag{28}$$

We now integrate this over the crater floor, integrating only over the region not shadowed by the observer. The second term in Eq. 28 only depends on ψ' and therefore is just the projected area in the direction of the observer. Being careful to integrate only over the unshadowed floor, as in Eq. 14, we obtain:

$$\int_{\text{observable floor}} \cos \psi' \, dA = A_a \cos \theta_o \tag{29}$$

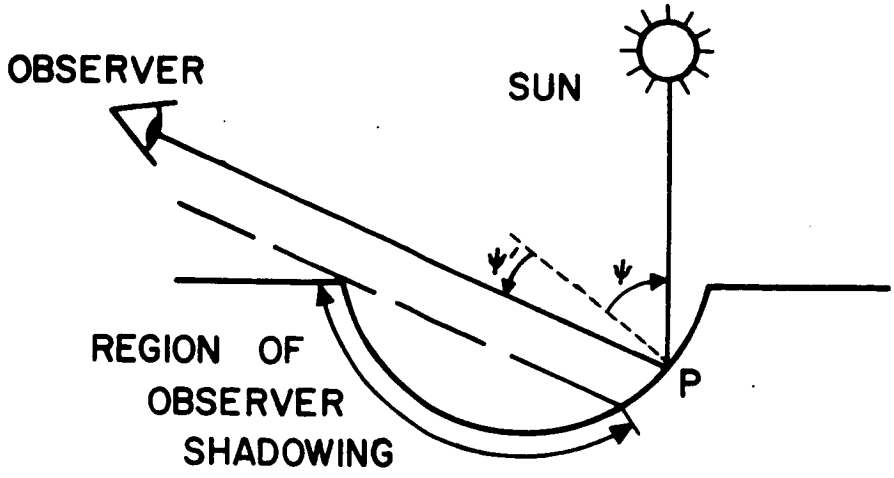

GEOMETRY FOR DETERMINING RADIATION PATTERN

FIGURE 10

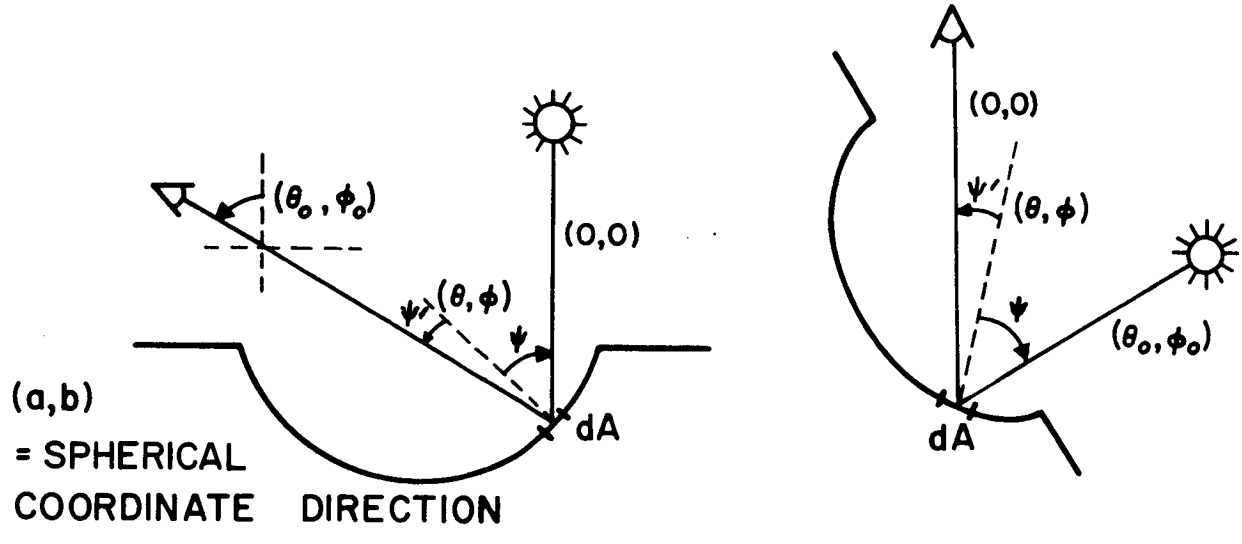

(a) (b)

SPHERICAL COORDINATE SYSTEM WITH SUN ON Z-AXIS

ROTATED SYSTEM WITH OBSERVER ON Z-AXIS

FIGURE 11

where A_a equals the aperture area and θ_o is now defined as the direction of the observer. Thus the second term of Eq. 28 gives just the results of a Lambert surface. The total integrated brightness is then:

$$\int B \cos \psi' \, dA = \frac{(1-a) f_s}{\pi} \int \cos \psi \cos \psi' \, dA + C \frac{f_s}{\pi} A_a \cos \theta_o \tag{30}$$

The average brightness of the crater is obtained by dividing Eq. 30 by the projected area of the crater as seen by the observer, i.e. $A_a \cos \theta_o$:

$$\overline{B} = \frac{f_s}{\pi} \left[\frac{(1-a)}{A_a \cos \theta_o} \int \cos \psi \cos \psi' \, dA + C \right] \tag{31}$$

The integral is performed only over the observable floor using the geometry shown in Fig. 11a. To make the integration easier, we rotate the coordinate system to Fig. 11b where the observer is now on the z-axis and the Sun and the crater have been tilted by θ_o. (The Sun is still directly over the crater; however, the angle ϕ has been rotated by 180°.) In Appendix III we have worked out the form of the integral as:

$$\int \cos \psi \cos \psi' dA = \frac{r^2 \cos \theta_o}{3} \int_o^{2\pi} (\cos^3 \theta_1 - \cos^3 \theta_2) \, d\phi - \frac{r^2 \sin \theta_o}{3} \int_o^{2\pi} (\sin^3 \theta_2 - \sin^3 \theta_1) \cos \phi \, d\phi \tag{32}$$

The limits of the θ integration (θ_1 and θ_2), which appear in Eq. 32, are functions of ϕ. They represent the spherical coordinates of the shadow-rim boundary shown in Fig. 12. The contour has to be evaluated numerically. The geometry for solving for the shadow-rim boundary is as follows. The observer on the z-axis sees all the region of the crater within a cylinder that intersects the crater rim. Since the cylinder is defined by the circular rim, which is tilted at an angle θ_o, its base is an ellipse. The intersection of this elliptical cylinder with the sphere is the shadow-rim contour. The coordinates of the contour must be solved numerically and then the integrals in Eq. 32 run on a computer. The results of the computer for the sine and cosine integrals are given in Table I for various crater angles and observing angles. Generally the angle θ_1 is zero except when the shadow-rim boundary is entirely on one side of the z-axis. Except for this case the θ integration is between θ_2 and zero. These integration limits are derived in Appendix V. For the hemispherical crater the limit can be stated analytically:

$$\sin^2 \theta_2 = \frac{1}{1 + \tan^2 \theta_o \cos^2 \phi}$$

$$\cos^2 \theta_2 = \frac{\tan^2 \theta_o \cos^2 \phi}{1 + \tan^2 \theta_o \cos^2 \phi} \qquad (33)$$

$$\theta_1 = 0$$

From Appendix II we have the expression for the aperture area A_a as:

$$\frac{A_a}{4\pi r^2} = C\ (1 - C) \qquad (34)$$

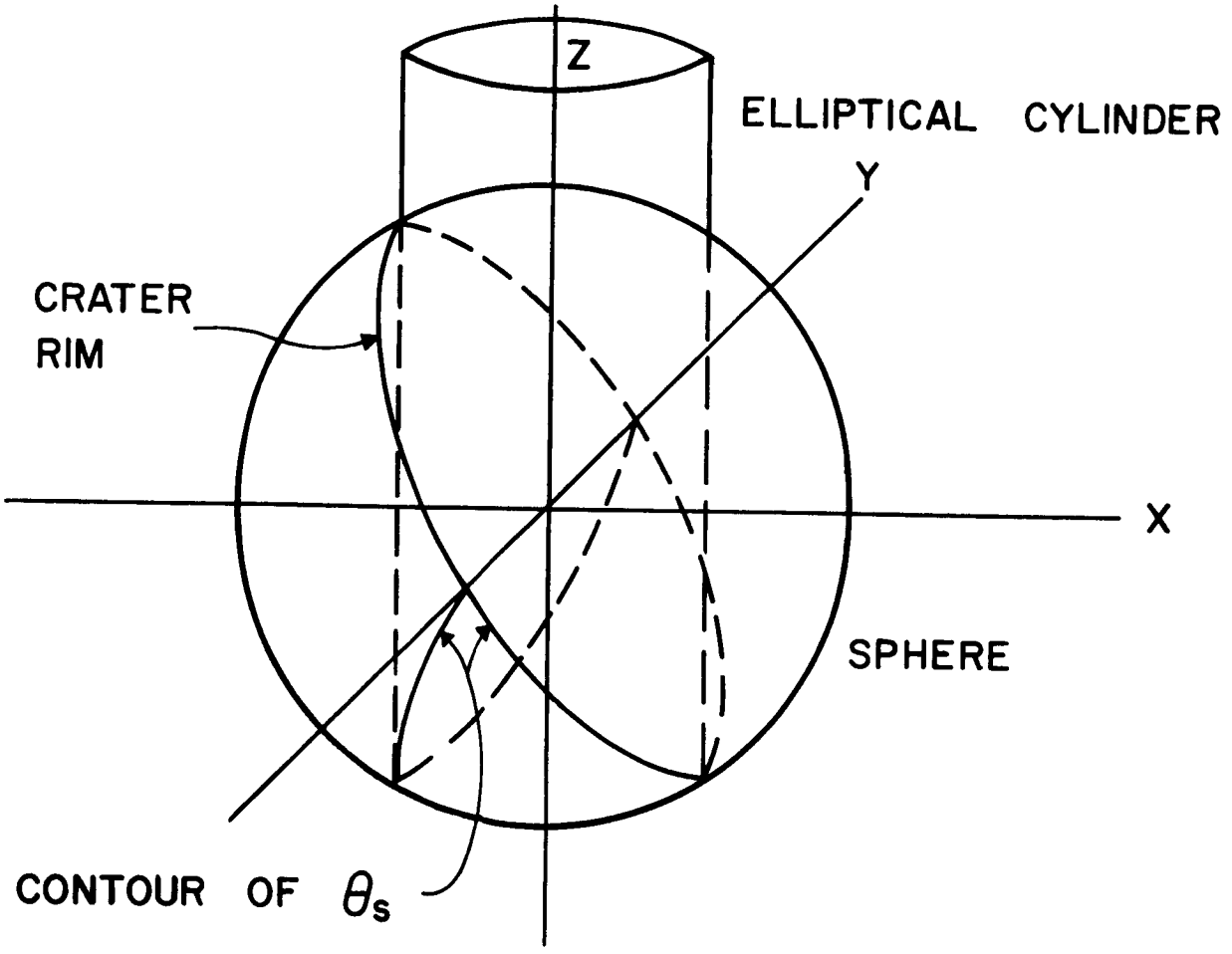

GEOMETRY FOR DETERMINING SHADOW–RIM INTEGRATION CONTOUR

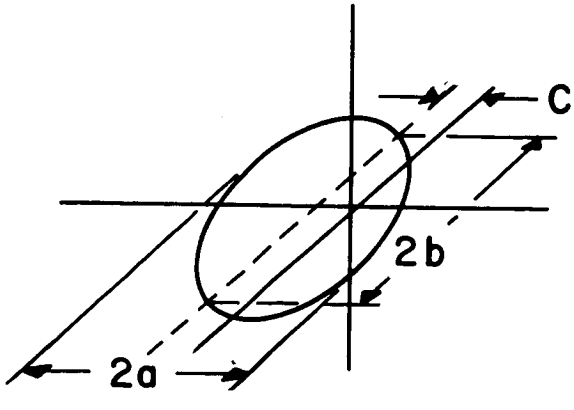

ELLIPTICAL CYLINDER

FIGURE 12

COSINE INTEGRAL

	Crater Angle (γ)						
θ_0	180°	150°	120°	90°	60°	30°	10°
0	6.2832	6.1743	5.4978	4.0618	2.2021	0.6206	0.0715
5	6.2814	6.1570	5.4710	4.0364	2.1866	0.6160	0.0709
10	6.2691	6.1056	5.3912	3.9613	2.1406	0.6023	0.0693
15	6.2360	6.0218	5.2610	3.8385	2.0655	0.5798	0.0667
20	6.1725	5.9072	5.0844	3.6720	1.9634	0.5495	0.0630
25	6.0700	5.7591	4.8666	3.4666	1.8377	0.5115	0.0584
30	5.9208	5.5727	4.6142	3.2287	1.6920	0.4685	0.0535
35	5.7191	5.3434	4.3344	2.9655	1.5308	0.4195	0.0478
40	5.4603	5.0679	4.0309	2.6850	1.3590	0.3684	0.0417
45	5.1416	4.7442	3.7050	2.3957	1.1802	0.3162	0.0359
50	4.7621	4.3714	3.3576	2.1066	1.0043	0.2625	0.0298
55	4.3228	3.9505	2.9896	1.8205	0.8351	0.2119	0.0237
60	3.8264	3.4836	2.6024	1.5415	0.6724	0.1636	0.0178
65	3.2774	2.9743	2.1962	1.2716	0.5261	0.1198	0.0130
70	2.6818	2.4277	1.7788	1.0059	0.3965	0.0817	0.0086
75	2.0472	1.8495	1.3447	0.7487	0.2823	0.0517	0.0050
80	1.3821	1.2458	0.9025	0.4958	0.1807	0.0290	0.0023
85	0.6963	0.6269	0.4530	0.2472	0.0880	0.0127	0.0007

SINE INTEGRAL

	Crater Angle (γ)						
θ_0	180°	150°	120°	90°	60°	30°	10°
0	-0.00	-0.0000	-0.0000	-0.0000	-0.0000	-0.0000	-0.0000
5	-0.00	-0.1976	-0.3069	-0.2893	-0.1772	-0.0529	-0.0062
10	-0.00	-0.3892	-0.6044	-0.5698	-0.3490	-0.1043	-0.0122
15	-0.00	-0.5690	-0.8836	-0.8330	-0.5101	-0.1525	-0.0178
20	-0.00	-0.7314	-1.1359	-1.0709	-0.6558	-0.1960	-0.0229
25	-0.00	-0.8717	-1.3537	-1.2763	-0.7816	-0.2335	-0.0272
30	-0.00	-0.9855	-1.5304	-1.4429	-0.8836	-0.2642	-0.0308
35	-0.00	-1.0693	-1.6606	-1.5656	-0.9587	-0.2862	-0.0334
40	-0.00	-1.1207	-1.7403	-1.6408	-1.0048	-0.3001	-0.0349
45	-0.00	-1.1379	-1.7671	-1.6661	-1.0194	-0.3053	-0.0357
50	-0.00	-1.1207	-1.7403	-1.6409	-1.0045	-0.3000	-0.0353
55	-0.00	-1.0693	-1.6606	-1.5656	-0.9589	-0.2871	-0.0337
60	-0.00	-0.9855	-1.5304	-1.4426	-0.8843	-0.2646	-0.0306
65	-0.00	-0.8717	-1.3534	-1.2771	-0.7821	-0.2338	-0.0275
70	-0.00	-0.7315	-1.1363	-1.0702	-0.6563	-0.1948	-0.0232
75	-0.00	-0.5690	-0.8833	-0.8330	-0.5106	-0.1527	-0.0180
80	-0.00	-0.3889	-0.6046	-0.5690	-0.3492	-0.1046	-0.0122
85	-0.00	-0.1971	-0.3072	-0.2896	-0.1773	-0.0529	-0.0061

Table 1

Integrals Evaluated on the Computer

Substituting this and the integral shown in Eq. 32 in the average brightness equation (Eq. 31), we get:

$$\overline{B} = \frac{f_s}{\pi} \left[\frac{(1-a)}{12\pi C (1-C)} \int_0^{2\pi} (\cos^3 \theta_1 - \cos^3 \theta_2)\, d\phi \right. \\ \left. - \frac{(1-a)\tan\theta_o}{12\pi C (1-C)} \int_0^{2\pi} (\sin^3 \theta_2 - \sin^3 \theta_1) \cos\phi\, d\phi + C \right] \tag{35}$$

Since f_s/π is the brightness for a flat Lambert surface, we refer to the quantity in brackets in Eq. 35 as the radiation pattern for the crater. Thus the radiation pattern for a flat surface is unity in all directions. This definition of radiation pattern as the ratio of the brightness of a rough surface to the brightness of a flat Lambert surface is appropriate for comparison with the distribution of planetary heat about the subsolar point obtained by Pettit and Nicholson.

3.5 Radiation Patterns of Several Craters

The brightness of a radiating surface is proportional to the amount of power that a detector would receive when looking at the surface in a particular direction. This is related to the brightness temperature by the Plánck radiation law. For a Lambert surface the cosine law is cancelled out by the secant dependence of the area seen by the detector. Hence a Lambert surface appears equally bright from any direction. The brightness of a rough surface, however, is dependent on the direction from which it is viewed. The Moon's surface has an anomalous radiation pattern such that its brightness will appear higher in the direction of the Sun and will decrease away from the Sun. The case of the sub-solar point is illustrated in Fig. 9a.

The average brightness of a crater under normal incidence can be calculated from Eq. 35 and Table I. The terms inside the brackets represent the radiation pattern, which is unity for a Lambert surface. For a crater the radiation pattern decreases as the angle of the observer (θ_o) increases. This is due to the fact that the observer sees more of the rim and less of the central region. The surface visible at the rim has a much lower temperature than that at the center (Fig. 25a). Thus the effective brightness temperature of the crater is peaked in the direction of illumination.

The radiation patterns for several different crater angles were evaluated and plotted in Fig. 13. The Pettit and Nicholson data for the Moon is plotted along with them. This represents a relative crater density of 1.0. Adding a certain amount of flat area reduces the variation in brightness so that it approaches a constant value. We illustrate that in Fig. 14, where the brightness of hemispherical craters is shown for various values of relative crater density. In comparing Figs. 13 and 14, we see that to some extent one can make a trade-off between relative density and depth to diameter ratio and still obtain a good fit to the Pettit and Nicholson data. We will attempt to resolve this problem by obtaining the density from the data on the scan across a full Moon.

The radiation patterns that have been calculated from the average crater brightness, Eq. 35, have assumed that the detector has an infinite spectrum bandwidth. This is not quite accurate since the observations of Pettit and Nicholson were made in the $8 - 14\mu$ telluric water vapor window. To calculate the brightness of a crater as seen

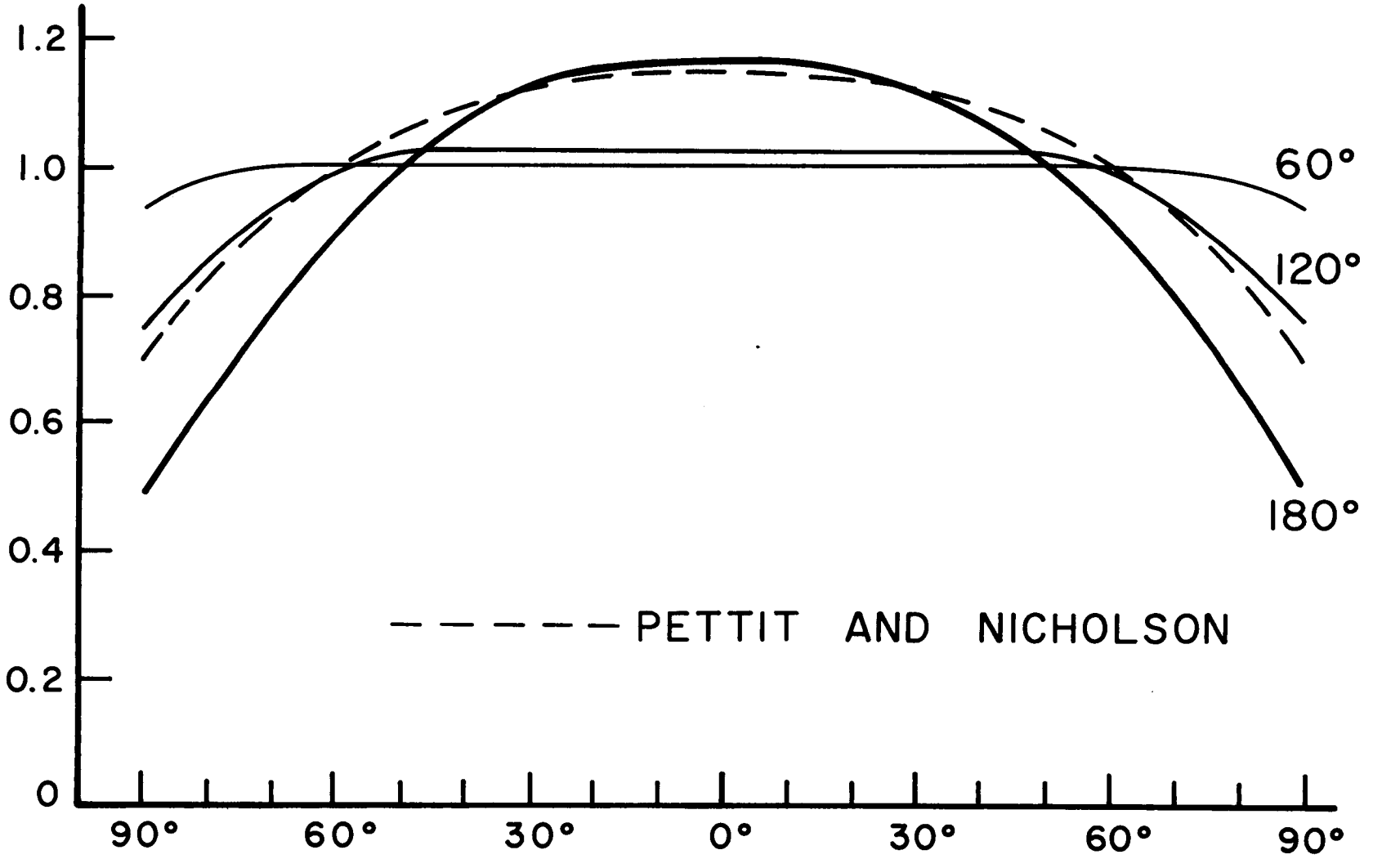

FIGURE 13

RADIATION PATTERN FOR VARIOUS ANGLE CRATERS

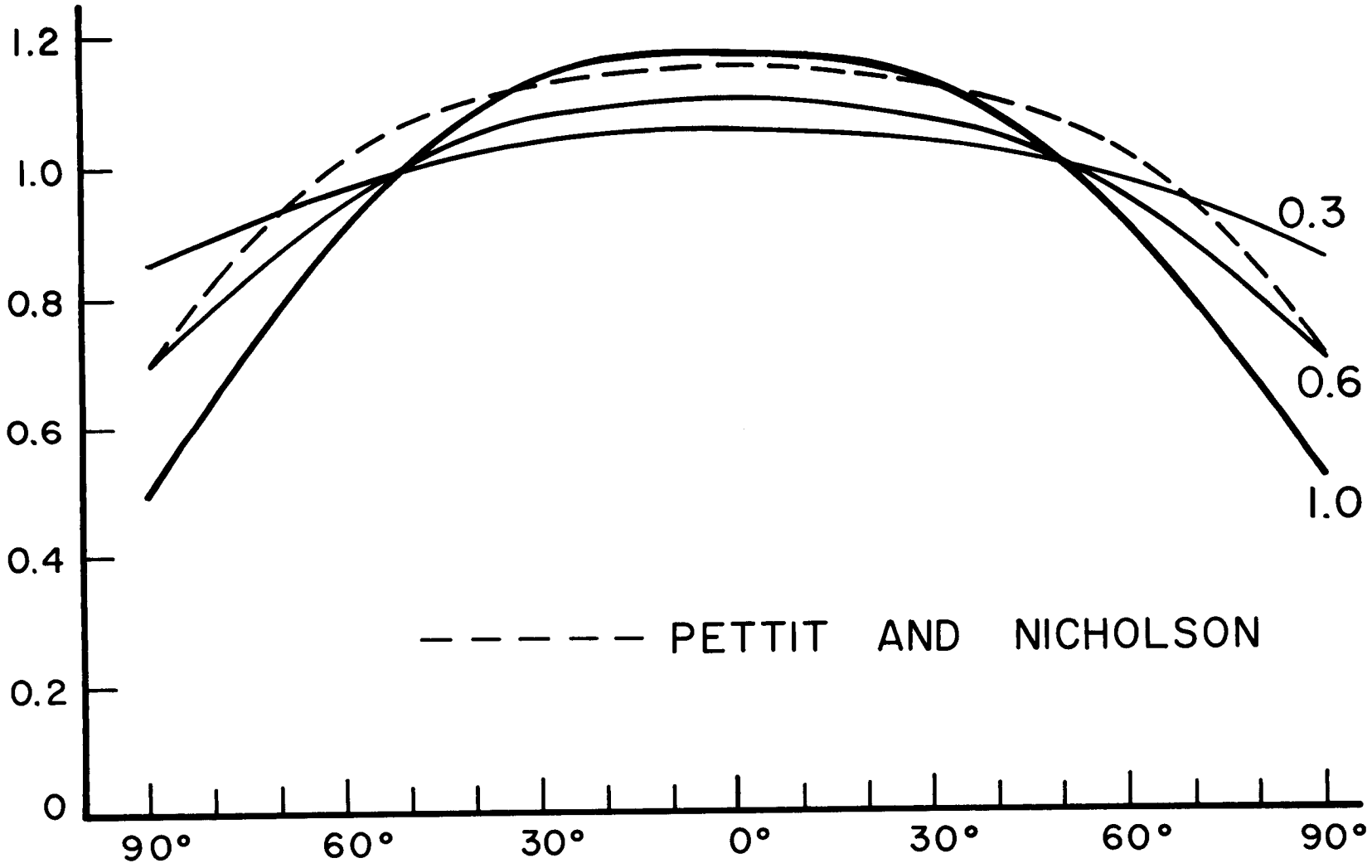

FIGURE 14

RADIATION PATTERN FOR VARIOUS DENSITY HEMISPHERICAL CRATERS

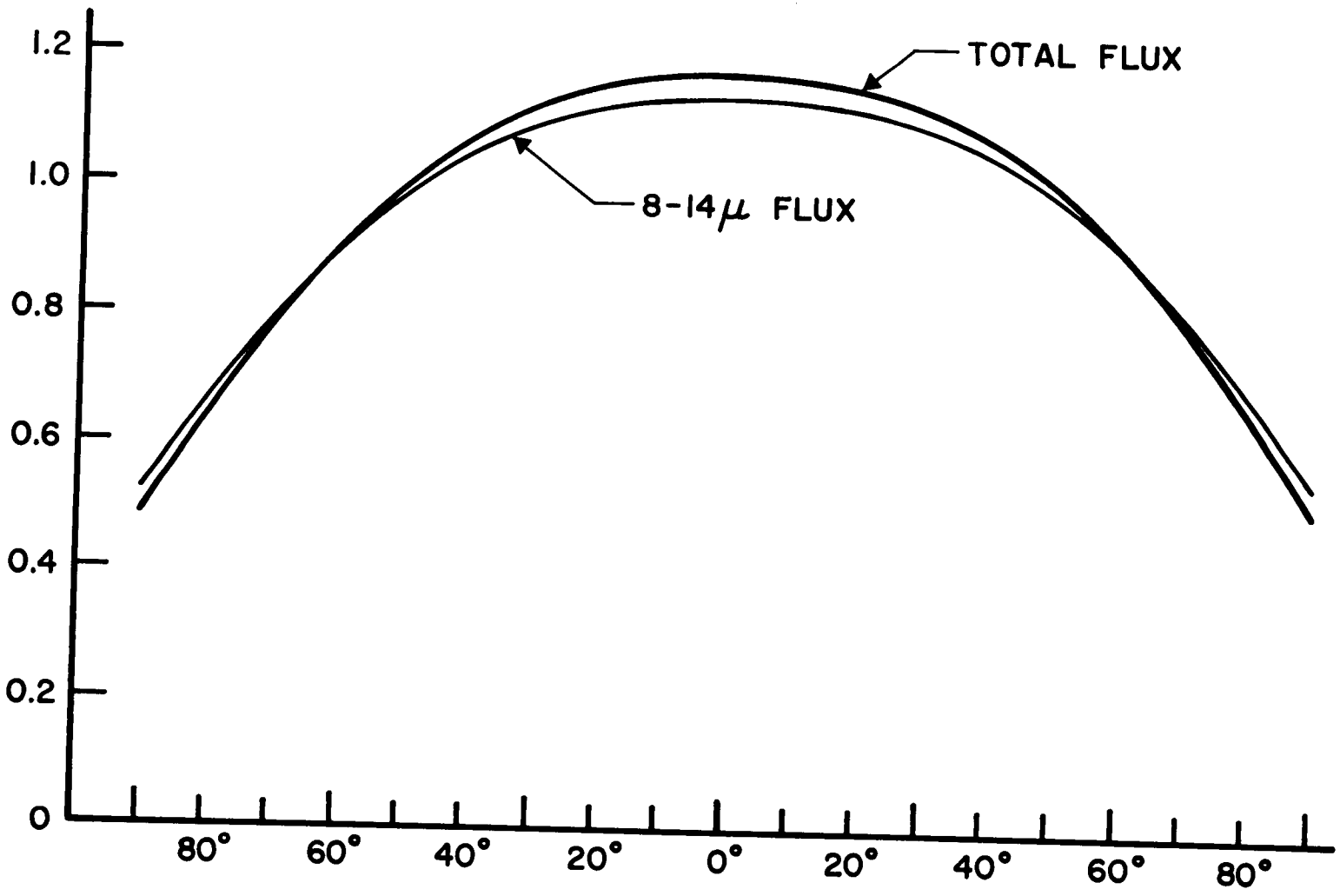

FIGURE 15

RADIATION PATTERN OF HEMISPHERICAL CRATER AS SEEN IN 8-14μ WINDOW

in this window, we have interchanged the order of integration in Eq. 32. By integrating over ϕ first we are integrating over strips of constant temperature. The θ integral can then be evaluated numerically using the integral of the Planck radiation law to approximate the flux in the $8 - 14\,\mu$ interval. The calculation shows that the effect of this limited bandwidth is small. This is because we are working in region of the Planck radiation curve that varies approximately as T^4 so that assuming a T^4 variation in brightness (Eq. 28) is sufficient. A plot of the radiation pattern of a 180° crater, as seen in the $8 - 14\,\mu$ interval, and for an infinite bandwidth detector is shown in Fig. 15.

3.6 Cylindrical Model for a Crater

In order to predict the radiation patterns for craters deeper than hemispherical, we have set up a cylindrical crater with the Sun at normal incidence. In this case only the bottom of the crater receives direct radiation from the Sun. The bottom is assumed to be at a uniform temperature. The walls of the crater are heated by the reradiation flux. The integral equation governing the temperature on the walls of a cylinder is derived in Appendix VI.

$$\sigma T^4(z) = f_b(z) + \int_0^d K(z, z')\, \sigma T^4(z')\, dz' \tag{36}$$

$$f_b(z) = \int_0^{\phi_1} \frac{f_o}{2\pi} (\cos 2\theta_2 - \cos 2\theta_1)\, d\phi \tag{37}$$

$$\operatorname{cotan} \theta_{1,2} = \frac{1}{z} \left(\cos\phi \mp (\cos^2\phi - z^2 \sin^2\phi)^{\frac{1}{2}} \right)$$

$$\text{cotan } \phi_1 = z$$

where f_b is the flux radiated from the bottom of the crater. The kernel is no longer simple, as in the case of a spherical crater, and must be numerically integrated.

$$K(z, z') = \frac{1}{\pi} \int_0^{2\pi} \left[\frac{2 \sin^2 \frac{\phi}{2}}{\left((z - z')^2 + 4 \sin^2 \frac{\phi}{2} \right)} \right]^2 d\phi \qquad (38)$$

The solution to the integral equation was obtained by a successive approximation method. A trial temperature distribution was substituted into the right side of Eq. 36. The integral was then numerically integrated to give a new temperature distribution on the left side of Eq. 36. Convergence was dependent on the depth-to-diameter ratio of the crater, with a 5 : 1 depth to diameter crater requiring 100 successive approximations. Shallower craters converged more rapidly.

The brightness of the crater in a particular direction is then easily obtained by numerically integrating over the visible region of the crater as was done for the spherical crater. The results of this calculation are shown in Fig. 16. The radiation patterns show an interesting reversal of curvature as the depth-to-diameter ratio increases. The deeper craters exhibit a pattern more typical of the photometric back-scattering, while the shallower ones approximate the thermal radiation patterns. This suggests that the craters causing the anomalous daytime radiation patterns are approximately hemispherical.

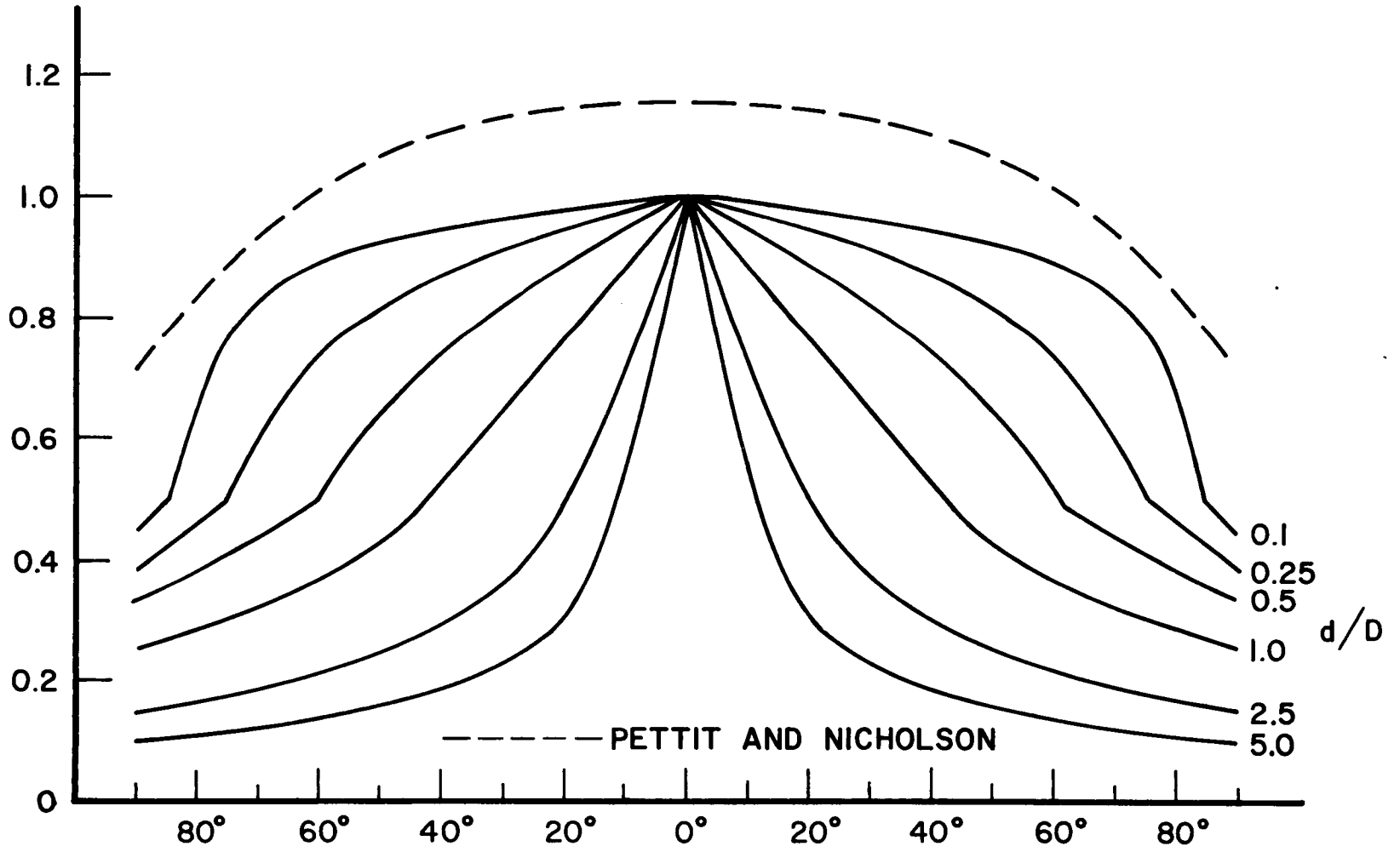

FIGURE 16

RADIATION PATTERN FOR A CYLINDRICAL CRATER

3.7 Apparent Temperature Across the Full Moon

The variation of thermal radiation, if the Moon were a Lambert surface, should follow a cosine law across to the limb. The data of Pettit and Nicholson (1930) and work by Shorthill and Saari indicate a $(\cos\theta)^n$ variation with the exponent (n) equal to $\frac{2}{3}$ at the center but decreasing toward the limb. The data, which is illustrated in Fig. 9b, exhibits a large scatter indicating an uncertainty in the value of the exponent. Accepting the value of $\frac{2}{3}$, the apparent temperature variation is:

Lambert Surface	Moon
$\sigma T^4 \approx \cos\theta$	$\sigma T^4 \approx (\cos\theta)^{\frac{2}{3}}$
$T \approx (\cos\theta)^{\frac{1}{4}}$	$T \approx (\cos\theta)^{\frac{1}{6}}$

(39)

Hence the Moon's surface exhibits an infrared limb brightening when compared with a smooth Lambert surface. These experimental results can be explained by the presence of craters that affect the apparent temperature of the full Moon.

The calculation proceeds in the same way as for the radiation patterns. The Sun is now at the same angle as the observer ($\psi = \psi'$) and so both can be placed along the z-axis with a suitable rotation (Fig. 17). Eq. 25a can be applied since the solar and observer shadowing are identical:

$$\sigma T^4 = (1 - a) f_s \cos\psi + C f_s \cos\theta_o \qquad (40)$$

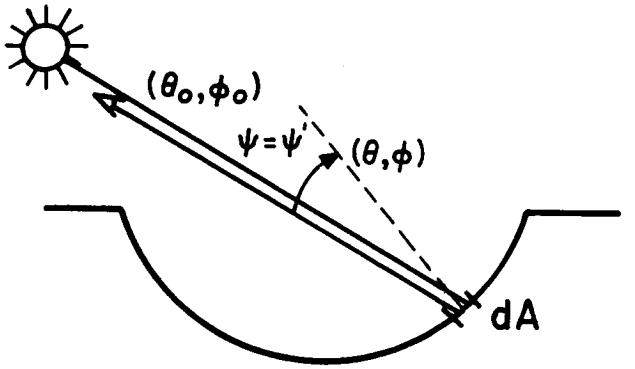

(a)

SPHERICAL SYSTEM

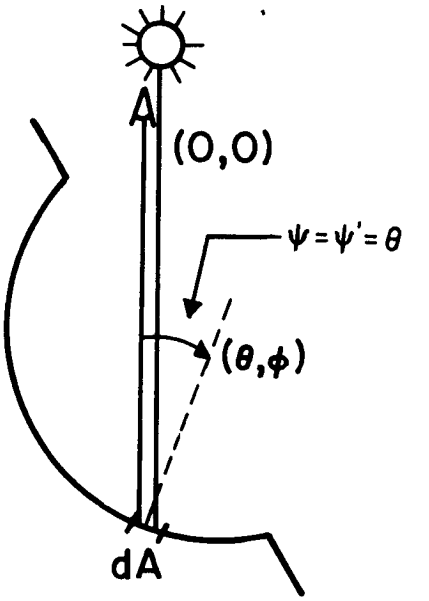

(b)

ROTATED SYSTEM WITH SUN AND OBSERVER ON Z-AXIS

FIGURE 17

The Sun is at an angle θ_o to the lunar surface normal, thus giving a different temperature distribution than in the radiation pattern calculation. The brightness is the same as previously (Eq. 28):

$$B \cos \psi = \frac{\sigma T^4}{\pi} \cos \psi = \frac{(1 - a) f_s}{\pi} \cos^2 \psi + C \frac{f_s}{\pi} \cos \theta_o \cos \psi \qquad (41)$$

Again the second term integrates to give the projected crater aperture:

$$\int \cos \psi \, dA = A_a \cos \theta_o$$

$$\int B \cos \psi \, dA = \frac{(1 - a) f_s}{\pi} \int \cos^2 \psi \, dA + C \frac{f_s}{\pi} A_a \cos^2 \theta_o \qquad (42)$$

From Fig. 17, it is obvious that $\psi = \theta$, so that the average brightness is:

$$\overline{B} = \frac{1}{A_a \cos \theta_o} \int B \cos \psi \, dA = \frac{f_s}{\pi \cos \theta_o} \left[\frac{r^2 (1 - a)}{A_a} \right.$$

$$\left. \int_0^{2\pi} \int_{\theta_1}^{\theta_2} \cos^2 \theta \sin \theta \, d\theta \, d\phi + C \cos^2 \theta_o \right] \qquad (43)$$

$$\frac{A_a}{4\pi r^2} = C (1 - C)$$

The integration is over the same contour as before (Fig. 12).

$$\overline{B} = \frac{f_s}{\pi \cos \theta_o} \left[\frac{(1 - a)}{12 \pi C (1 - C)} \int_0^{2\pi} (\cos^3 \theta_1 - \cos^3 \theta_2) \, d\phi \right.$$

$$\left. + C \cos^2 \theta_o \right] \qquad (44)$$

The average brightness temperature is just the temperature of a black body, which gives the same observed brightness:

$$\frac{\sigma T^4}{\pi} = \overline{B} = \frac{f_s}{\pi}\left[\frac{\sec\theta_o\,(1-a)}{12\pi C\,(1-C)}\right]\int_0^{2\pi}(\cos^3\theta_1 - \cos^3\theta_2)\;d\phi + C\cos\theta_o\Bigg] \tag{45}$$

For a Lambert surface this is just:

$$\frac{\sigma T^4}{\pi} = \overline{B} = \frac{f_s}{\pi}\cos\theta_o \tag{46}$$

The integral in Eq. 45 has been evaluated for the radiation patterns (Table I). The second term is again seen to be the same as a Lambert surface. We have plotted the brightness temperature (Eq. 45) in Fig. 18 along with the experimental results of $(\cos\theta_o)^{1/6}$ and a Lambert surface of $(\cos\theta_o)^{\frac{1}{4}}$.

Several curves for the 180° crater with various densities are shown in Fig. 19. It should be pointed out that a crater whose depth-to-diameter ratio is greater than that of a hemispherical crater will give approximately the same limb brightening since all that is visible at the limb is the crater rim. Thus Fig. 19 is somewhat independent of depth-to-diameter ratio and can be used to determine the relative density of craters.

By comparing Fig. 19 with Fig. 14 one can get some idea of the depth and density of the small lunar craters. The relative density as determined by Fig. 19 is about 0.3. This fits the observations that the exponent decreases as one goes toward the limb, giving greater limb brightening than $(\cos\theta_o)^{1/6}$. The 0.3 radiation pattern in Fig. 14 is somehwat shallow, however, one can make this

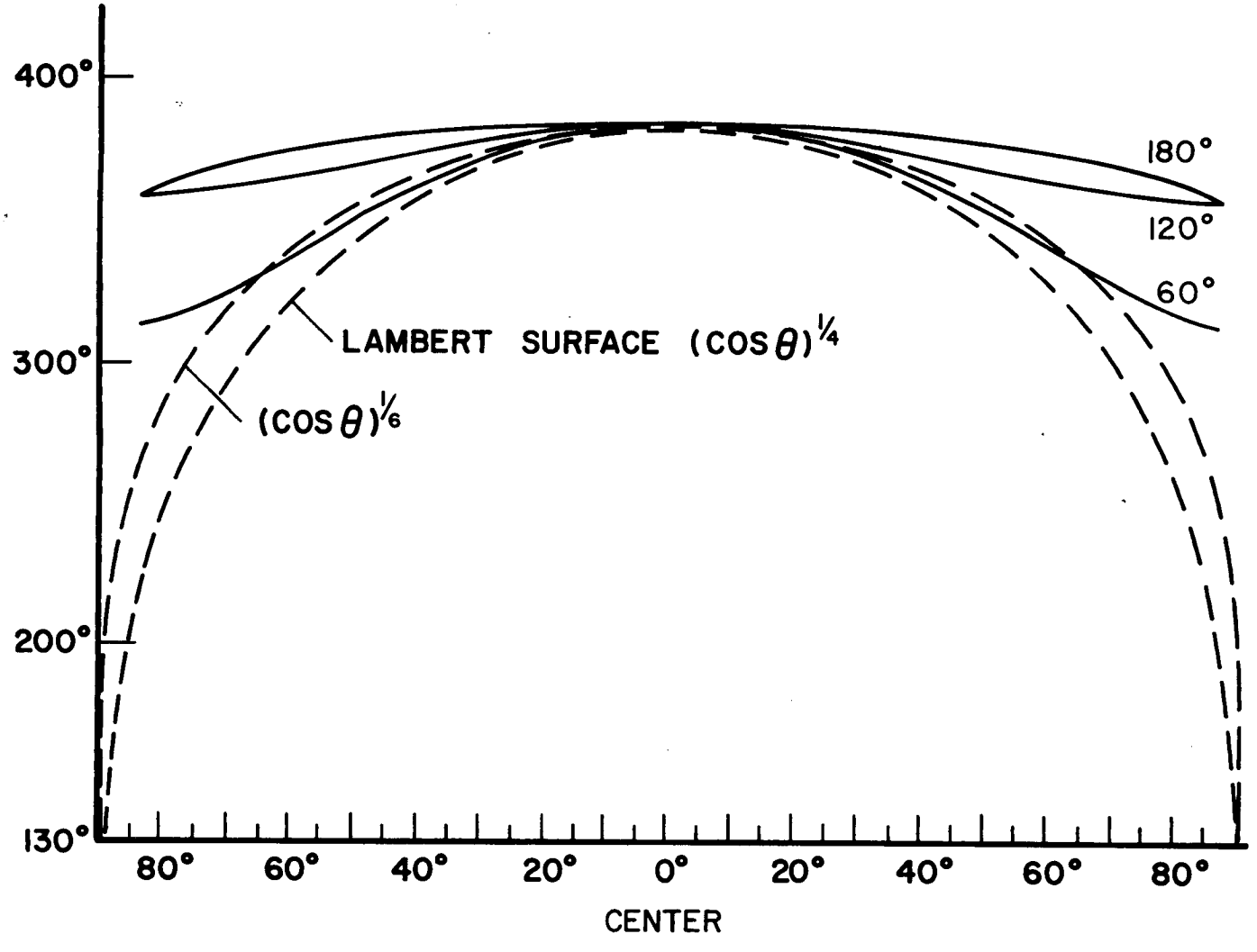

FIGURE 18
LIMB BRIGHTENING FOR
VARIOUS ANGLE CRATERS

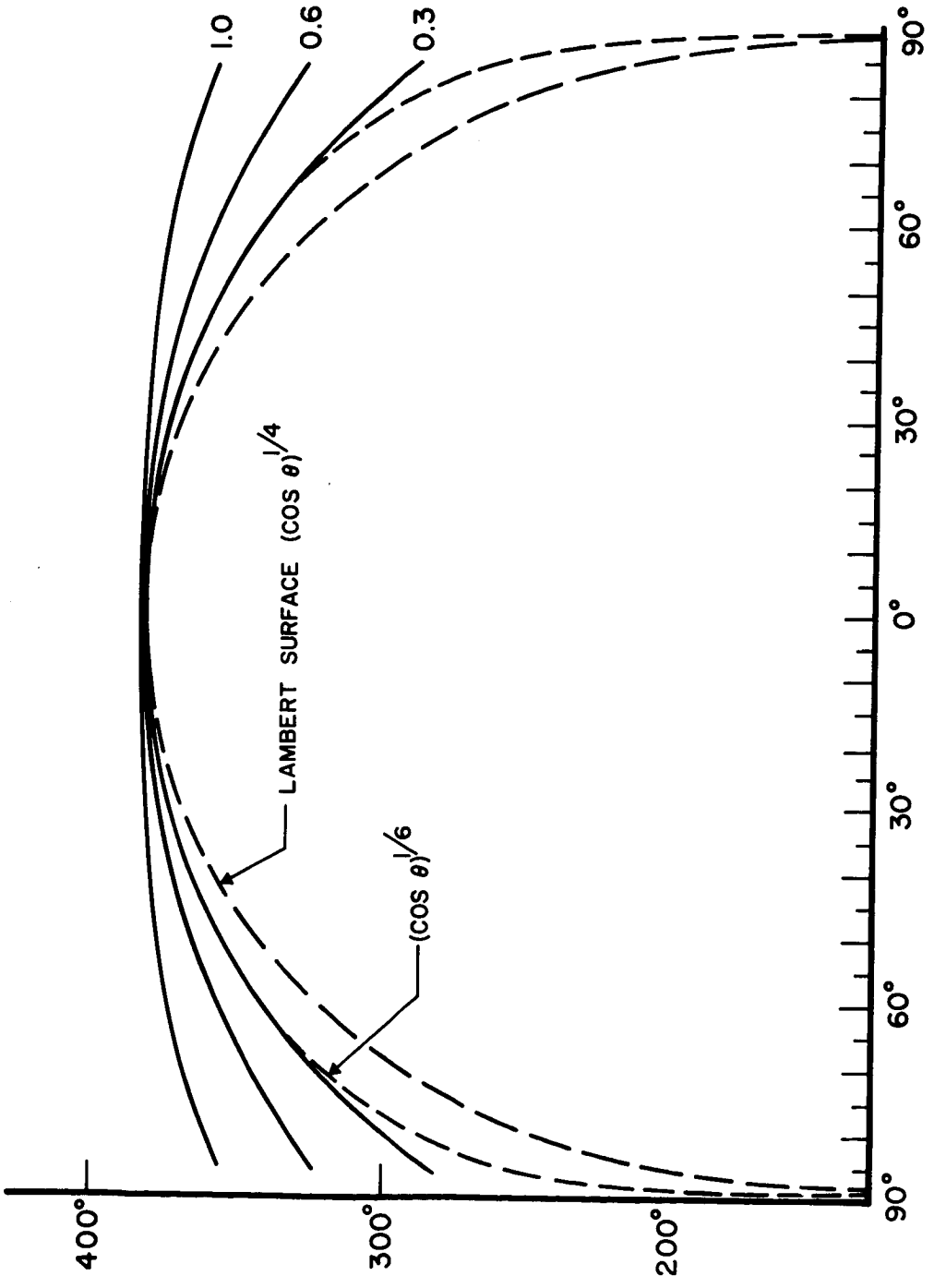

FIGURE 19

LIMB BRIGHTENING FOR VARIOUS DENSITY HEMISPHERICAL CRATERS

pattern considerably steeper by increasing the depth of the crater (Fig. 13). The increased depth will have little effect on the limb brightening curves, and will allow the radiation pattern to conform much more closely to the observed data. The geometry of craters deeper than hemispherical is rather difficult. The calculation of the cylinder (Fig. 16) indicates that the depth-to-diameter ratio for the craters cannot exceed about 1.0 because of the reversal in curvature of the radiation patterns. Therefore, we conclude that the relative density of small craters on the moon is about 0.3 and the depth-to-diameter ratio is slightly greater than that for a hemisphere. These results are for the particular idealized model we have chosen. In interpreting the infrared data of Pettit and Nicholson, one should realize the large amount of scatter that exists in the data. Some of this scatter may be due to the fact that each data point represents a different part of the lunar surface.

3.8 The Size of the Small Scale Craters

We have shown that the daytime radiation anomalies may be caused by the presence of small craters. These craters contain rather large temperature gradients as indicated in Fig. 25a. Up to now we have assumed for the illuminated crater that the conduction terms in the flux balance equations (Eqs. 22 a — c) are negligible. However, the existence of large temperature gradients on the surface may cause the lateral conducted flux to be quite large. To calculate the magnitude of such an effect consider the following.

The temperature within the crater is completely determined by the balance of flux condition, Eq. 25. The net lateral flux (f_ℓ) can be added in as follows:

$$\sigma T^4 = (1 - a) f_s \cos \psi + C f_s \cos \theta_o + f_\ell \tag{47}$$

The temperature distribution will be disturbed only when the lateral flux becomes of the order of the solar flux ($f_\ell \approx f_s$). This can be translated into a temperature gradient because the lateral flux must flow through the bulk material. Thus we obtain from the conductivity relation (Eq. 21) the maximum temperature gradient that can be maintined on the surface without disturbing the flux balance condition as:

$$\frac{dT}{dx} = \frac{1}{k} f_\ell \approx \frac{1}{k} f_s \tag{48}$$

The solar constant used for the temperature calculations was 0.033 g cal/cm^2/sec. Thermal conductivities for the Moon vary from 3×10^{-6} for a pumice of 35% porosity to 6×10^{-5} for an open cell structure of 88% porosity (Glaser and Wechsler 1965). Taking an average value of 10^{-5}, we get the following maximum temperature gradient.

$$\frac{dT}{dx} = \frac{1}{k} f_s = 3,300^\circ \text{ K/cm} \tag{49}$$

The temperature differences from center to rim for a hemispherical crater are about 100° K (Fig. 25a). This means that the temperature

distribution in the crater can be maintained down to a diameter as small as 1 mm. This represents a lower limit because craters smaller in diameter than 1 mm will begin to disturb the temperature balance condition (Eq. 25). As the temperature gradients are washed out by lateral flux, the crater will assume a constant temperature. Such a crater with a uniform temperature distribution radiates isotropically and cannot produce the anomalous radiation patterns that Pettit and Nicholson observed. It has been pointed out already that craters larger in diameter than 1 mm are shallower and their relative density decreases so that they are much less effective in causing the observed radiation anomalies. We therefore conclude that the anomalous infrared radiation from the Moon is most probably due to millimeter scale cratering and roughness.

The possibility of large temperature variations such as those shown in Figure 25a over very small dimensions is a very interesting result of our study. The anomalous emission from the subsolar point is very strong evidence for the existence of these temperature variations. We further suggest that the variations in temperature are produced by the illumination of micrometeorite craters of millimeter dimensions, rather than by larger craters or other objects. This follows from the high relative density needed to explain the anomalous infrared radiation from the Moon. Thus the picture of the lunar surface that we obtain from interpreting the infrared data indicates that 30% of the surface is covered with roughly hemispherical shaped craters whose dimensions are of the order of a few millimeters.

4. Nighttime and Eclipse Study of the Moon

4.1 The Thermal Anomalies

The observation of anomalous cooling in certain regions of the lunar surface by Shorthill et al. (1960) has given rise to much speculation about the origin of these anomalies (Fig. 20). Several possible explanations suggested by Saari and Shorthill (1963) are presented in the Introduction. The one most generally accepted concerns the bulk properties of a lunar surface. The point is that a denser material will have a larger thermal inertia and hence a longer cooling time during a lunar eclipse. Thus one interpretation is that the material in the region of a hot spot is denser than the surrounding region. A variation of this idea is based on a two-layer model for the surface in which a decrease in the thickness of the overlying dust layer produces a surface that cools more slowly. In both these models the surface itself is assumed to be flat.

Another line of reasoning attributes the anomalous cooling to surface roughness (Winter 1965 and Bastin 1965). In this model a region of rough surface is constructed on a uniform density material. The slots or grooves of the roughness model cause the surface to cool less rapidly due to the "excavation" of heat from deeper material by radiation conductivity. Thus the effective thermal inertia of the surface is increased by the presence of roughness.

In Section II we have proposed as a possible alternative to the previous suggestions that the thermal anomalies are a region densely covered with very deep spherical craters. The anomalies that were observed by Saari and Shorthill (1963) are associated

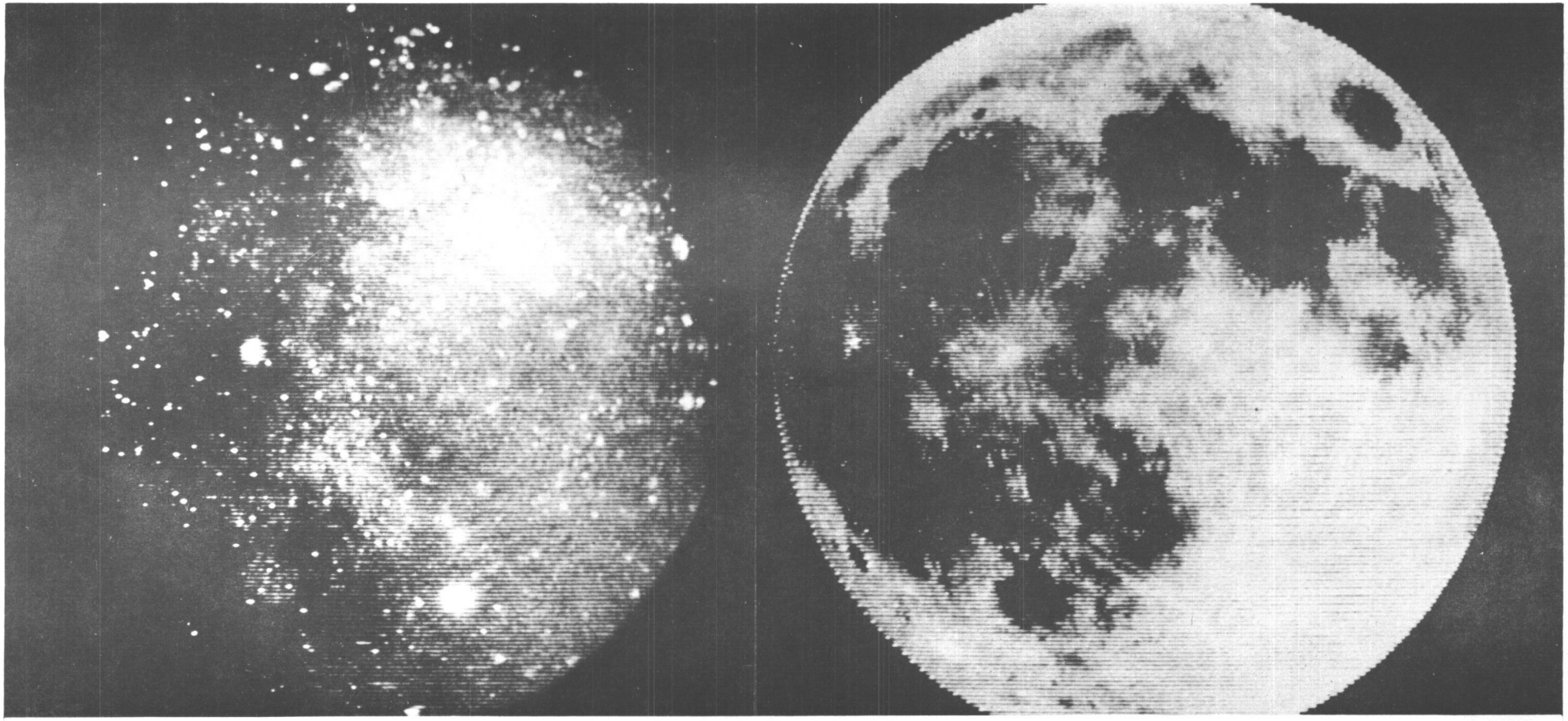

Infrared (10 — 12 μ)

Visible

FIG. 20. Thermal anomalies on the eclipsed Moon (Shorthill and Saari)

almost entirely with bright-rayed craters. There is evidence that the rays are made up of many small secondary craters (Rackham 1965). We therefore propose that the anomaly is caused by numerous deep craters located in and around the much larger parent crater and that these probably are produced by debris from the initial meteor impact. This would help to explain the fact that the anomalies are larger generally in diameter than the associated crater.

These deep craters would provide excavation of heat from the deeper layers similar to the previous models. As in the study of the illuminated Moon, the effects of reradiation on the temperature of the crater are considered here; and, in addition, the flux conducted up up from beneath the surface is taken into account because it determines the rate of cooling of the crater. This is accomplished by using Eqs. 22 (a — h) in a numerical diffusion calculation. The method developed by Wesselink (1948) to study the cooling of a smooth, flat surface can be adapted easily to a lunar crater.

4.2 Numerical Solution for the Cooling of a Crater

The Wesselink procedure is a numerical technique for solving a diffusion problem. Mathematically this can be stated as a boundary value problem where the differential equation is:

$$\frac{d^2T}{dz^2} - \frac{1}{K}\frac{dT}{dt} = 0 \qquad K = \frac{k}{pc} \tag{50}$$

This diffusion equation can be transformed into a finite difference equation as follows:

$$\frac{T(t, z+\Delta z) - 2T(t,z) + T(t, z-\Delta z)}{(\Delta z)^2} - \frac{1}{K}\frac{T(t+\Delta t, z) - T(t,z)}{\Delta t} = 0 \tag{51}$$

It is convenient to select the Δt and Δz increments such that

$$(\Delta z)^2 = 2K\Delta t \tag{52}$$

Substituting Eq. 52 into Eq. 51 and multiplying by $K\Delta t$, the $T(t, z)$ terms cancel leaving:

$$T(t+\Delta t, z) = \tfrac{1}{2}\left(T(t, z+\Delta z) + T(t, z-\Delta z)\right) \tag{53}$$

Thus the diffusion equation simply gives the temperature at time $t+\Delta t$ as the average of two temperatures at time t.

Starting at some initial temperature distribution one can then theoretically obtain the complete temperature history at any depth, provided that the boundary conditions are supplied. Since one wants to to terminate the diffusion process at a finite depth, the boundary condition at $N\Delta z$ is chosen as a constant temperature equal to the average lunar temperature. Because of the exponentially damped behavior of the diffusion, this is not a serious error for an $N\Delta z$ of about one thermal wavelength. The thermal wavelength for a sinuisoidally heated boundary is just:

$$\lambda = 2\pi\sqrt{2K/\omega} \qquad \omega = \frac{2\pi}{P} \tag{54}$$

Using this with Eq. 52 gives the z-increment in thermal wavelengths as:

$$\frac{\Delta z}{\lambda} = \frac{1}{2\pi}\sqrt{\omega \Delta t} = \sqrt{\frac{1}{2\pi}\left(\frac{\Delta t}{P}\right)} \approx 0.4\left(\frac{\Delta t}{P}\right)^{\frac{1}{2}} \tag{55}$$

For the crater problem we chose to split the lunar cycle (29.5 days) into 100 increments, which gives a z-increment of:

$$\begin{aligned} \Delta z &= 0.04\ \lambda \\ \Delta t &= 0.01\ P \end{aligned} \tag{56}$$

An array of 25 z-increments by 500 increments in time was chosen (Fig. 21) because it allowed the crater to go through 5 lunation cycles. It was discovered, however, that 2 cycles were sufficient for convergence of the surface temperature when started at a constant temperature at all depths.

The calculation of the cooling of a lunar crater begins with the computation of the average cooling. The boundary condition at the surface ($z = 0$) is a flux balance and, as such, is a gradient condition on the temperature (Eq. 22f)

$$\bar{f}_c = k\frac{d\bar{T}}{dz} = k\frac{\Delta \bar{T}}{\Delta z} \tag{57}$$

which, in terms of the thermal wavelength, is:

$$\bar{f}_c = \frac{k}{\lambda}\frac{\Delta \bar{T}}{0.04} \qquad \frac{\Delta z}{0.04} = 0.04 \tag{58}$$

I	T1	T2	T3	T4	T5	T6	T7	T8	T9	T10	T11	T12	T13	T14	T15	T16	T17	T18	T19	T20	T21	T22	T23	T24	T25
1	230	230	230	230	230	230	230	230	230	230	230	230	230	230	230	230	230	230	230	230	230	230	230	230	230
2	230	230	230	230	230	230	230	230	230	230	230	230	230	230	230	230	230	230	230	230	230	230	230	230	230
3	252	230	230	230	230	230	230	230	230	230	230	230	230	230	230	230	230	230	230	230	230	230	230	230	230
4	271	252	230	230	230	230	230	230	230	230	230	230	230	230	230	230	230	230	230	230	230	230	230	230	230
5	286	260	241	230	230	230	230	230	230	230	230	230	230	230	230	230	230	230	230	230	230	230	230	230	230
6	299	276	245	235	230	230	230	230	230	230	230	230	230	230	230	230	230	230	230	230	230	230	230	230	230
7	310	283	246	237	232	230	230	230	230	230	230	230	230	230	230	230	230	230	230	230	230	230	230	230	230
8	320	296	260	244	233	231	230	230	230	230	230	230	230	230	230	230	230	230	230	230	230	230	230	230	230
9	329	302	270	247	237	231	230	230	230	230	230	230	230	230	230	230	230	230	230	230	230	230	230	230	230
10	337	313	274	254	239	234	230	230	230	230	230	230	230	230	230	230	230	230	230	230	230	230	230	230	230
11	344	317	283	257	244	235	232	230	230	230	230	230	230	230	230	230	230	230	230	230	230	230	230	230	230
12	350	326	287	263	246	238	232	231	230	230	230	230	230	230	230	230	230	230	230	230	230	230	230	230	230
13	356	330	295	266	251	239	234	231	230	230	230	230	230	230	230	230	230	230	230	230	230	230	230	230	230
14	361	338	298	273	253	242	235	232	230	230	230	230	230	230	230	230	230	230	230	230	230	230	230	230	230
15	365	340	305	275	258	244	237	233	231	230	230	230	230	230	230	230	230	230	230	230	230	230	230	230	230
16	369	347	308	282	260	247	238	234	231	230	230	230	230	230	230	230	230	230	230	230	230	230	230	230	230
17	373	349	314	284	264	249	241	235	232	231	230	230	230	230	230	230	230	230	230	230	230	230	230	230	230
18	376	355	316	289	266	253	242	237	233	231	230	230	230	230	230	230	230	230	230	230	230	230	230	230	230
19	378	356	322	291	271	254	245	237	234	231	230	230	230	230	230	230	230	230	230	230	230	230	230	230	230
20	380	361	324	297	273	258	246	239	234	232	231	230	230	230	230	230	230	230	230	230	230	230	230	230	230
21	382	361	329	298	277	259	249	240	236	232	231	230	230	230	230	230	230	230	230	230	230	230	230	230	230
22	384	365	330	303	279	263	250	242	236	233	231	230	230	230	230	230	230	230	230	230	230	230	230	230	230
23	385	366	334	304	283	264	252	243	238	234	232	231	230	230	230	230	230	230	230	230	230	230	230	230	230
24	385	369	335	309	284	268	253	245	238	235	232	231	230	230	230	230	230	230	230	230	230	230	230	230	230
25	385	368	339	310	288	269	256	244	240	235	233	231	230	230	230	230	230	230	230	230	230	230	230	230	230
26	385	370	339	313	289	272	257	248	241	236	233	232	231	230	230	230	230	230	230	230	230	230	230	230	230
27	385	369	342	314	293	273	260	249	242	237	234	232	231	230	230	230	230	230	230	230	230	230	230	230	230
28	384	371	341	317	294	277	261	251	243	238	234	232	231	230	230	230	230	230	230	230	230	230	230	230	230
29	382	369	344	317	297	277	264	252	245	239	235	233	231	230	230	230	230	230	230	230	230	230	230	230	230
30	381	369	343	320	297	280	265	254	245	240	236	233	232	231	230	230	230	230	230	230	230	230	230	230	230
31	379	367	345	320	300	281	267	255	247	240	237	234	232	231	230	230	230	230	230	230	230	230	230	230	230
32	376	367	344	323	301	284	268	257	248	242	237	234	232	231	230	230	230	230	230	230	230	230	230	230	230
33	373	364	345	322	303	284	271	258	250	242	238	235	233	231	231	230	230	230	230	230	230	230	230	230	230
34	370	363	343	324	303	287	271	260	250	244	239	235	233	232	231	230	230	230	230	230	230	230	230	230	230
35	366	359	344	323	306	287	274	261	252	244	240	236	234	232	231	230	230	230	230	230	230	230	230	230	230
36	361	358	341	325	305	290	274	263	252	246	240	237	234	232	231	230	230	230	230	230	230	230	230	230	230
37	356	352	341	323	307	290	276	263	254	246	241	237	234	232	231	230	230	230	230	230	230	230	230	230	230
38	351	350	338	324	306	292	276	265	255	248	242	238	235	233	231	231	230	230	230	230	230	230	230	230	230
39	345	344	337	322	308	291	278	266	256	248	243	238	235	233	232	231	230	230	230	230	230	230	230	230	230
40	338	341	333	322	307	293	278	267	257	250	243	239	236	234	232	231	230	230	230	230	230	230	230	230	230
41	330	334	332	320	308	293	280	268	259	250	244	239	236	234	232	231	230	230	230	230	230	230	230	230	230
42	322	328	327	320	306	294	280	269	259	251	245	240	237	234	232	231	231	230	230	230	230	230	230	230	230
43	312	321	324	317	307	293	282	269	260	252	246	241	237	235	233	232	231	231	230	230	230	230	230	230	230
44	301	313	319	315	305	294	281	271	261	253	246	242	238	235	233	232	231	230	230	230	230	230	230	230	230
45	289	303	314	312	305	293	283	271	262	253	247	242	238	235	233	232	231	230	230	230	230	230	230	230	230
46	274	294	308	310	302	294	282	272	262	255	248	243	239	236	234	232	231	231	230	230	230	230	230	230	230
47	256	280	302	305	302	292	283	272	264	255	249	243	239	236	234	232	231	231	230	230	230	230	230	230	230
48	234	266	293	302	299	292	282	273	264	256	249	244	240	237	234	233	232	231	230	230	230	230	230	230	230
49	203	247	284	296	297	290	283	273	265	256	250	244	240	237	235	233	232	231	230	230	230	230	230	230	230
50	148	221	271	291	293	290	282	274	265	257	250	245	241	238	235	233	232	231	230	230	230	230	230	230	230
51	130	173	246	282	290	287	282	273	266	257	251	245	241	238	235	233	232	231	230	230	230	230	230	230	230
52	130	171	227	273	285	286	280	274	265	258	251	246	242	238	236	234	232	231	231	230	230	230	230	230	230
53	123	158	222	256	280	282	280	273	266	258	252	247	242	239	236	234	233	231	231	230	230	230	230	230	230
54	122	155	207	251	269	280	278	273	266	259	252	247	243	239	236	234	233	232	231	230	230	230	230	230	230
55	119	148	203	238	265	273	276	272	266	259	253	247	243	239	237	234	233	232	231	230	230	230	230	230	230
56	118	146	193	234	256	271	272	271	265	260	253	248	243	240	237	235	233	232	231	231	230	230	230	230	230
57	115	141	190	224	252	264	271	269	265	259	254	248	244	240	238	235	233	232	231	231	230	230	230	230	230
58	114	139	183	221	244	262	266	268	264	260	254	249	244	241	238	236	234	232	231	231	230	230	230	230	230
59	112	135	180	213	241	255	265	265	264	259	254	249	245	241	238	236	234	232	232	231	230	230	230	230	230
60	112	134	174	211	234	253	260	265	262	259	254	250	245	242	238	236	234	233	232	231	230	230	230	230	230
61	110	132	172	204	232	247	259	261	262	258	254	249	246	242	239	236	234	233	232	231	231	230	230	230	230
62	109	130	168	202	226	245	254	260	260	258	254	250	246	242	239	237	235	233	232	231	231	230	230	230	230
63	108	128	166	197	224	240	253	257	259	257	254	250	246	242	239	237	235	233	232	231	231	230	230	230	230
64	108	127	162	195	218	238	248	256	257	257	253	250	246	243	239	237	235	234	232	231	231	230	230	230	230
65	107	125	161	190	217	233	247	253	256	255	253	250	246	243	240	237	235	234	232	231	231	230	230	230	230
66	106	124	158	189	212	232	243	252	254	255	252	250	246	243	240	238	235	234	233	232	231	230	230	230	230
67	105	122	157	185	210	227	242	248	253	253	252	249	247	243	240	238	236	234	233	232	231	231	230	230	230
68	105	122	154	183	206	226	238	248	251	253	251	250	246	244	240	238	236	234	233	232	231	231	230	230	230
69	104	120	153	180	205	222	237	244	250	251	251	249	247	243	241	238	236	234	233	232	231	231	230	230	230
70	103	120	150	179	201	221	233	244	248	251	250	249	246	244	241	239	236	235	233	232	231	231	230	230	230
71	102	118	149	176	200	217	232	240	247	249	250	248	246	243	241	238	237	235	233	232	231	231	230	230	230
72	102	117	147	174	196	216	229	240	245	248	248	248	246	244	241	239	237	235	233	232	232	231	230	230	230
73	101	116	146	171	195	213	228	237	244	246	248	247	246	243	241	239	237	235	234	232	232	231	230	230	230
74	101	115	144	170	192	212	225	236	242	246	247	247	245	244	241	239	237	235	234	233	232	231	230	230	230
75	100	115	143	168	191	208	224	233	241	244	247	246	245	243	241	239	237	235	234	233	232	231	230	230	230
76	100	114	141	167	188	207	221	232	239	244	245	246	244	243	241	239	237	236	234	233	232	231	230	230	230
77	100	113	140	165	187	204	220	230	238	242	245	245	245	243	241	239	237	236	234	233	232	231	231	230	230
78	99	113	139	164	185	204	217	229	236	242	243	245	244	243	241	239	237	236	234	233	232	231	231	230	230
79	98	112	138	162	184	201	216	226	235	239	243	243	244	242	241	239	238	236	235	233	232	231	231	230	230
80	98	111	137	161	181	200	214	226	233	239	241	243	243	243	241	239	237	236	234	233	232	231	231	230	230
81	98	110	136	159	180	197	213	223	232	237	241	242	243	242	241	239	238	236	235	233	232	231	231	230	230
82	98	110	135	158	178	197	210	223	230	237	240	242	242	242	240	239	238	236	235	234	232	232	231	230	230
83	97	110	134	156	177	194	210	220	230	235	240	241	242	241	241	239	238	236	235	234	233	232	231	230	230
84	97	109	133	156	175	194	207	220	228	235	238	241	241	241	240	239	238	236	235	234	233	232	231	230	230
85	97	109	132	154	175	191	207	217	227	233	238	239	241	241	240	239	238	236	235	234	233	232	231	230	230
86	96	108	131	153	173	191	204	217	225	232	236	239	240	241	240	239	237	236	235	234	233	232	231	230	230
87	96	107	131	152	172	189	204	215	225	231	236	238	240	240	240	239	238	236	235	234	233	232	231	230	230
88	96	107	130	151	170	188	202	214	223	230	234	238	239	240	239	239	237	236	235	234	233	232	231	230	230
89	95	107	129	150	170	186	201	212	222	229	234	237	239	239	239	238	238	236	235	234	233	232	231	230	230
90	95	106	128	150	168	185	199	212	220	228	233	237	238	239	239	238	237	236	235	234	233	232	231	230	230
91	95	106	128	148	167	184	199	210	220	226	232	235	238	238	239	238	237	236	235	234	233	232	231	230	230
92	95	106	127	148	166	183	197	209	218	226	231	235	237	238	238	238	237	236	235	234	233	232	231	230	230
93	94	105	127	146	165	181	196	207	218	224	231	234	237	237	238	238	237	236	235	234	233	232	231	230	230
94	94	104	126	146	164	181	194	207	216	224	229	234	236	237	238	238	237	236	235	234	233	232	231	230	230
95	94	104	125	145	163	179	194	205	216	223	229	232	236	237	238	237	237	236	235	234	233	232	231	230	230
96	93	104	125	144	162	179	192	205	214	222	227	232	234	237	237	237	237	236	235	234	233	232	231	230	230
97	93	103	124	143	161	177	192	203	213	221	227	231	234	236	237	237	237	236	235	234	233	232	231	230	230
98	93	103	123	143	160	176	190	203	212	220	226	231	233	236	236	237	236	236	235	234	233	232	231	230	230
99	92	102	123	142	160	175	190	201	211	219	226	230	233	235	236	236	236	236	235	234	233	232	231	230	230
100	92	102	122	141	158	175	188	200	210	219	224	229	232	235	235	236	236	236	235	234	233	232	231	230	230

FIG. 21. Temperature array

Using Eq. 54 and the definition of K

$$\overline{f}_c = \frac{(k\rho c)^{\frac{1}{2}}\ \omega^{\frac{1}{2}}}{2\pi\sqrt{2}}\ \frac{\Delta\overline{T}}{0.04} = \frac{(k\rho c)^{\frac{1}{2}}}{(4\pi P)^{\frac{1}{2}}}\ \frac{\Delta\overline{T}}{0.04} \tag{59}$$

and combining this with Eq. 22b, the non-linear boundary condition for the average cooling of the crater is:

$$\sigma\,\overline{T^4}\,(0,\ t) = f_s\ \tfrac{1}{2}\,(\cos\omega t + |\cos\omega t|\,) + \frac{A_c}{A_a}\ \frac{50\,(k\rho c)^{\frac{1}{2}}}{(4\pi\ P)^{\frac{1}{2}}}\ \left(\overline{T}(\tfrac{1}{2}\,\Delta z,\ t) - \overline{T}\,(0,\ t)\right) \tag{60}$$

where $\omega t = \theta_o$. The solar flux term has been modified so that it automatically becomes Eq. 22d for the dark region. An extra factor of 2 appears in the second term due to the half increment in z that is used to improve accuracy. In effect, the whole temperature array is shifted $\frac{1}{2}$ increment toward the surface, making $T(-\frac{1}{2}\Delta z, t)$ $\frac{1}{2}$ increment above the surface.

In order to solve the fourth-order boundary condition (Eq. 60) the approximation must be made that:

$$\overline{T^4}\ (0,\ t) = \left(\overline{T}\ (0,\ t)\right)^4 \tag{61}$$

Using the temperature profiles that are obtained during the lunar night, it is shown in Appendix VII that such an approximation causes an error of less than 1° K in the final temperatures. This error is small considering the accuracy of the numerical procedure that was used to calculate the surface temperature was 1° K.

The average cooling of the crater now can be obtained using Eqs. 53 and 60 on the computer (Fig. 22). The procedure consists basically of three steps. First, the temperature at time $t + \Delta t$ and depth z is given by Eq. 53 as the average of the two temperatures located diagonally above it in the array. Since all of the temperatures in the previous row are known, Eq. 53 gives all of the temperatures in the next row, with the exception of two located at the boundary of the array. The right boundary was chosen as a constant temperature. Second, $\overline{T}\ (0,t)$ is obtained numerically from the fourth-order boundary condition, (Eq. 60). Finally, the missing term in the array is obtained by assuming a linear slope in temperature between increments as follows

$$\overline{T}\left(-\tfrac{1}{2}\Delta z,\ t\right) = 2T\ (0,t) - T\ (\tfrac{1}{2}\Delta z, t) \qquad (62)$$

giving the temperature at the left boundary of the array. This process is repeated, each time filling up a row of the array and, in addition, incrementing the solar flux by 1/100 of its period.

Using the procedure outlined here it is possible to determine completely the temperature of any point in the crater for the entire lunation period. We have demonstrated in detail how the average lunation cooling has been determined. A completely analogous method is used to determine the history of a point in the crater using Eq. 22 (a, c, and e). Eqs. 22a and 22c become transformed in the same way as Eq. 60, where the angle of incidence is $\psi = \omega t + \alpha$ (Fig. 8a):

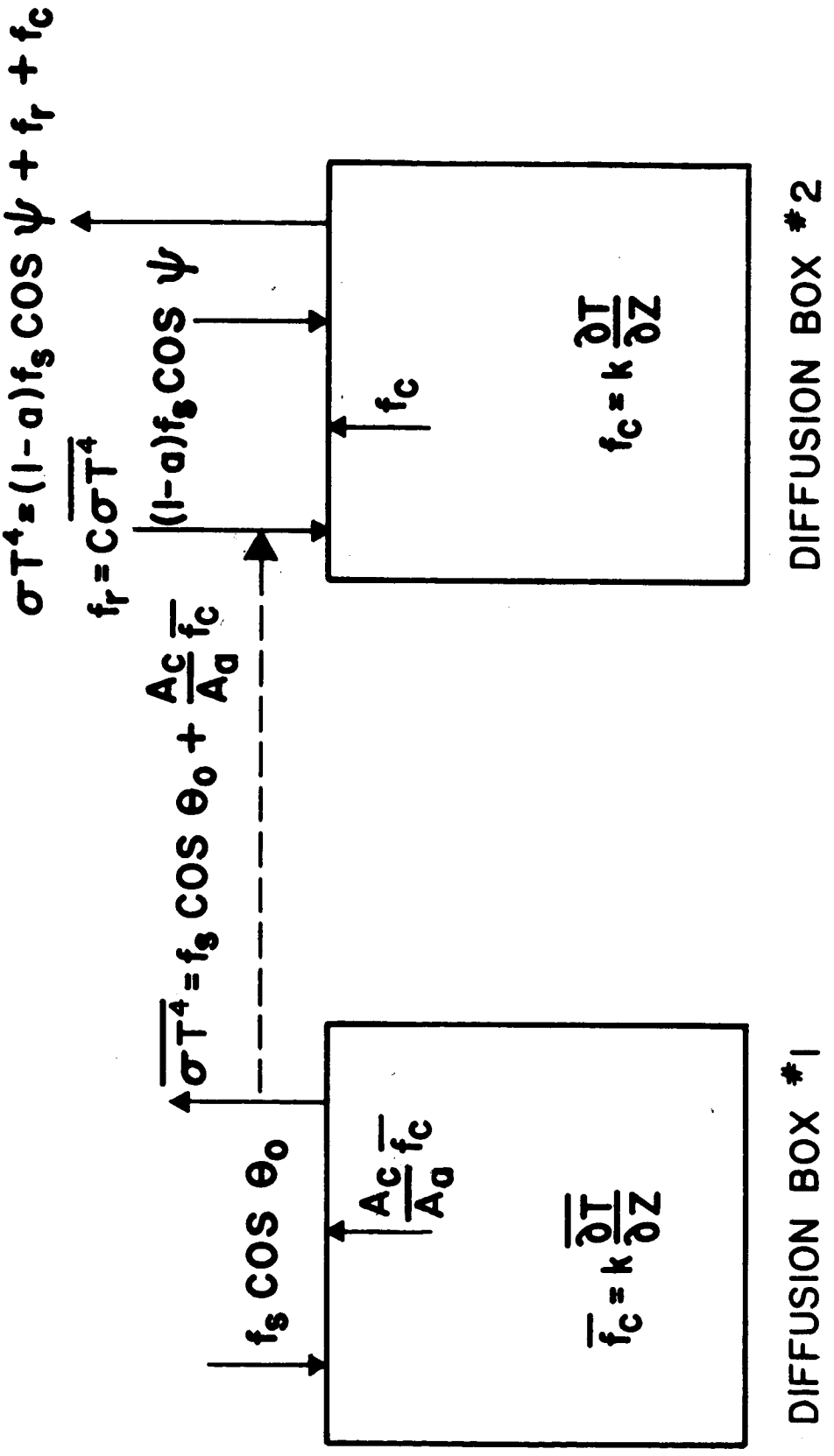

FIGURE 22
DIAGRAM OF COMPUTER CALCULATION

$$\sigma T^4 (0,t) = (1 - a) f_s \cos(\omega t + \alpha) + C \sigma \overline{T^4}(0, t) + \frac{50 (k\rho c)^{\frac{1}{2}}}{(4\pi P)^{\frac{1}{2}}} \left(T (\tfrac{1}{2} \Delta z, t) - T (0, t)\right) \text{ Illuminated Region}$$

$$\sigma T^4 (0, t) = C \sigma \overline{T^4}(0, t) + \frac{50 (k\rho c)^{\frac{1}{2}}}{(4\pi P)^{\frac{1}{2}}} \left(T (\tfrac{1}{2}\Delta z, t) - T (0, t)\right) \text{ Dark or shadowed region} \tag{63}$$

The combination of Eqs. 63 and 53 are used in a second numerical diffusion to solve for the temperature of a point. Thus by making N + 1 diffusion calculations one can obtain the thermal history of a lunar crater for N points within the crater.

The original equations for describing the temperature distribution in a crater have been reduced to numerical form to be used in a computer solution for the cooling of a crater. The forms of the equations to be used on the computer are:

$$\sigma \overline{T^4} (0, t) = \frac{f_s}{2} (\cos \omega t + |\cos \omega t|) + \frac{A_c}{A_a} \frac{50 (k\rho c)^{\frac{1}{2}}}{(4\pi P)^{\frac{1}{2}}} \left(\overline{T} (\tfrac{1}{2}\Delta z, t) - \overline{T} (0, t)\right) \tag{a}$$

(64)

$$\overline{T} (t + \Delta t, z) = \tfrac{1}{2} \left(\overline{T} (t, z + \Delta z) + \overline{T} (t, z - \Delta z)\right) \tag{b}$$

Illuminated Region:

$$\sigma T^4 (0, t) = (1 - a) f_s \cos (\omega t + \alpha) + C \sigma \overline{T^4} (0, t)$$

$$+ \frac{50\,(k\rho c)^{\frac{1}{2}}}{(4\pi P)^{\frac{1}{2}}} \left(T\left(\tfrac{1}{2}\Delta z,\ t\right) - T\,(0,\ t) \right) \qquad (c)$$

Dark or Shadowed Region: (64)

$$\sigma T^4\,(0,\ t) = C\,\sigma\overline{T^4}\,(0,t) + \frac{50\,(k\rho c)^{\frac{1}{2}}}{(4\pi P)^{\frac{1}{2}}} \left(T\left(\tfrac{1}{2}\Delta z,\ t\right) - T\,(0,t) \right) \qquad (d)$$

$$T\,(t+\Delta t,\ z) = \tfrac{1}{2}\left(T\,(t,\ z+\Delta z) + T\,(t,\ z-\Delta z) \right) \qquad (e)$$

The average cooling array (Fig. 21) is calculated first, using the radiation balance equation (Eq. 64a) as the boundary condition for the left edge of the array. The top and right-hand boundaries of the array are set equal to the average temperature of the Moon (230° K). The diffusion equation is reduced to a numerical temperature average (Eq. 64b), which is used to obtain the temperature inside the boundary of the array. After the average cooling has been determined, the temperature history of a point within the crater can be evaluated. The shadow region has been derived in Appendix III and requires the direct solar flux to be zero when:

$$\omega t < -90 + \gamma/4 - \alpha/2 \qquad (\theta_o < \theta_a)$$

$$\omega t > 90 - \gamma/4 - \alpha/2 \qquad (\theta_o > \theta_b) \qquad (65)$$

This condition is then used to tell the computer when to switch from Eq. 64c to Eq. 64d. The reradiation term ($\overline{T^4}$) has been calculated already; therefore, the computer proceeds to determine the temperature variation of a point in the same manner that it determined the average cooling of the crater.

4.3 The Change in Effective Thermal Inertia

The cooling of a lunar crater during an eclipse or lunation can be determined using the theory we have developed. Consideration has been given to the effect of the flux conducted between the surface and the deeper layers as it is no longer negligible, as in the daytime case. The method used for this was developed by Wesselink (1948) for lunation and eclipse studies. Eq. 64a determines the average cooling of the crater and must be calculated before the temperature distribution within the crater can be evaluated using Eq. 64c. The average cooling of the crater is similar to that of a flat surface, except for the factor A_c/A_a, which appears in the conduction term, and this increases the thermal inertia of the flat surface by reducing the amount of flux that the deeper layers of the surface have to provide. Hence, the heat stored in the layers will last longer and cause the surface to cool more slowly. This can be seen in the equations, since the A_c/A_a factor multiplies the thermal inertia in Eq. 64a. Therefore, the average cooling of the crater is slowed by:

$$(k\rho c)^{\frac{1}{2}}_{\text{effective}} = \frac{A_c}{A_a} (k \rho c)^{\frac{1}{2}} \qquad (66)$$

4.4 The Eclipse Illumination Function

Until now, obtaining the lunation cooling curves for the crater has been the primary emphasis. The techniques developed here, however, apply equally well to the eclipse situation. The time scale must be

expanded since an eclipse on the lunar surface takes place in about 5 hours. The path of the Sun behind the Earth is taken along an Earth diameter. During the eclipse the angle of the solar illumination is assumed to be stationary and the initial temperatures in the crater can be obtained directly from Eq. 25a. To evaluate the illumination function that applies it is assumed that the Sun is a uniformly bright disk (no limb darkening) and that the ratio of the diameter of the Earth to the diameter of the Sun as seen from the Moon is 3.58. The illumination then is just proportional to the amount of the solar disc that is visible around the Earth. In Appendix VIII this is shown to be

$$f_e = f_s \left[1 - \frac{1}{2\pi} (\phi_s - \sin \phi_s) - \frac{(3.58)^2}{2\pi} (\phi_e - \sin \phi_e) \right] \tag{67}$$

where

$$\begin{aligned} \sin \frac{\phi_s}{2} &= 3.58 \sin \frac{\phi_e}{2} \\ \cos \frac{\phi_s}{2} &= \frac{1 - (3.58)^2 + 4D^2}{4D} \end{aligned} \tag{68}$$

The apparent motion of the Sun and the Earth as seen from the Moon is such that an observer sees the Earth as fixed in the sky and the Sun as moving at 12.2°/day, returning to the same position in the sky every 29.5 days (708 hours). This motion of 12.2°/day will cause the distance between the centers of the disks of the Sun and the Earth (D in Eq. 68) to change at the rate of 0.954 solar diameters/hour. Thus the full eclipse takes place in 4.8 hours (4.58/0.954), assuming that the Earth passes directly in front of the Sun.

4.5 Numerical Solution for an Eclipse

The procedure for calculating the variation in temperature during an eclipse is the same as that for a lunation except that the illumination function (Eq. 67) is used in place of the cosine variation of solar flux. Hence Eqs. 22 a and 22b become:

$$\sigma T^4 = (1 - a) f_e \cos \psi + C \sigma \overline{T^4} + f_c \tag{69}$$

$$\sigma \overline{T^4} = f_e \cos \theta_o + \frac{A_c}{A_a} f_c \tag{70}$$

As far as the variations in $\cos \psi$ and $\cos \theta_o$ are concerned, the Sun can be assumed to be stationary during the eclipse.

The time scale was chosen to give about 500 intervals during the eclipse. A value of Δt equal to 1/100 of an hour gives a z-increment of (Eq. 55):

$$\Delta z = 1.5 \times 10^{-3} \lambda$$

$$\Delta t = 1.41 \times 10^{-5} P = 0.01 \text{ hours} \tag{71}$$

A temperature array of 25 x 500 was used and the initial temperature (first row) was given a slope equal to the lunation gradient. For simplicity we assumed the Sun to be directly overhead, i.e., the crater is located at the sub-solar point. The resulting non-linear boundary condition for the computer calculation is for the average cooling

$$\sigma \overline{T^4}(0,\ t) = f_e(t) + \frac{A_c}{A_a} \frac{1,330\ (k\rho c)^{\frac{1}{2}}}{(4\pi P)^{\frac{1}{2}}} \left(\overline{T}\ (\tfrac{1}{2}\Delta z,\ t) - \overline{T}\ (0,t) \right) \tag{72}$$

The Sun is at the zenith ($\theta_o = 0$) so that we obtain the temperature for a point an angle α away from the flat surface normal as ($\psi = \alpha + \theta_o$):

$$\sigma T^4\ (0,\ t) = (1 - a)\ f_e(t) \cos\alpha + C\sigma \overline{T^4}(0,t) + \frac{1,330\ (k\rho c)^{\frac{1}{2}}}{(4\pi P)^{\frac{1}{2}}} \left(T\ (\tfrac{1}{2}\Delta z,\ t) - T\ (0,t) \right) \tag{73}$$

Eqs. 72 and 73 together with Eqs. 64b and 64e are used to describe completely the eclipse cooling of a crater. The procedure has been shown in detail already for the average lunation cooling.

In both the lunation and eclipse the average cooling has been modified by an increase in the effective thermal inertia of A_c/A_a, which appears in Eqs. 64a and 72. Thus a surface covered with a sufficient relative density of small, deep craters will be a thermal anomally during an eclipse or during the lunar night. The minimum size limit for the diameter of such craters is determined by the depth of the thermal wave (Fig. 23). In effect the crater can only excavate heat from the deeper layers if its depth is larger than the thermal disturbance. The depth of the thermal disturbance is about 10 z-increments and so the resulting depths are:

$$\begin{aligned} d &= 0.4\,\lambda \quad \text{lunation} \\ d &= 0.015\,\lambda \quad \text{eclipse} \end{aligned} \tag{74}$$

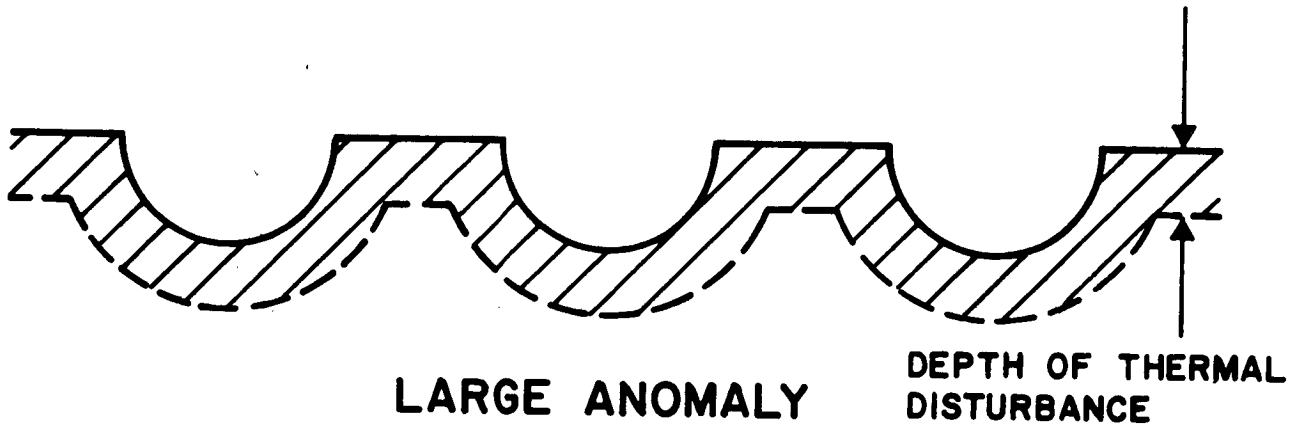

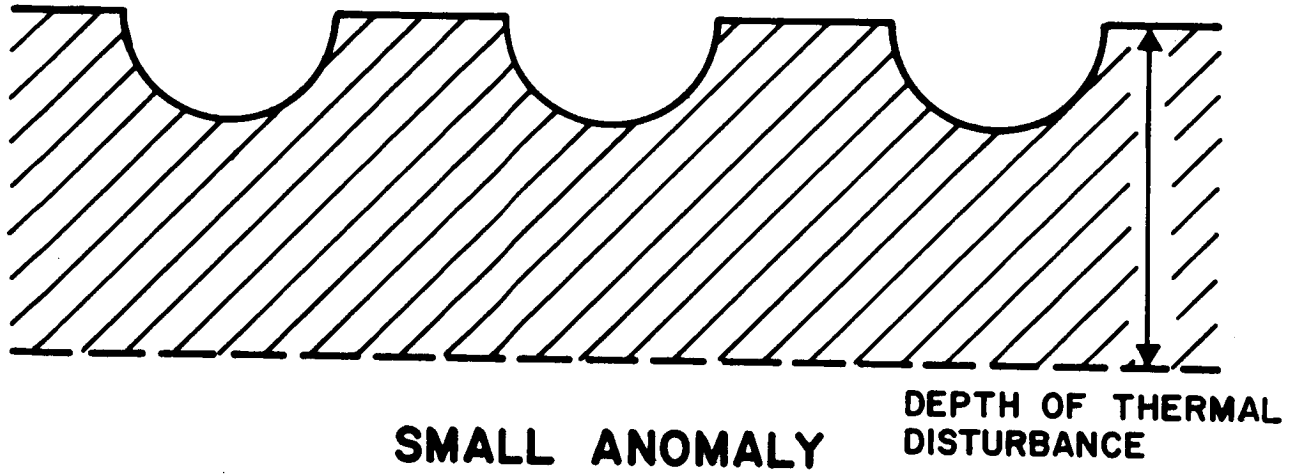

FIGURE 23

EFFECT OF CRATER DIAMETER ON THERMAL ANOMALY

Using a thermal wavelength of 100 cm, the minimum depth required for a crater to affect the thermal inertia becomes 1.5 cm for an eclipse and 40 cm for a lunation. If the craters are hemispherical, this gives a minimum diameter of 3 cm. Hence craters of the order of a few centimeters in diameter can significantly affect the cooling of the lunar surface during an eclipse.

4.6 Lunation and Eclipse Cooling Curves

The method we have developed for treating the cooling of a lunar crater is quite general and depends on very few assumptions. The programs were run on an IBM 7094 and required only about 10 seconds actual computing time for a 5-cycle lunation. To display the cooling of a crater, nine points were chosen within the crater on the cross section containing the Sun's path. This required ten lunation calculations, one for the average cooling and one for each point. The result of the calculations for a 180° crater are shown in Figs. 24 and 25.

The plot of the thermal history of several points (Fig. 24) is shown to illustrate a typical temperature variation during a lunation. Note that the reradiation effect maintains all points in the crater at the same level above the surrounding area at night. The interchange of radiation brings the crater to an equilibrium and produces a 15° K to 20° K anomaly. By looking at a cross-section of the data at a fixed time we have plotted profiles of the crater temperature for both day and night (Figs. 25a and 25b). The daytime temperature profiles show a large variation due to the geometry of the surface. The large temperature variations are important in the

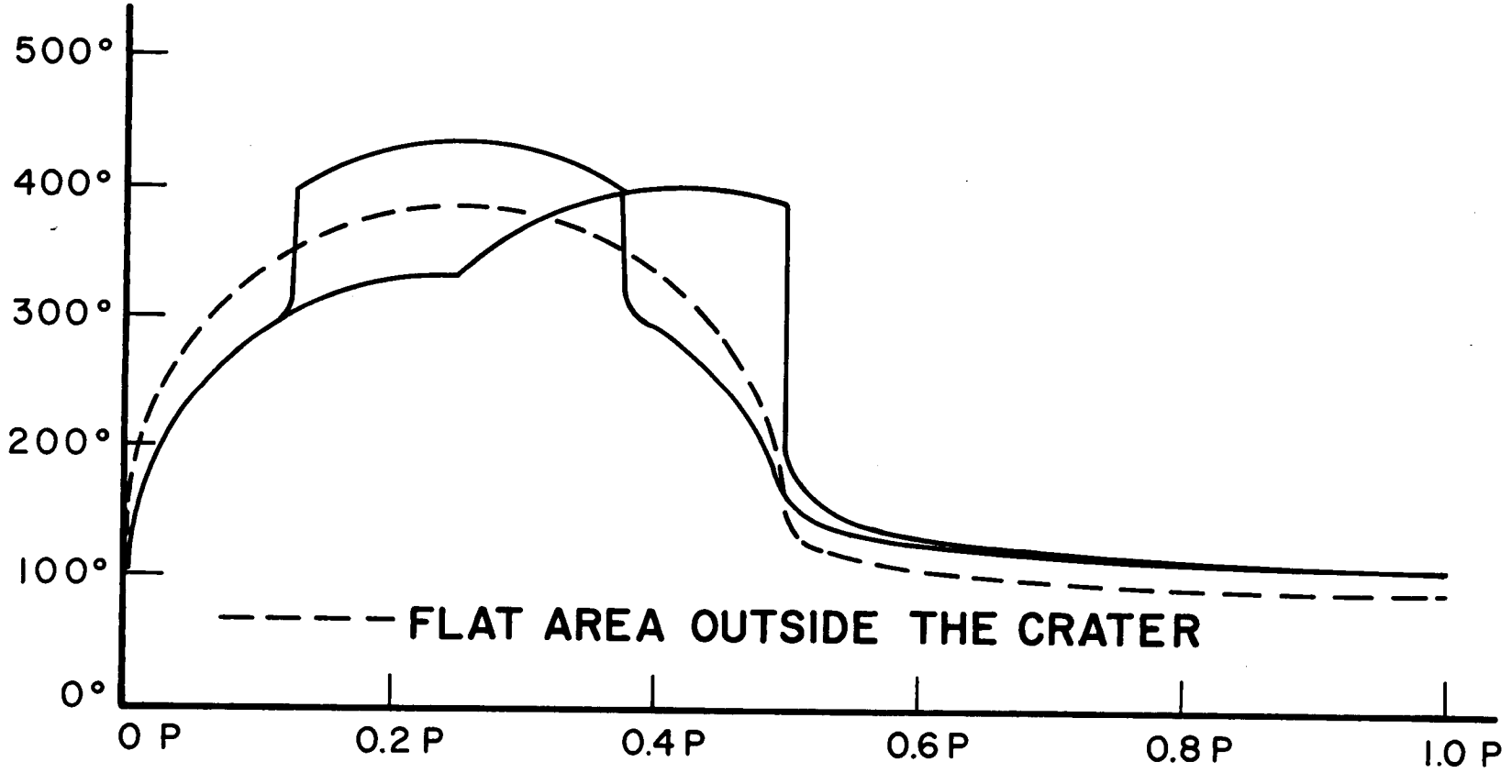

FIGURE 24

TEMPERATURE HISTORY OF A POINT IN THE CENTER AND ONE ON THE RIM OF A HEMISPHERICAL CRATER ($\gamma = 180°$)

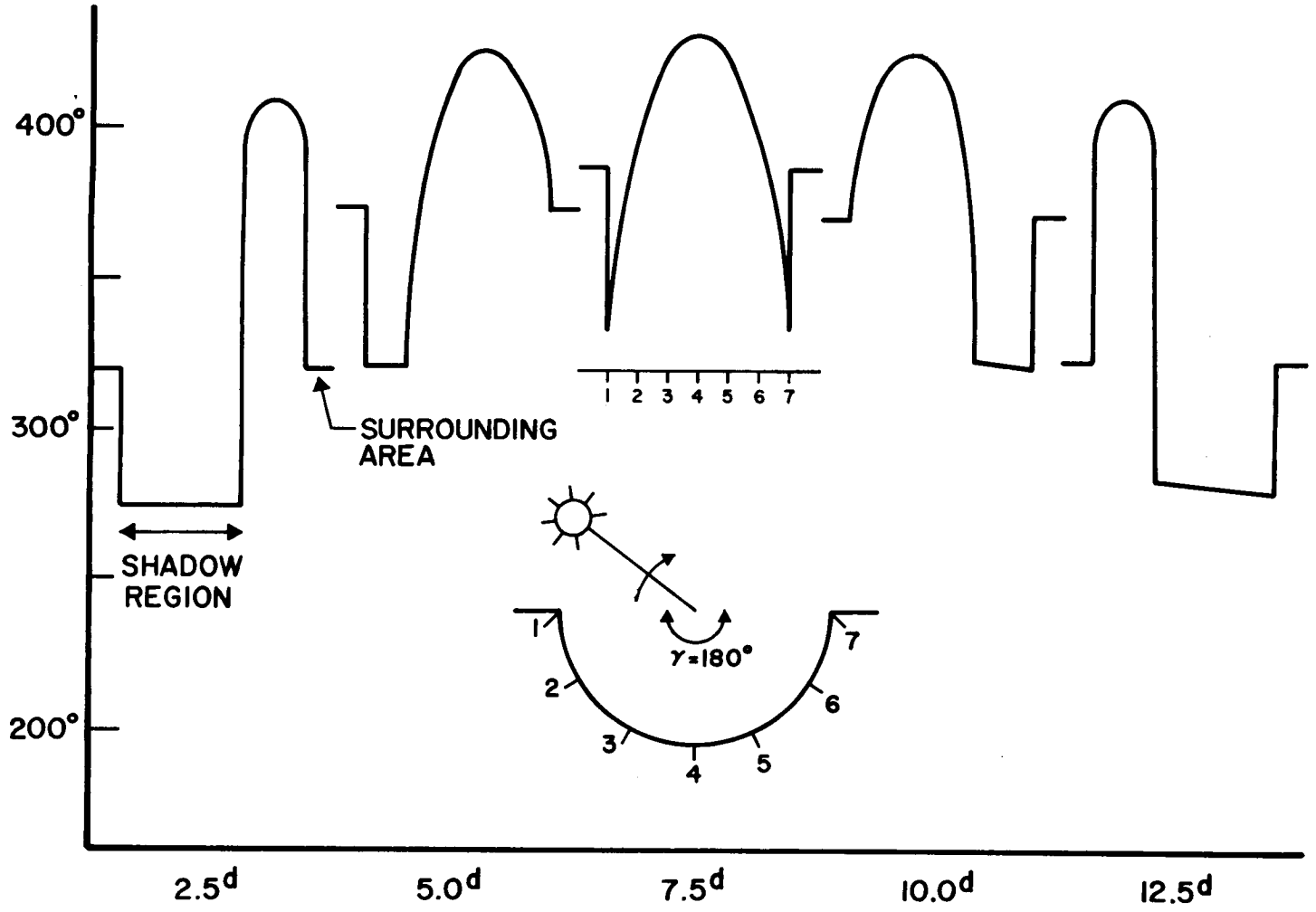

FIGURE 25 a

DAYTIME TEMPERATURE DISTRIBUTION
IN 180° CRATER
(TIME IS IN DAYS AFTER SUNRISE)

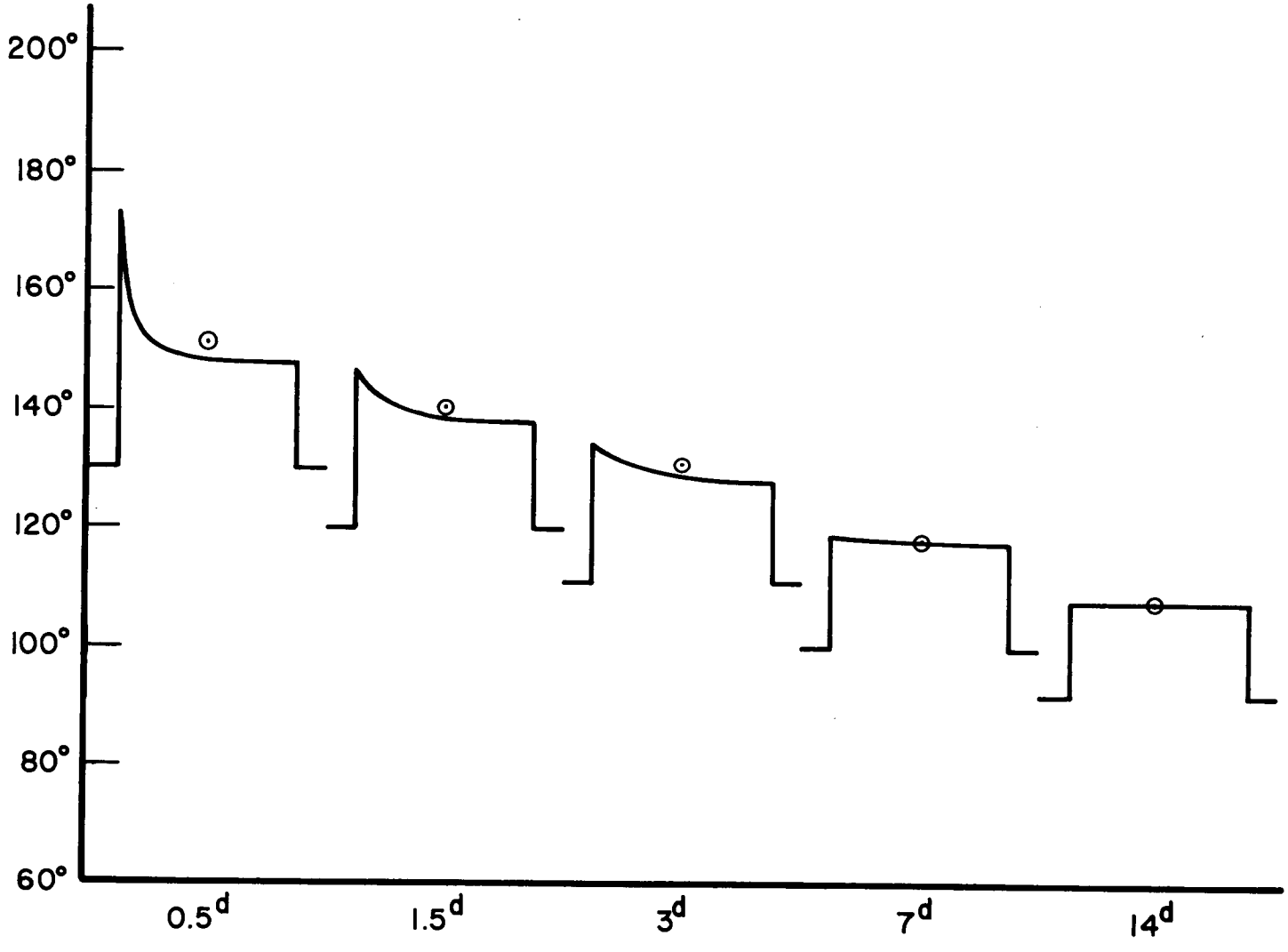

FIGURE 25 b
NIGHTTIME TEMPERATURE DISTRIBUTION
IN 180° CRATER

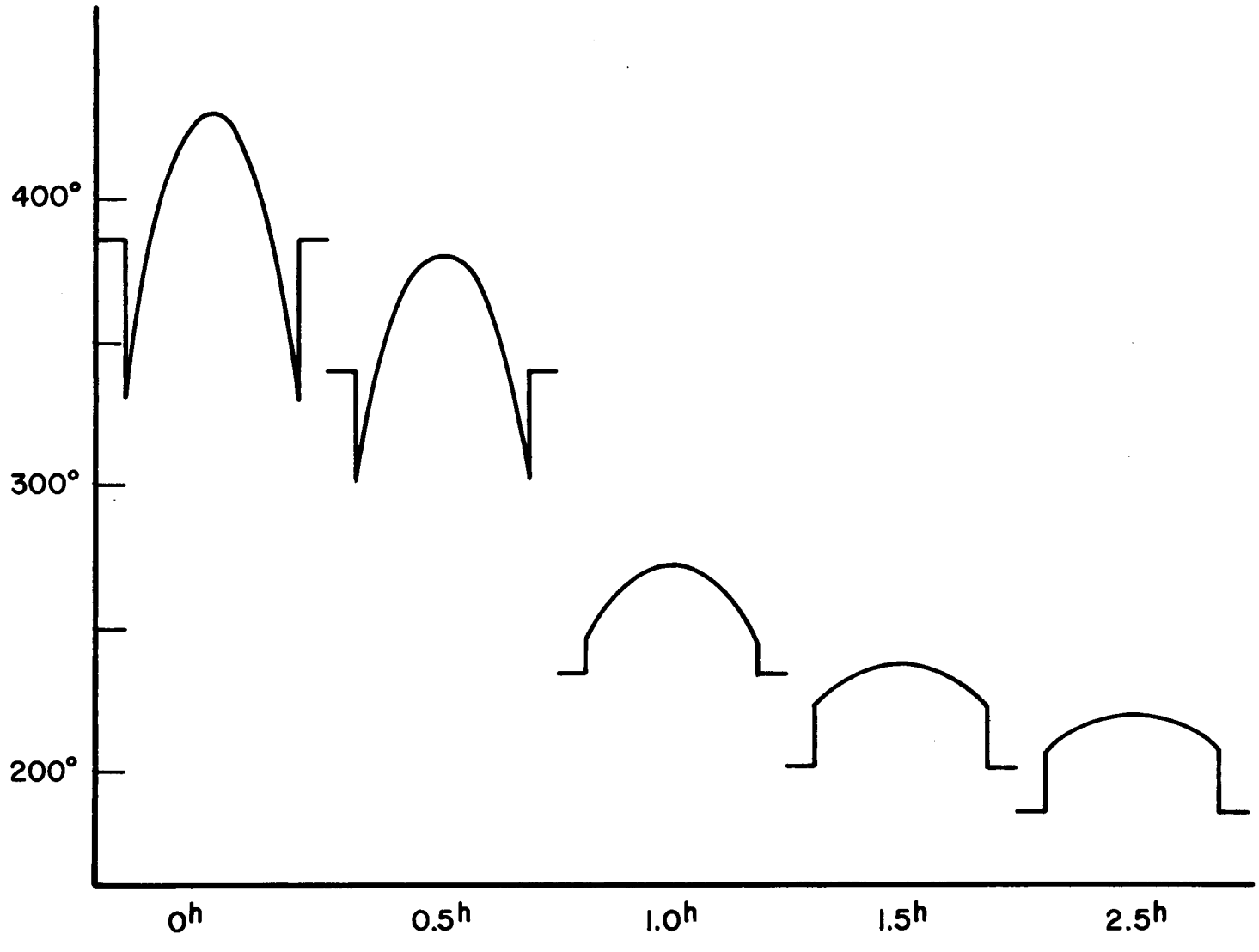

FIGURE 25c

ECLIPSE TEMPERATURE DISTRIBUTION IN 180° CRATER

radiation patterns that we discussed in Section 3. The nighttime cooling profiles show the tilt due to the geometry at sunset slowly coming to an equilibrium by radiation interchange. The average cooling of the crater is indicated for each profile. The fact that the average cooling temperature is equal to the actual crater temperature at dawn is an important check on the theory we have developed.

In a similar way the temperatures in the eclipse cooling profile (Fig. 25c) show some convergence toward an equilibrium value. The process is not as complete as in the lunation case due to the shorter time scale involved. The anomaly produced is about 30° K to 40° K above the surrounding area, and it remains relatively constant throughout the eclipse. Hence the reradiation and excavation of heat are even more pronounced during an eclipse.

We have emphasized the 180° (hemispherical) crater since it produces the largest anomalies that can be modeled with a spherical geometry. Shallower craters, which produce smaller but not insignificant anomalies, are shown in Figs. 26 and 27. These craters take longer to come to equilibrium due to the lower level of reradiation involved.

It is obvious that deeper structures can be modeled with an elliptical or cylindrical geometry. However, the resulting integral equations needed to describe the reradiation flux will be much more difficult to solve (Eq. 36). Following the results obtained here with respect to the increase of thermal inertia (Eq. 66), it seems safe to say that the ratio of crater surface area to aperture or opening area gives a reasonable approximation to the average cooling.

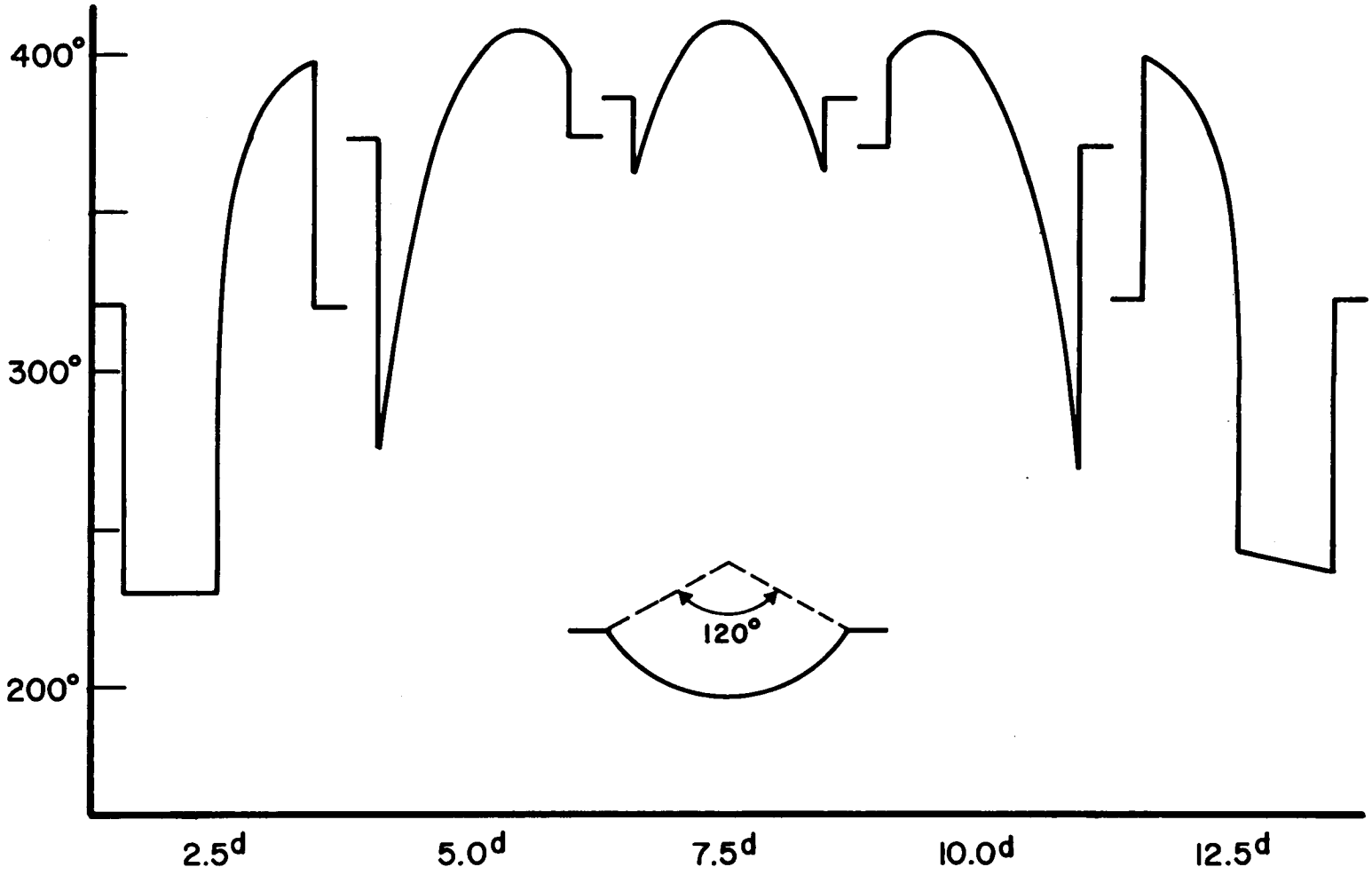

FIGURE 26a

DAYTIME TEMPERATURE DISTRIBUTION IN 120° CRATER

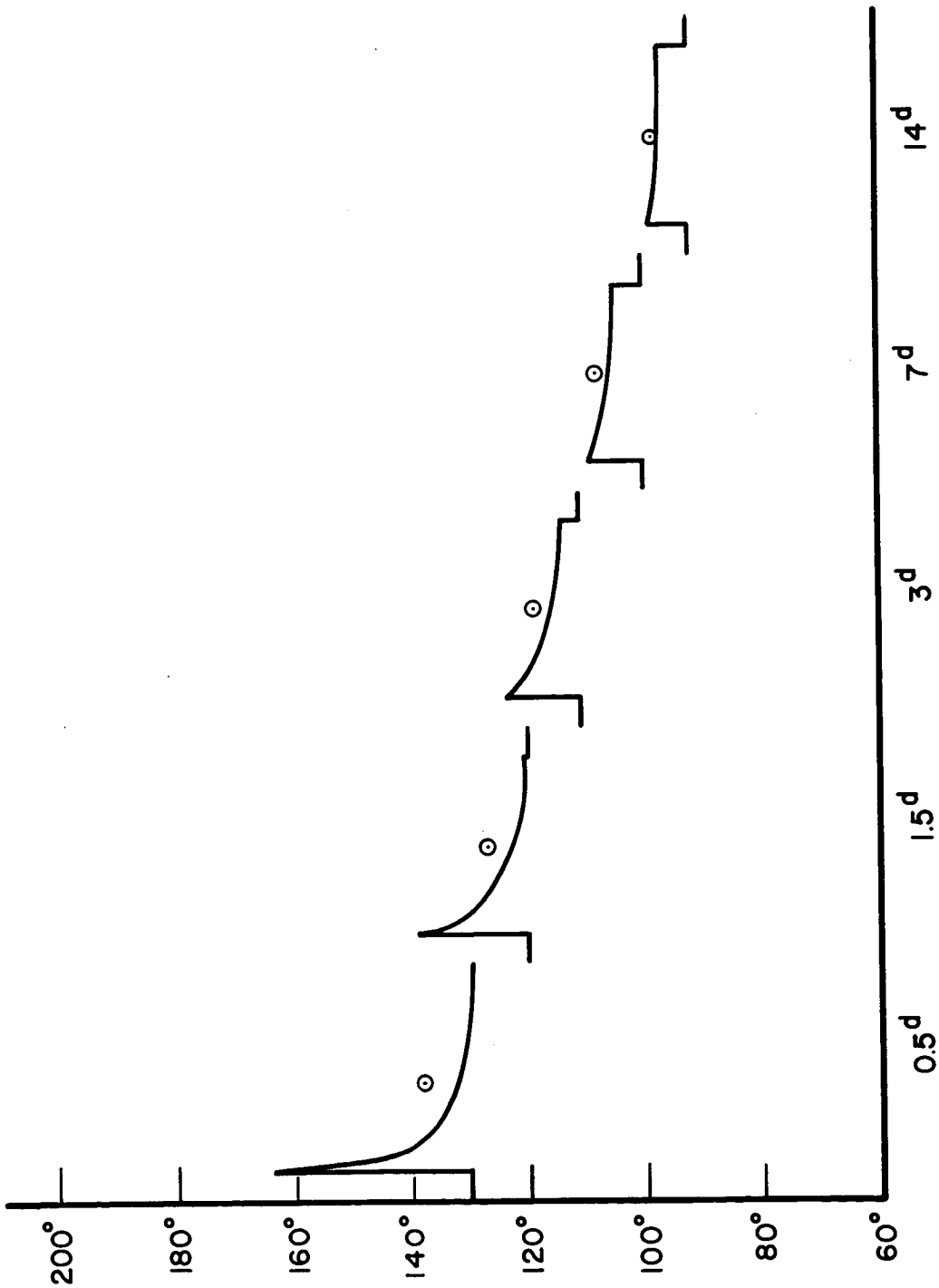

FIGURE 26 b

NIGHTTIME TEMPERATURE DISTRIBUTION IN 120° CRATER

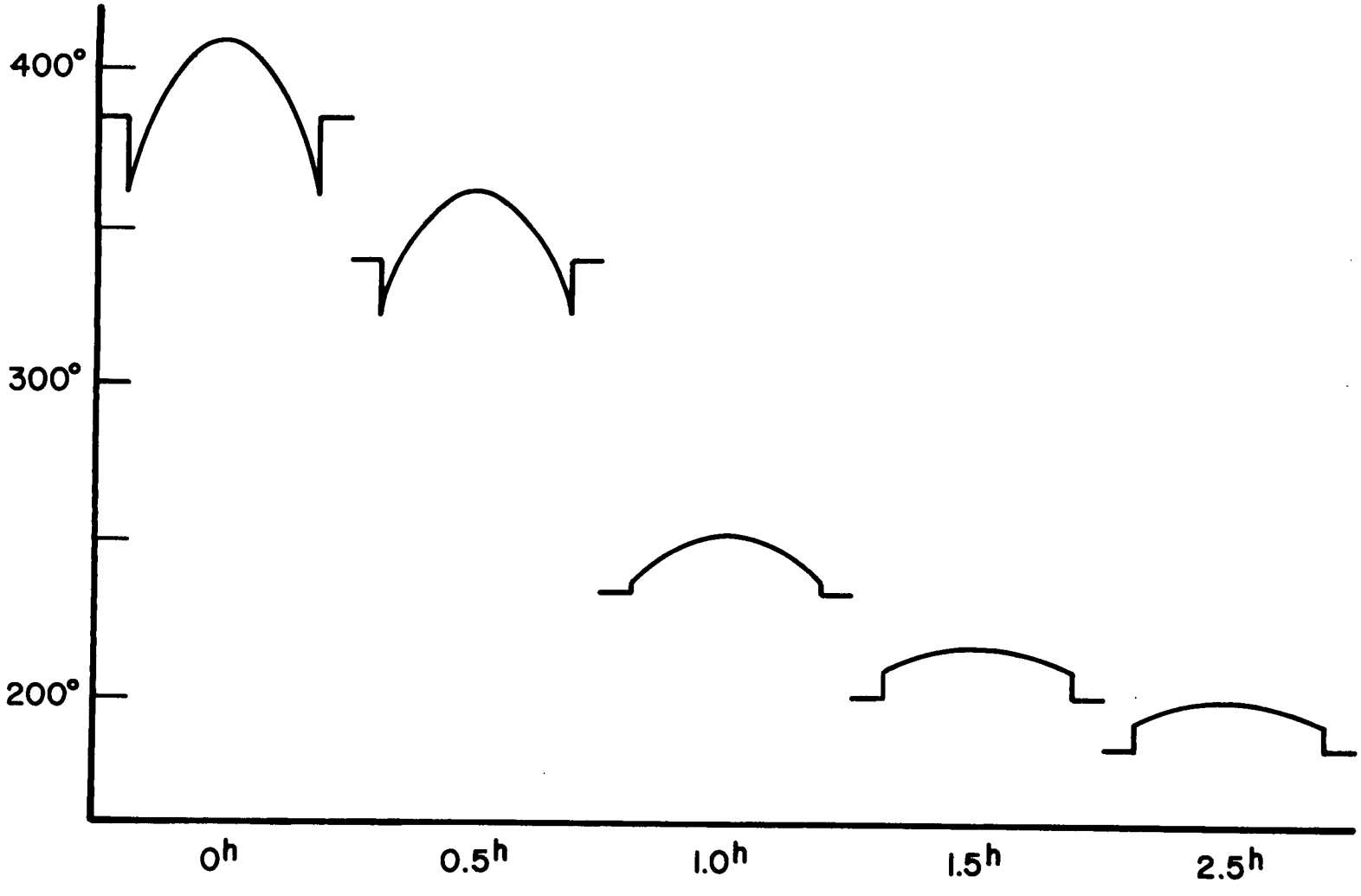

FIGURE 26c
ECLIPSE TEMPERATURE DISTRIBUTION IN 120° CRATER

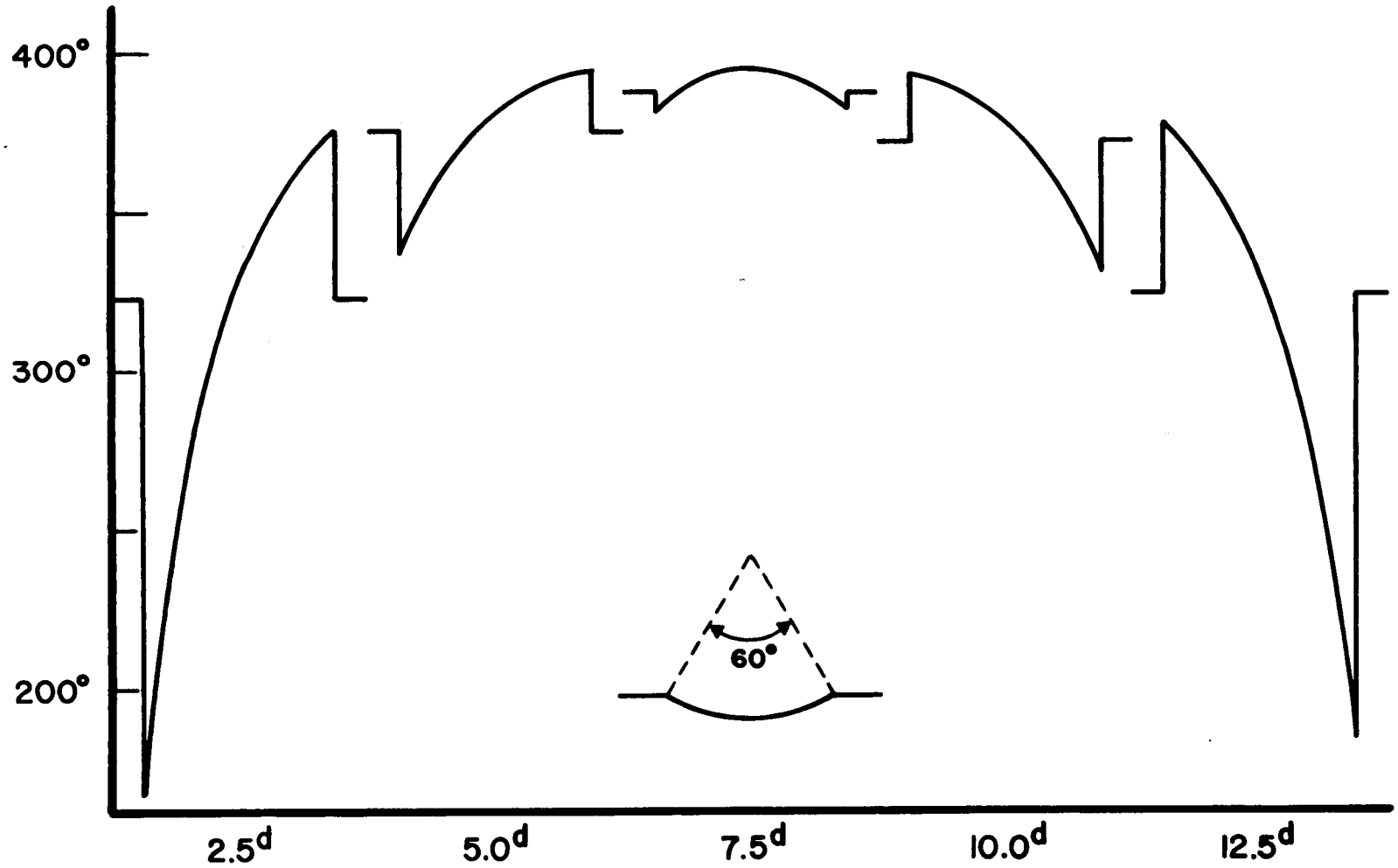

FIGURE 27a

DAYTIME TEMPERATURE DISTRIBUTION IN 60° CRATER

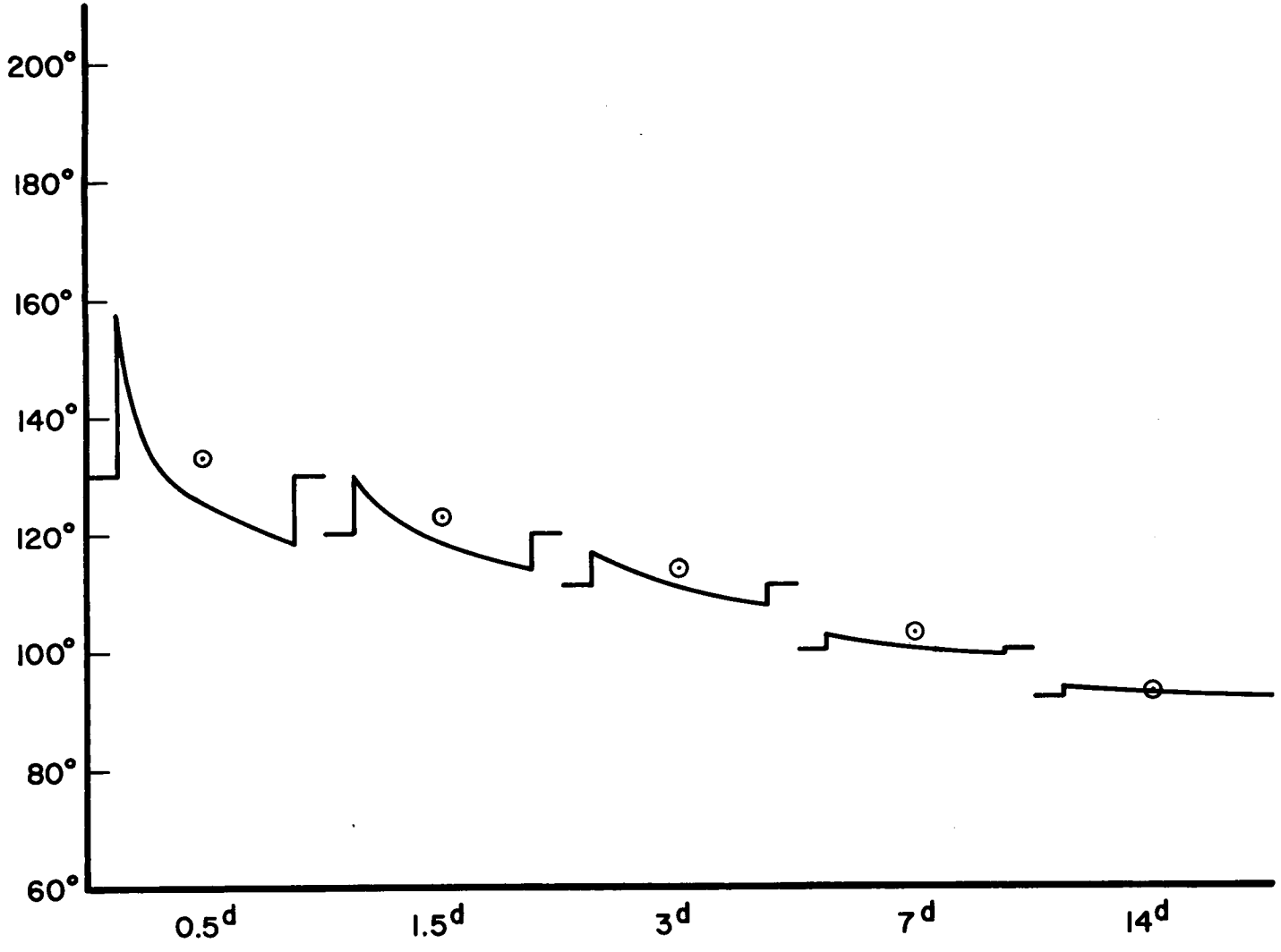

FIGURE 27b

NIGHTTIME TEMPERATURE DISTRIBUTION IN 60° CRATER

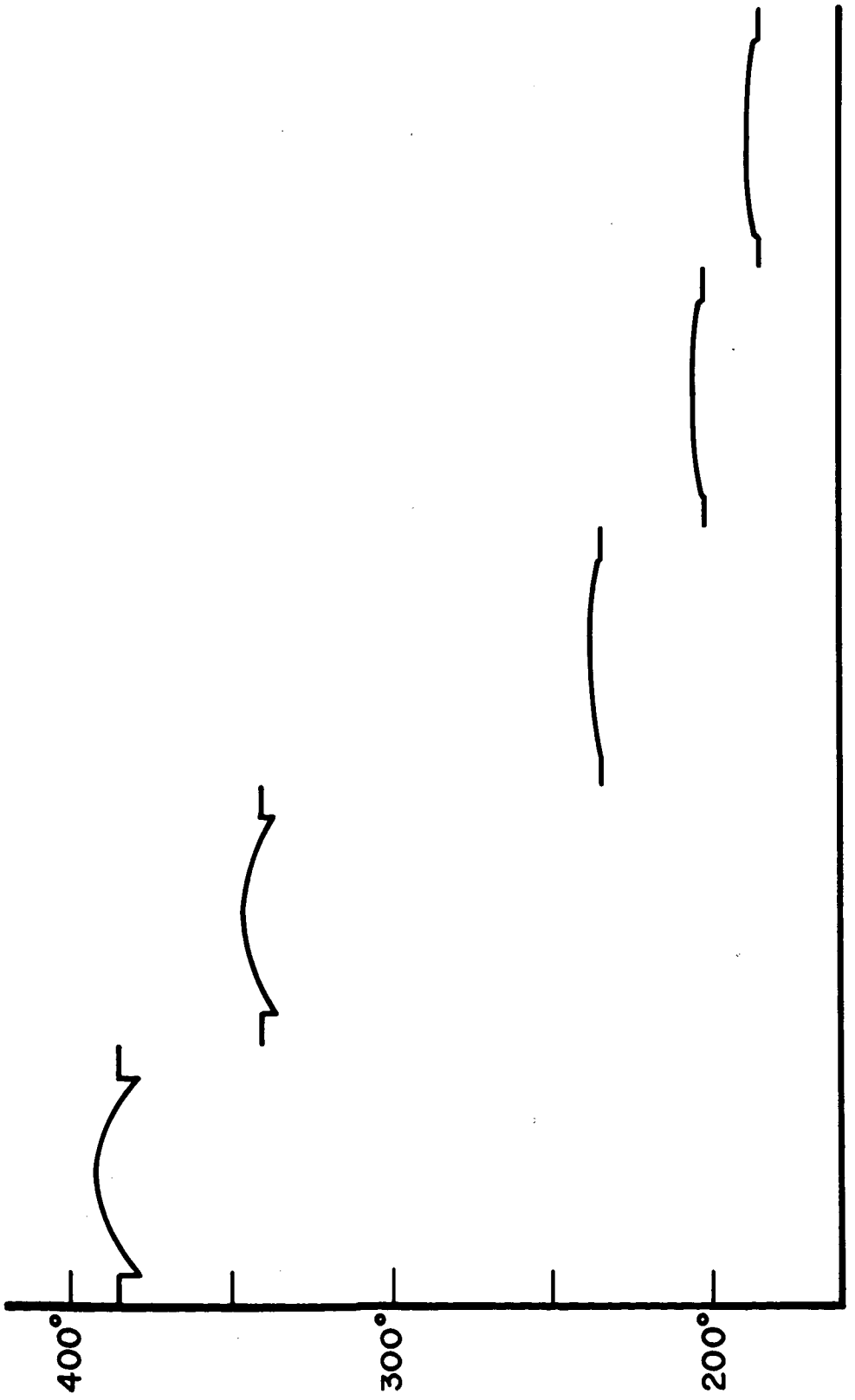

FIGURE 27c

ECLIPSE TEMPERATURE DISTRIBUTION IN 60° CRATER

Hence a hemispherical crater will double the effective thermal inertia of the surface; a cylinder with the same diameter-to-depth ratio will triple the effective thermal inertia; a structure consisting of a cylinder with a hemispherical bottom and a diameter to depth ratio of one will multiply the effective thermal inertia by a factor of four and so on. As a result of these considerations we have plotted a set of average lunation cooling curves for a surface covered with structures of various depth-to-diameter ratios, (Fig. 28a). The craters are spherical for the 60°, 120°, and 180° curves and become cylindrical with hemispherical bottoms for a depth-to-diameter ratio greater than $\frac{1}{2}$. These curves represent a surface completely covered with craters or a relative density of 1.0.

To show the effect of relative crater density on the cooling curves, we have calculated what an observer would see looking at a surface composed of a certain number of hemispherical craters and a certain amount of flat area. The flat area will cool more rapidly than the craters producing a surface that is a composite of two different temperatures. The effective brightness temperature for such a surface can be calculated by using an integral of the Planck law from 10 to 12 microns to express the radiation flux. This is necessary as the observations of Shorthill and Saari have been made in this region of the spectrum. We then use this function (W) to find the amount of flux radiated by each of the two components of the surface and weight these by the respective densities. The effective brightness temperature for the surface is the temperature of a flat surface that would produce an equivalent amount of flux. This can be expressed as follows:

$$W(T_B) = b\,W(\overline{T}_c) + (1 - b)\,W(T_f) \qquad (75)$$

where:

b = relative density of craters

T_B = effective brightness temperature

$\overline{T}_c$ = average crater temperature

T_f = flat area temperature

$W(\ )$ = integral of the Planck law (10 — 20 μ)

Thus the effective brightness temperature is obtained from the flux by inverting the integral of the Planck law, which can be done numerically on the computer. In Fig. 28b cooling curves for the lunar night are shown. These curves were calculated by applying Eq. 75 to the temperatures indicated in Fig. 24. The parameter on the curves is the density of hemispherical craters, which affects cooling in a manner similar to change in depth.

The calculation procedure for brightness temperature of an eclipse is identical; the effects of crater depth and density are shown in Fig. 29. Note that the curves in Figs. 29a and 29b are also quite similar, making it possible to perform a trade-off between depth-to-diameter ratio and relative crater density and obtain the same cooling. Thus a surface covered with a large number of shallow craters will cool in the same manner as a surface covered with a small number of deep craters; this is limited, however, in that heat excavation becomes inefficient in very deep craters. The limiting case of an infinitely deep crater has been calculated by Winter (1965).

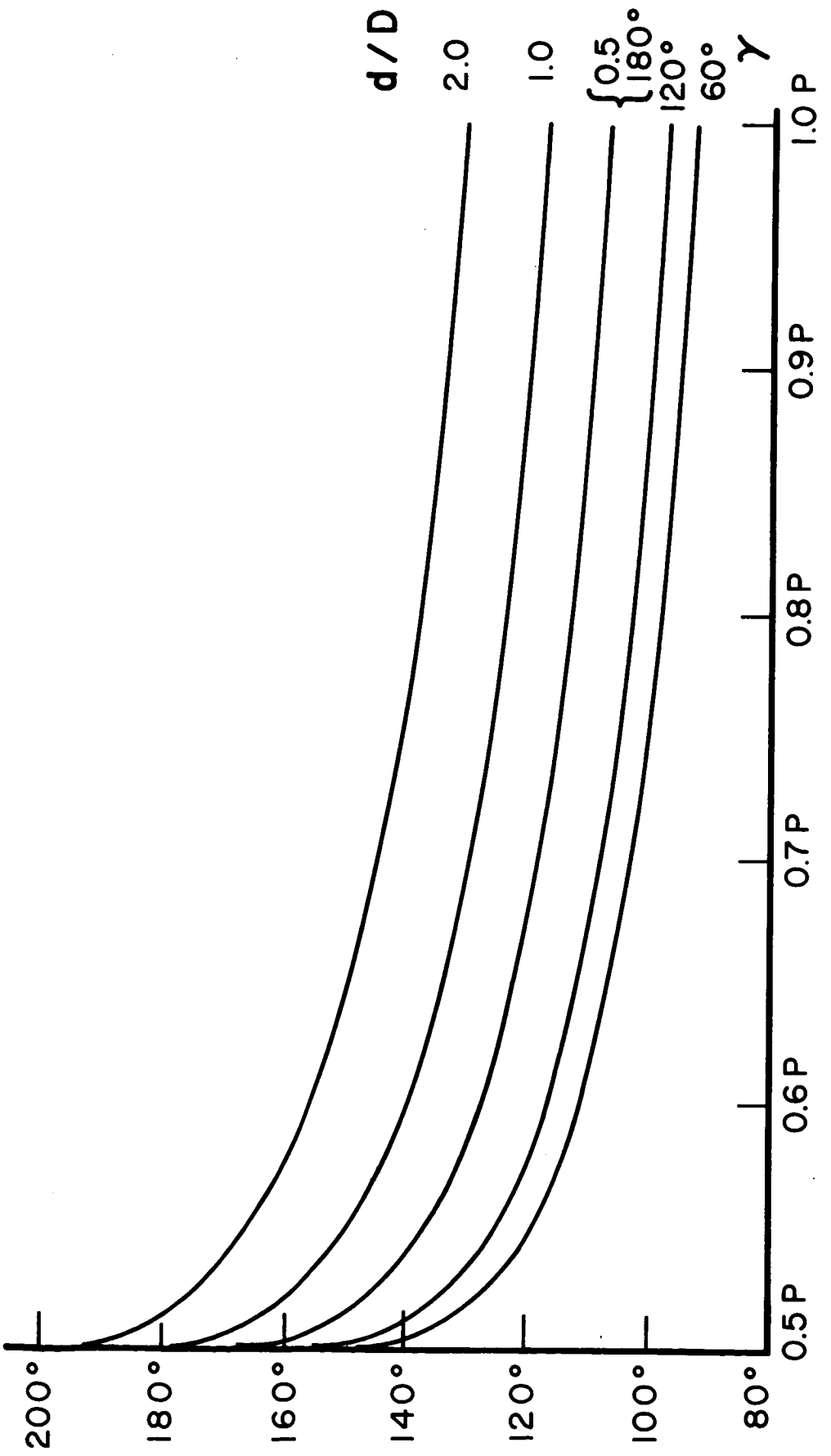

FIGURE 28a

NIGHTTIME COOLING CURVES FOR VARIOUS DEPTH CRATERS

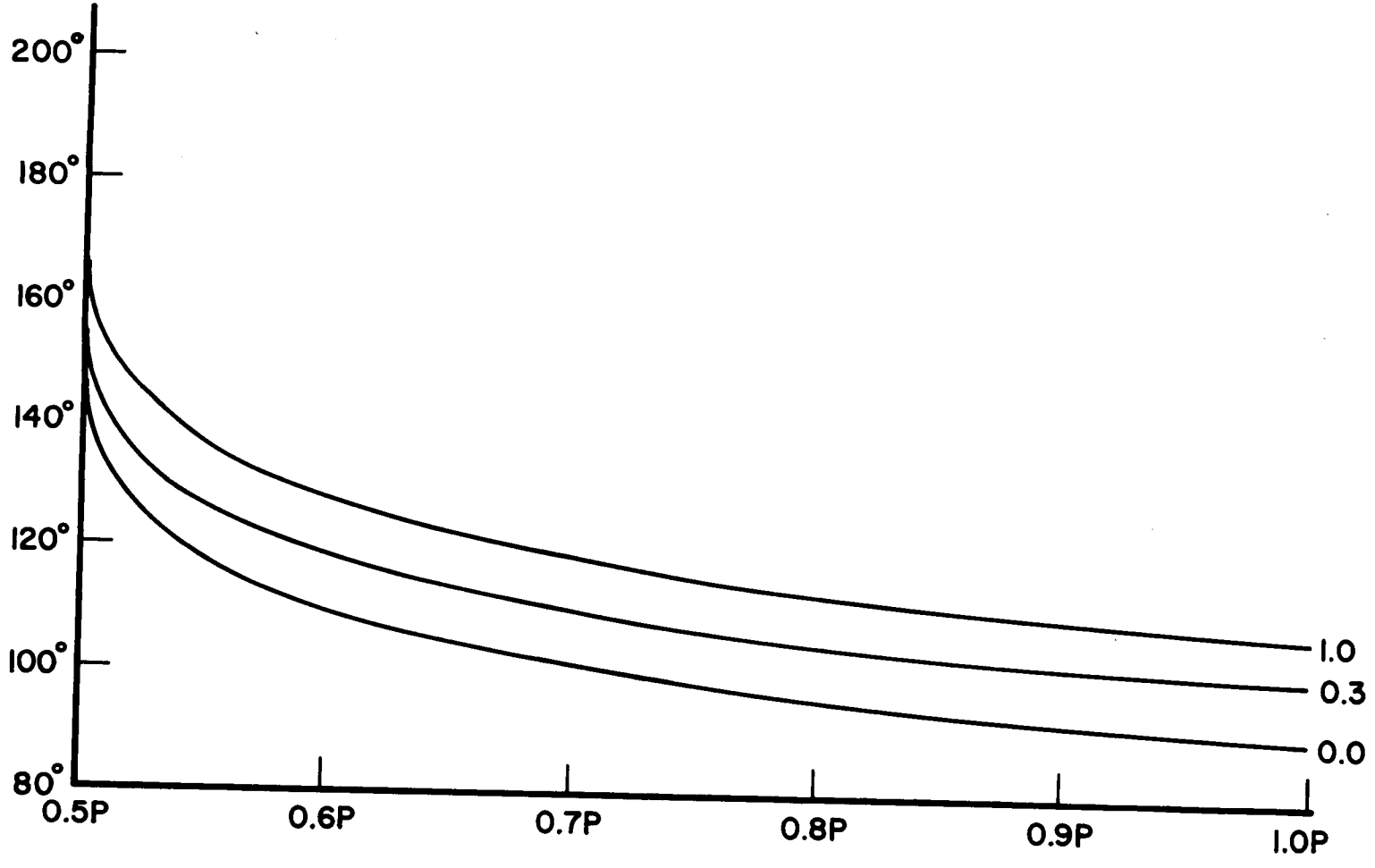

FIGURE 28b

NIGHTTIME COOLING CURVES FOR
VARIOUS DENSITY HEMISPHERICAL CRATERS

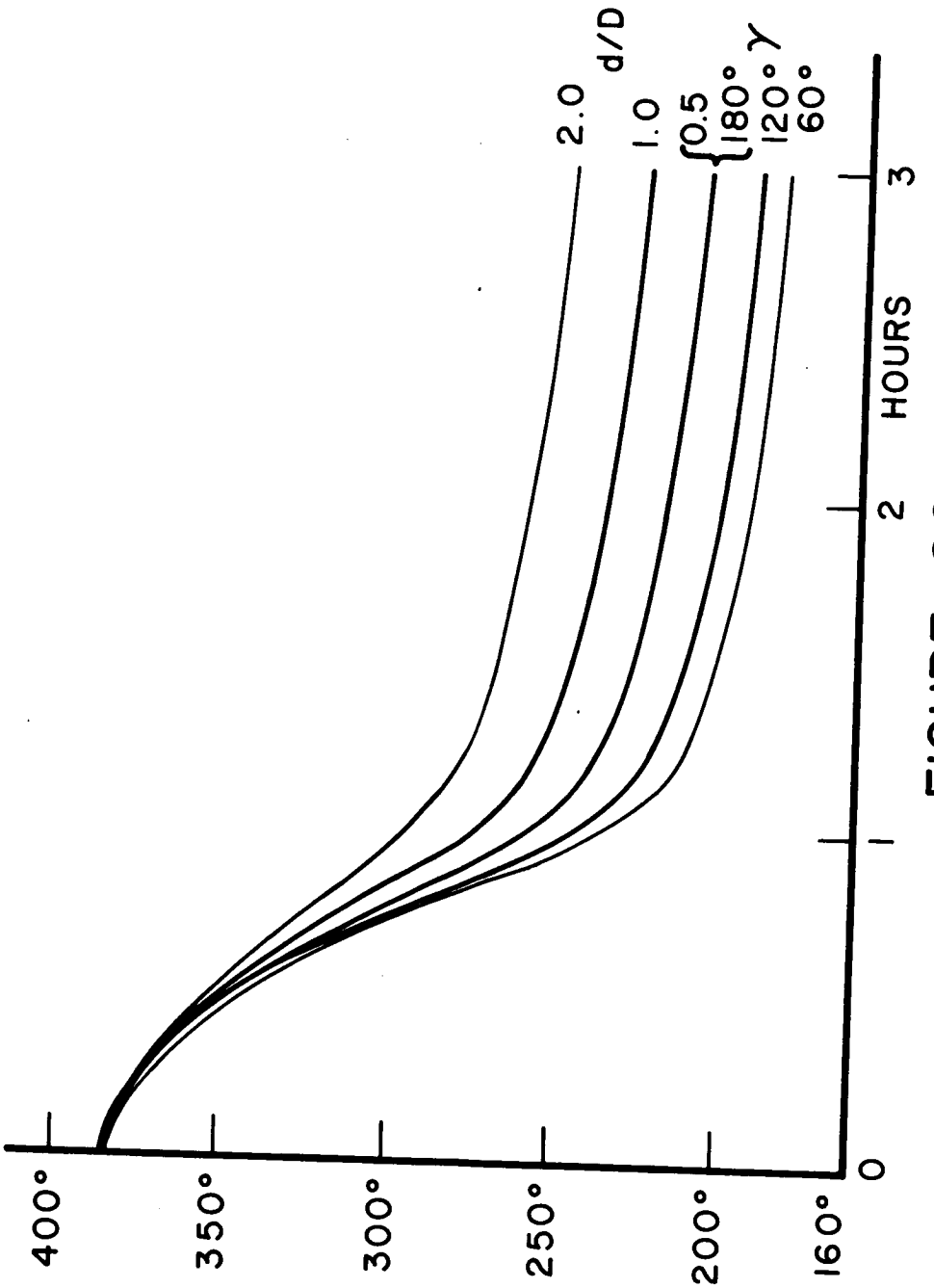

FIGURE 29a

ECLIPSE COOLING CURVES FOR VARIOUS DEPTH CRATERS

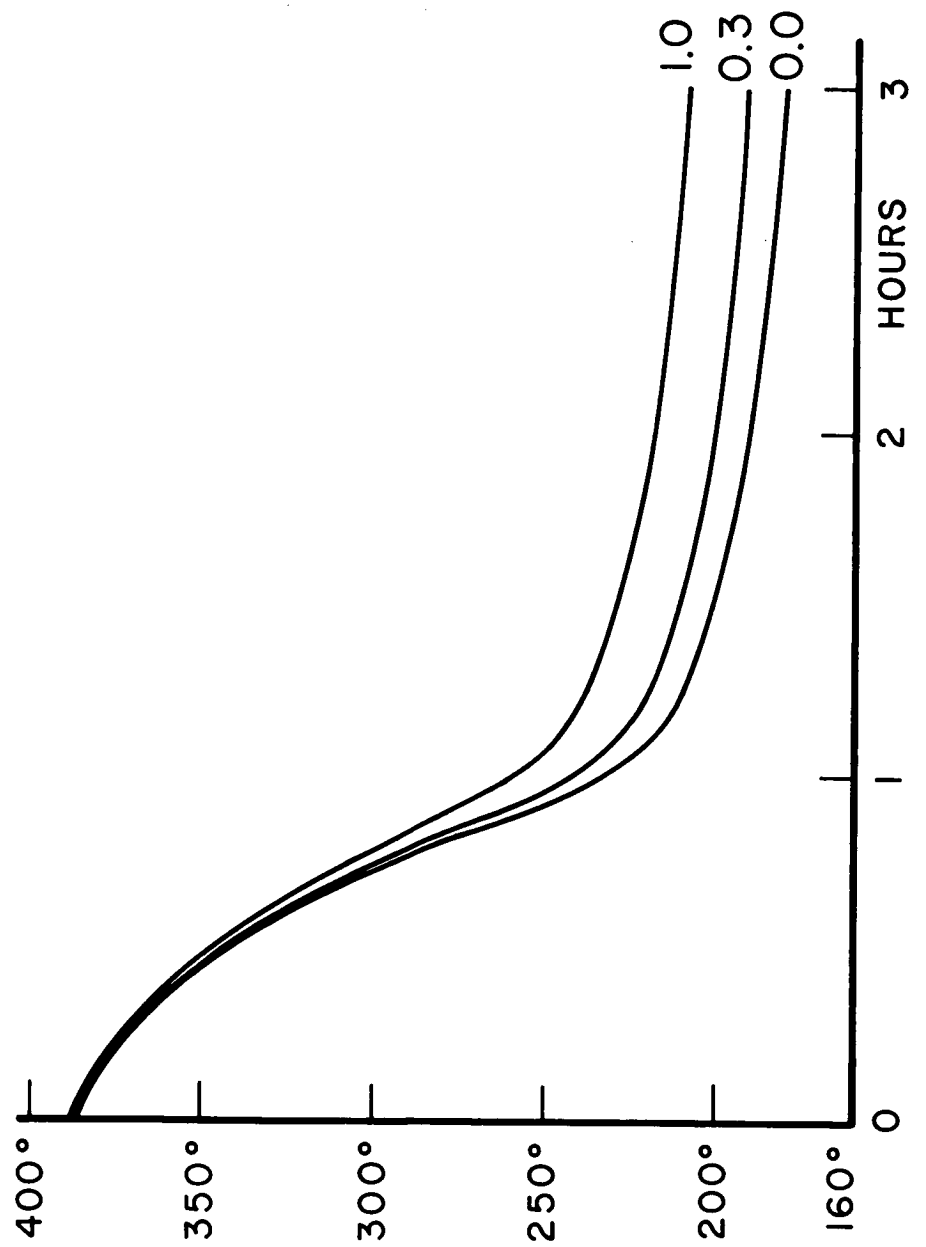

FIGURE 29b

ECLIPSE COOLING CURVES FOR VARIOUS DENSITIES OF HEMISPHERICAL CRATERS

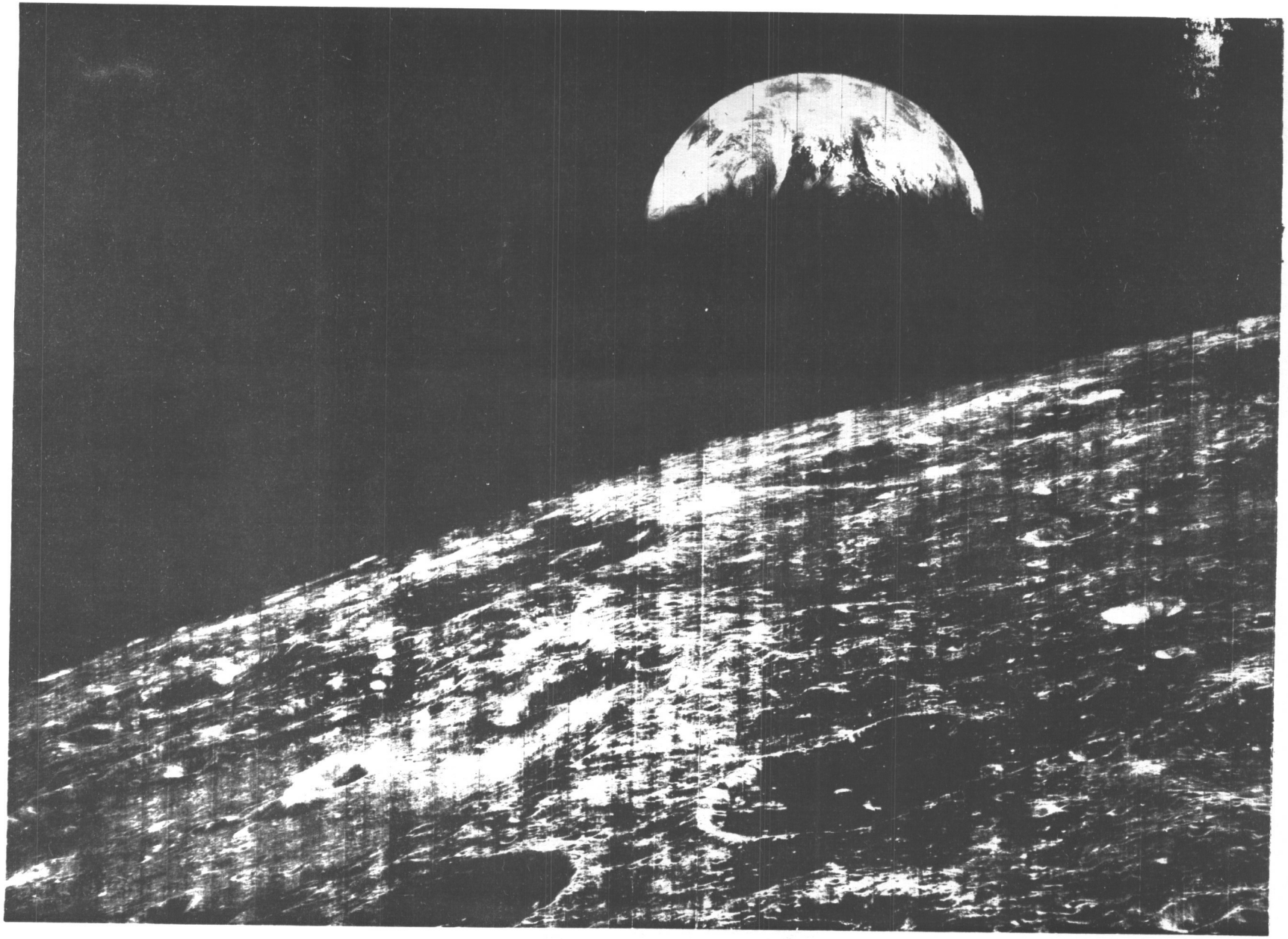

Orbiter I view of lunar landscape (sky and telescope, Dec. 1966)

The thermal anomalies that have been observed are generally in the range of 10° K to 30° K for an eclipse with a high of 50° K reported for Tycho (Saari and Shorthill, 1965). Lunation anomalies tend to be smaller, of the order of 10° K to 20° K, due to the gradual decrease in solar energy and the longer cooling time. The results of our study indicate that such anomalous cooling can be explained by the presence of craters whose shapes are roughly hemispherical. Crater counts have shown that small craters are much more numerous than large ones and also tend to have a larger depth-to-diameter ratio. This fact leads to the possibility that very small craters, of the order of 1 cm, may be responsible for the observed hot spots. Several daytime experiments that would determine more about the nature of these craters are suggested in the Section IV.

IV. EXPERIMENTAL INVESTIGATION

1. Experiments to Detect Small-Scale Lunar Cratering

1.1 The Microwave Anomaly

The large thermal anomalies associated with craters such as Tycho and Copernicus are easily observed in the infrared. If these hot spots are caused by denser material, instead of the cratering suggested here, we will show that one should be able to observe a microwave temperature anomaly. The eclipse is much too short to provide much of a temperature variation. The lunation, however, has a pronounced effect on the microwave temperature.

To calculate the size of the anomaly one would expect, we consider two materials of different densities. The microwave temperature for each is sinusoidal throughout the lunation. Its amplitude is a function of the ratio of microwave skin depth to thermal wavelength

$$\delta = 2\pi L/\lambda$$

$$\lambda = 2\pi\sqrt{2K/\omega} = 2\pi\sqrt{\frac{2k}{\rho c \omega}} \qquad (76)$$

For a sinusoidal boundary condition $\left(T_1 e^{j\omega t}\right)$ the temperature amplitude at a depth z is given by

$$T(z) = T_1 e^{-2\pi z/\lambda} \qquad (77)$$

The microwave temperature that will be observed for a layer at a depth z is

$$T_{\mu} = T(z)\, e^{-z/L} \tag{78}$$

The integration of these two, including a phase effect in Eq. 77, has been done by Piddington and Minnett (1949). The resulting variation in microwave temperature for a homogeneous surface and substrate is:

$$T_{\mu} = T_o + T_1 \frac{1}{\sqrt{1 + 2\delta + 2\delta^2}} \cos(\omega t + \phi)$$

$$\text{Tan}\,\phi = \frac{\delta}{(1 + \delta)} \tag{79}$$

where T_o is the average surface temperature and T_1 is the amplitude of the fundamental component. Higher harmonics are ignored.

Since the microwave losses are proportional to the density of the material (Troitsky 1962), we can assume that the skin depth decreases as:

$$L = \alpha / \rho \tag{80}$$

where α is a material constant. This can be combined with Eq. 76 to give

$$\delta = \frac{2\pi\alpha}{\rho\lambda} = \frac{\alpha c \sqrt{\omega}}{\sqrt{2}\,(k \rho c)^{\frac{1}{2}}}$$

$$\delta \approx (k \rho c)^{-\frac{1}{2}} \tag{81}$$

Thus, due to the fact that α, c, and ω are constants, we have shown that the skin depth-to-wavelength ratio δ is proportional to the reciprocal thermal inertia. Referring to Eq. 79, it can be seen that the microwave temperature depends upon the surface fundamental amplitude T_1 and the reciprocal thermal inertia $(k\rho c)^{-\frac{1}{2}}$. T_1 is also a function of $(k\rho c)^{-\frac{1}{2}}$ and it was evaluated by numerically finding the first fourier coefficient of the surface temperature for various values of thermal inertia. These are given in Table II along with average temperature T_o and the peak sinusoidal variation of the microwave temperature $|T_{\mu 1}|$. One must assume an initial value of δ for the Moon and this will depend on the microwave wavelength. In Table II, we have shown the predicted microwave temperatures for several initial values of δ. δ_i can be determined by selecting the microwave temperature variation (in the row $(k\rho c)^{-\frac{1}{2}} = 1,000$) that agrees with the observed variation (Troitsky 1965 and Sinton 1962). At a wavelength of 1.25 cm, Piddington and Minnett (1949) measured a peak temperature variation of 52° that gives a δ_i of 1.6:

$$|T_{\mu 1}| = \frac{T_1}{\sqrt{1 + 2\delta + 2\delta^2}} = 52^\circ \text{ K} \quad \begin{matrix} T_1 = 157^\circ \text{K} \\ \delta_i = 1.6 \end{matrix} \qquad (82)$$

$$\phi = 45^\circ$$

It is now possible to determine the temperature variation of a microwave anomaly. We consider a region of the surface corresponding to an infrared anomaly to be composed of a denser material giving a $(k\rho c)^{-\frac{1}{2}}$ of 500. The surrounding area is assumed to have a $(k\rho c)^{-\frac{1}{2}}$ of 1,000. In the infrared one will observe an

RTIN $(kpc)^{-\frac{1}{2}}$	Surface Temperature TC °K	Surface Temperature T1 °K	Microwave Temperature INITIAL VALUE OF DELTA 0.1	0.2	0.3	0.4	0.5	0.6	0.7	0.8	0.9	1.0	1.1	1.2	1.3	1.4	1.5	1.6	1.7	1.8	1.9	2.0	2.1	2.2	2.3	2.4	2.5
1000.	210.17	157.23	142	129	117	107	99	92	85	79	74	70	66	62	59	56	53	51	49	47	45	43	41	40	39	37	36
500.	218.20	146.44	139	132	126	120	114	109	105	100	96	92	89	85	82	79	76	74	71	69	67	65	63	61	60	58	56
400.	221.06	142.60	137	131	126	121	117	112	108	104	101	97	94	91	88	86	83	81	78	76	74	72	70	68	66	65	63
300.	224.76	137.32	133	129	125	121	118	115	111	108	105	102	100	97	95	92	90	88	86	84	82	80	78	76	75	73	72
200.	230.32	129.48	126	124	121	119	117	114	112	110	108	106	104	102	100	98	97	95	93	92	90	88	87	85	84	83	81
100.	240.46	114.41	113	112	111	109	108	107	106	105	104	103	102	101	100	99	98	97	96	95	94	94	93	92	91	90	89

RTIN $(kpc)^{-\frac{1}{2}}$	TC °K	T1 °K	INITIAL VALUE OF DELTA 2.6	2.7	2.8	2.9	3.0	3.1	3.2	3.3	3.4	3.5	3.6	3.7	3.8	3.9	4.0	4.1	4.2	4.3	4.4	4.5	4.6	4.7	4.8	4.9	5.0
1000.	210.17	157.23	35	34	33	32	31	30	29	29	28	27	26	26	25	25	24	24	23	23	22	22	21	21	20	20	20
500.	218.20	146.44	55	54	52	51	50	49	47	46	45	44	43	43	42	41	40	39	39	38	37	37	36	35	35	34	34
400.	221.06	142.60	62	60	59	58	56	55	54	53	52	51	50	49	48	47	46	45	45	44	43	42	42	41	40	40	39
300.	224.76	137.32	70	68	67	66	65	64	63	61	60	59	58	57	56	55	54	53	53	52	51	50	49	49	48	47	47
200.	230.32	129.48	80	79	78	76	75	74	73	72	71	70	69	68	67	66	65	64	64	63	62	61	60	60	59	58	57
100.	240.46	114.41	93	88	87	86	85	84	84	83	82	82	81	80	79	79	78	77	77	76	75	75	74	74	73	72	72

TABLE II

Amplitude of microwave temperature variation

eclipse anomaly of 30° K and a lunation anomaly of 15° K. The microwave temperature for this situation is given in Table II, where we have chosen $\delta_i = 1.6$

$$T_\mu = 218 + 74 \cos \omega t \quad \text{anomaly}$$

$$T_\mu = 210 + 52 \cos \omega t \quad \text{surrounding area} \qquad (83)$$

We have plotted the microwave temperature in Fig. 30 to show the variation in the observed temperature of the anomaly (shaded area). The phase lag of approximately 45° is not shown. What one sees is a microwave hot spot for part of the lunation cycle and a cold spot for the remainder of the cycle. The peak temperature anomaly will be + 30° K and — 14° K.

The significance of this result is that an infrared anomaly that is caused by a change in the bulk properties of the surface will have a large variable microwave anomaly associated with it. An anomaly produced by cratering will have a small constant microwave anomaly due only to the shift in average temperature.

Observations of a microwave anomaly in the craters Tycho and Copernicus were attempted at the University of California Hat Creek Observatory. The 85-foot antenna was used at a wavelength of 1.35 cm. The beamwidth was 4', but unfortunately the main lobe contained only 25% of the antenna pattern. The craters are approximately 1' in diameter so that they occupy $\frac{1}{16}$ of the area covered by the main lobe. The additional factor of 4 due to the aperture efficiency gives the increase in antenna temperature as:

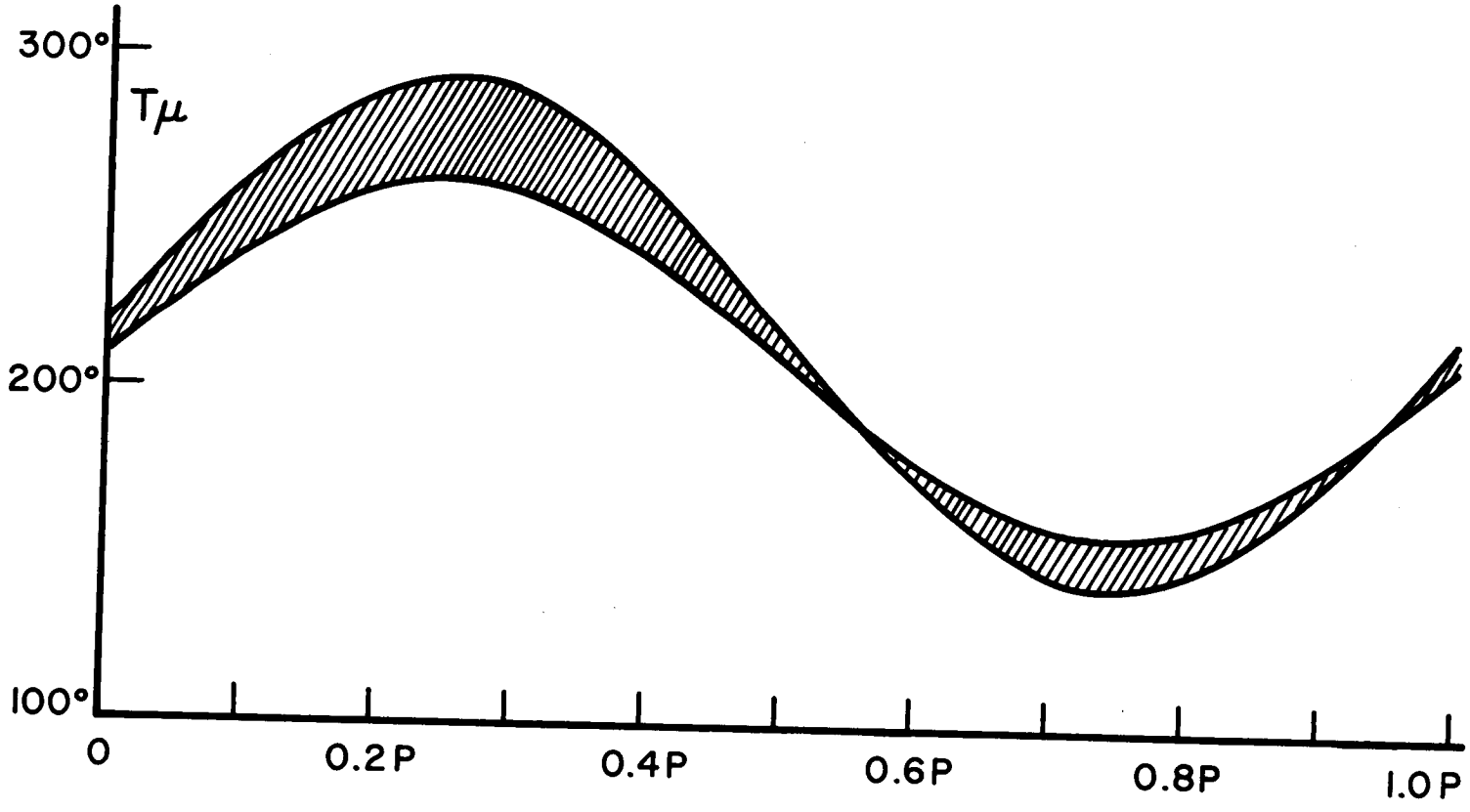

FIGURE 30

MICROWAVE ANOMALY TEMPERATURE

$$\Delta T_A = \frac{\Delta T_\mu}{64} \tag{84}$$

By making successive scans of the crater and then integrating, a resolution of $\Delta T_A = 0.2^\circ$ K was obtained and no anomaly was observed. Thus an upper limit for the anomaly temperature is 12.8° K for our measurements. It is felt that a much better upper limit can be obtained using presently available mm-wave antennas. Since no microwave anomalies have been reported, we are led to conclude that the hard surface model for the thermal anomalies is incorrect.

1.2 Radiation Patterns of Specific Areas on the Lunar Surface

The exact nature of the small-scale cratering on the lunar surface is difficult to determine from presently available data. Several experiments that would help to clarify the characteristics of the anomalous infrared radiation from the Moon will be outlined. This in turn will give a better picture of the type of surface that causes radiation anomalies. It would be of interest to have radiation patterns for various parts of the Moon's surface. This can be illustrated by the study of the sub-earth point shown in Fig. 7c. In this experiment the detector is fixed and the source is rotated. The depth-to-diameter ratio and the relative density of craters in the area investigated will produce a definite type of radiation curve. In particular, the regions that show the anomalous cooling discussed in Section 4 could be investigated in this manner. If they are produced by deep cratering, as has been suggested here, then they will exhibit a peculiar radiation curve. The particular type of radiation curve

that is obtained will be similar to the radiation patterns that we discussed in Section 3. Since the depth-to-diameter ratio of the cratering very strongly affects the radiation patterns (Figs. 13 and 16), it may be possible to determine the depth-to-diameter ratio and the relative density of cratering in the vicinity of a thermal anomaly.

The experiments shown in Figs. 7b and 7c are identical in their geometrical setup and differ only in that the source and detector have been interchanged. There is a reciprocity between the two experiments that can be seen by considering a particular ray that leaves the source, is multiply scattered from the surface, and finally arrives at the detector. If it is assumed that the scattering or reradiation is isotropic on a microscopic scale, this particular ray path is reciprocal. That is, a ray starting from the detector will undergo the same multiple scattering in reverse order and arrive at the source. The attenuation in the path is the same in both directions. Since geometrical optics has been assumed to be valid, the experiment is just measuring an infinite number of these ray paths, each of which is reciprocal. Hence the two experiments should give identical results. The only precaution necessary is to realize that in watching the sub-earth point (Fig. 7c) a constant amount of area is always observed, while in observing the sub-solar point (Fig. 7b) the amount of area observed increases as sec θ_o. Therefore, the radiation pattern for a lambert surface at the sub-earth point is cos θ_o , while at the sub-solar point it is unity in all directions.

In performing an observation of a particular part of the lunar surface, one should take the observed brightness variation throughout half a lunation and multiply this by sec θ_o. The resulting curves then can be compared with those in Figs. 13 and 16 to determine the crater depth-to-diameter ratio. This ratio can be determined primarily from the steepness of the curves, with a reversal in curvature indicating very deep craters (depth/diameter > 1.0).

It would be very useful to have data on the radiation patterns of specific areas, particularly those that have been found to be hot spots during an eclipse (Fig. 20). Such data could be obtained easily since the daytime brightness of the Moon is very high. The photometric behavior of various areas of the surface has been studied already in detail, both experimentally and theoretically (Sitinskaja and Saronov 1952, Hapke 1963). Much can be learned about the thermal anomalies by a similar study in the infrared, which could be carried out for many areas of the Moon. The results of such a survey, when combined with the Pettit and Nicholson data, would provide a much better conception of small-scale lunar cratering.

1.3 The Slope of Radiation in the Infrared Window

The experiments that have been done in the infrared generally have measured the total flux coming from an area of the Moon's surface in the 8 — 14 μ telluric water vapor window. It has been assumed that the area emits as a constant-temperature blackbody. As has been shown here, the small craters contain large temperature variations (Fig. 25a) and therefore do not emit as a blackbody. Such craters have a composite radiation curve, which is non-isothermal. One means of determining the

nature of the Moon's surface is to measure the spectrum, as well as the magnitude of the emission in the water vapor window. Such a measurement could be made most simply by taking the ratio of the flux in the 12 — 14 μ interval to the flux in the 8 — 10 μ interval. This ratio is equivalent to the normalized slope of the lunar emission in the 8 — 14 μ window. A slope measurement would not be difficult to make with presently available infrared filters, and because a ratio is being determined, it should be relatively immune to experimental errors. This type of experiment would be very valuable in determining further the types of small craters and roughness that characterize the lunar surface.

In order to calculate the ratios that one would theoretically expect to obtain in an infrared slope experiment, the Planck law integration, described in Section 4.6, was used. This procedure integrates over constant temperature strips in the crater to obtain the 8 — 10 μ or 12 — 14 μ flux that is radiated in the direction of the observer, which then can be applied to a particular experiment. Two experiments will be considered that were performed by Pettit and Nicholson (Figs. 7a and 7b) and the results of a slope measurement for each will be presented.

To illustrate the data one would expect, we have chosen two extreme cases — a Moon that is a smooth Lambert sphere and one that is covered completely with hemispherical craters. Presumably, the actual Moon is somewhere between these two extremes. In the scan across the full Moon (Fig. 7a) Pettit and Nicholson observed a $(\cos \theta_o)^{\frac{2}{3}}$ variation of brightness instead of a $\cos \theta_o$

variation, which would be expected for a smooth Moon. We have shown that this probably is due to the presence of small-scale cratering and roughness.

The slope of the infrared radiation as one measures across to the limb is shown in Fig. 31. Note that there is very little change in slope from center to limb for a cratered Moon. However, the smooth Moon curve is very steep, producing a large difference in slope at the limb. This experiment, therefore, is very sensitive to the amount of cratering and roughness and should provide a very good indication of the small-scale lunar surface. The two surface models for the radiation patterns shown in Fig. 32 differ less. In this experiment the slope for a smooth Moon is constant for all angles, while the slope for the cratered Moon decreases slightly toward the limb. It will be more difficult, therefore, to distinguish roughness in a slope measurement of the sub-solar point (Fig. 7b). Thus the measurement of infrared slope for the full Moon will give the most significant data on the small-scale cratering. Both this experiment and that suggested in Section 1.2 would add a great deal to our knowledge of the small-scale lunar surface.

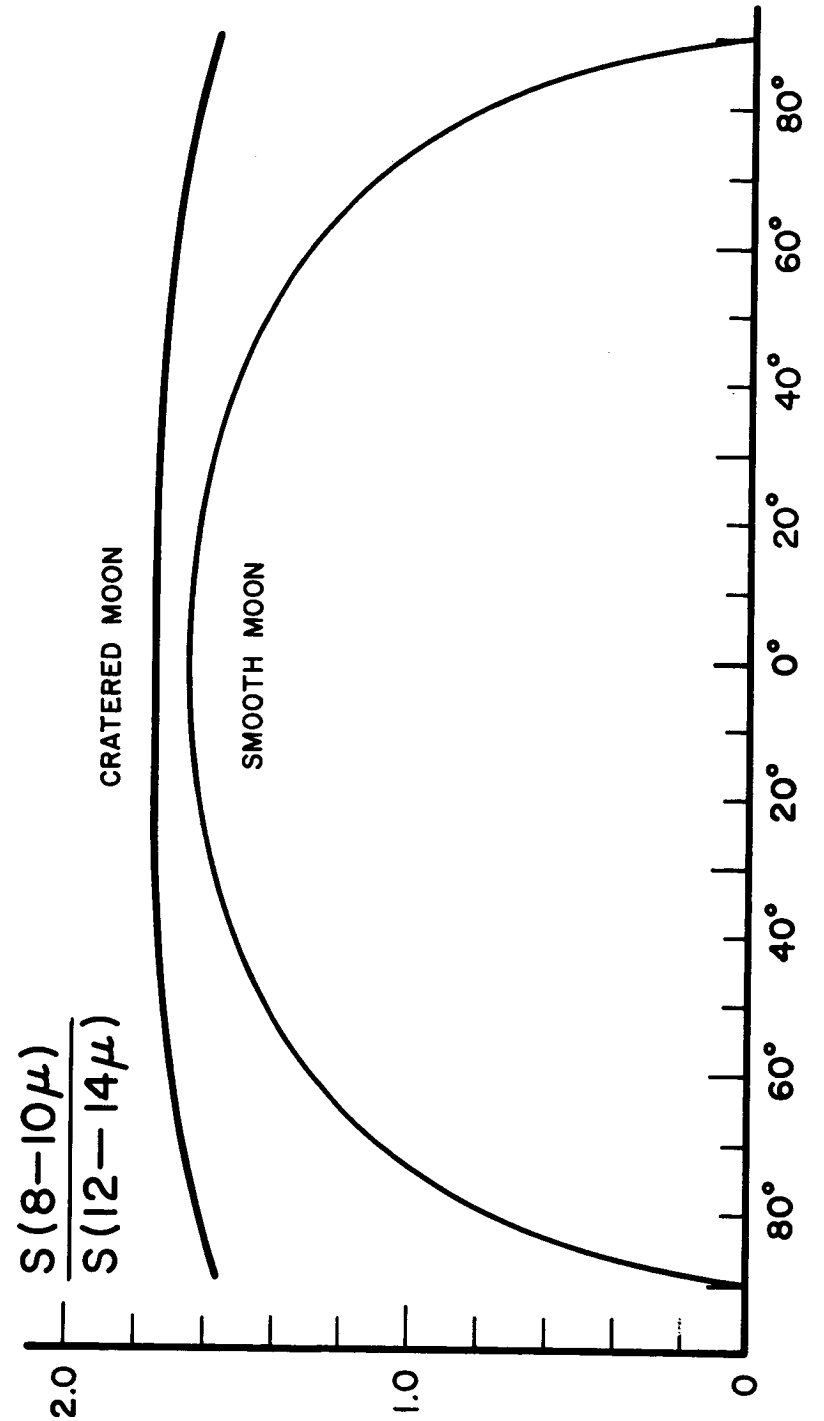

FIGURE 31

INFRARED SLOPE FOR THE FULL MOON

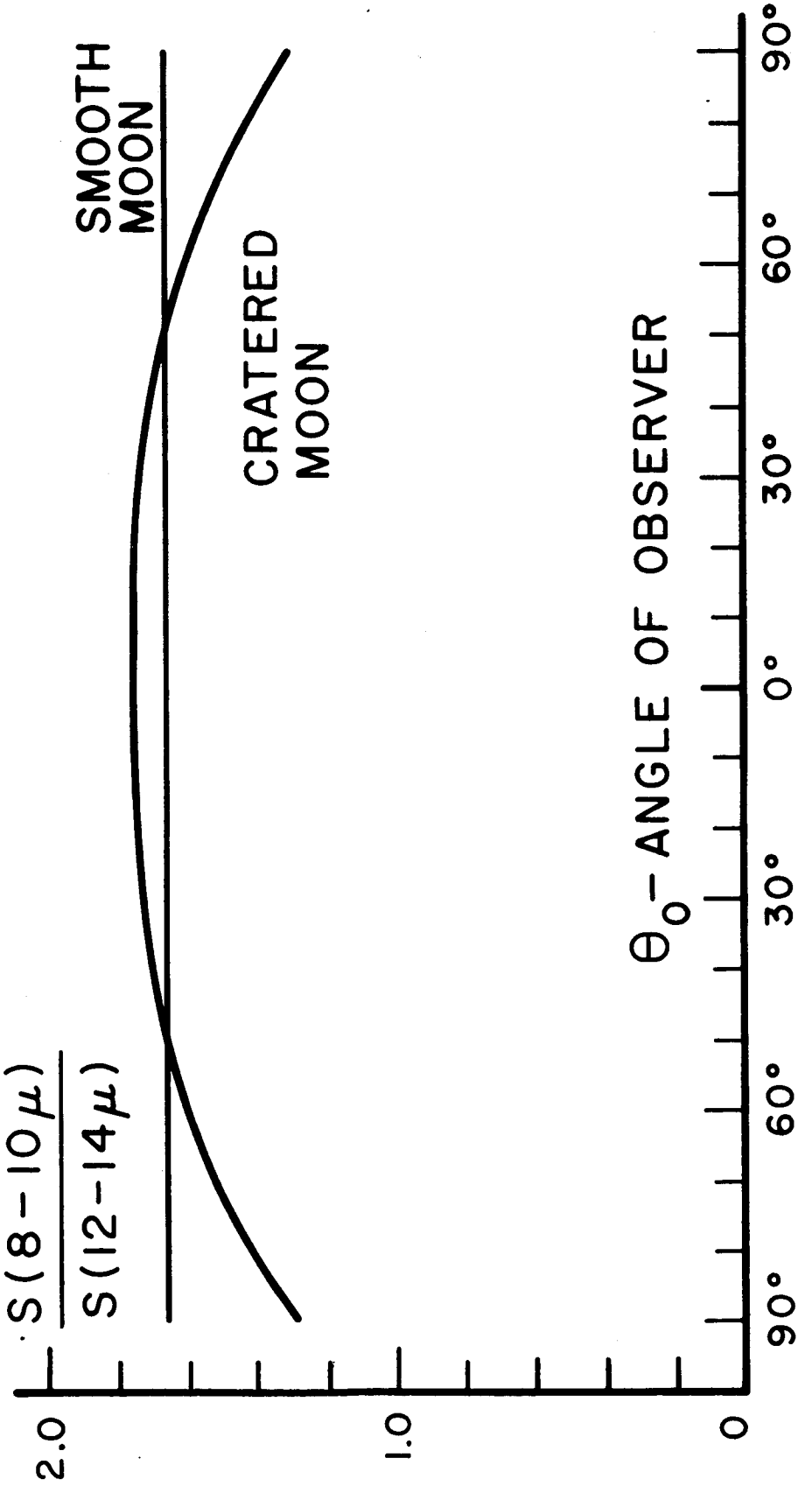

FIGURE 32

INFRARED SLOPE FOR THE SUB SOLAR POINT

V. DISCUSSION

Out of the many interpretations of visual, infrared, and microwave data on the Moon have come a number of conflicting models for the lunar surface. Some of these conflicts will only be settled by a manned landing on the surface. We have attempted to resolve some of the problems by showing the importance of small-scale cratering and roughness in the interpretation of infrared measurements. In addition, several experiments have been suggested that would allow us to describe in greater detail the extent and type of cratering that exist in various regions of the lunar surface. From examining the data of Pettit and Nicholson, we have concluded that at the scale of a few millimeters, 30 % of the Moon's surface is covered with craters of approximately hemispherical shape (depth/diameter $\approx \frac{1}{2}$). These craters, which probably have been produced by micrometeorites, are much deeper (relative to the diameter) than any that have been studied by Baldwin (Fig. 2). It is therefore important that additional infrared measurements be made to find out more information about these millimeter scale craters.

In order to explain the infrared data of Pettit and Nicholson, we have used a model that consists of spherical craters in a flat terrain. This model is similar to some of those that have been proposed to explain the photometric data, except that multiple scattering (or reradiation) has been considered as well as shadowing (Van Diggelen 1960, Bennet 1938). However, the model is quite different from those of other interpretations of the infrared

data. Pettit and Nicholson suggested a surface composed of spheres, but they only calculated the effect of these on the full moon limb darkening. Gear and Bastin (1962) proposed rectangular corrugations, but did not calculate any radiation curves. Their model could be considered to be equivalent to cylinders with a depth-to-diameter ratio of 1.0. As we have shown, the radiation patterns for such a cylindrical model do not correspond to the subsolar point data of Pettit and Nicholson. Winter (1965) proposed infinitely deep cracks, primarily as an explanation for the eclipse thermal anomalies. Again, such a roughness model does not explain the illuminated infrared radiation pattern of the subsolar point.

It is important to realize that practically any roughness model with a suitable adjustment of parameters will give the infrared limb darkening of $(\cos \theta)^{\frac{3}{2}}$ observed by Pettit and Nicholson. The characteristic that can be used to distinguish between the various models for surface roughness is the radiation pattern. In order to determine the correct surface model, this must be compared with the subsolar point observations of Pettit and Nicholson. The radiation pattern is very sensitive to a change in the depth-to-diameter ratio of the roughness (Fig. 16). Hence, it should give a very good indication of the depth-to-diameter or average slope of the small-scale roughness. Due to the change in slope from center to rim, large temperature variations are produced in the illuminated crater. These temperature variations are directly related to the radiation patterns. If the crater is small enough, the temperature variations are reduced by surface conduction, and the radiation pattern becomes isotropic. Hence an anomalous radiation pattern

implies the existence of large temperature variations. The lower limit of size for the crater is obtained by calculating the maximum permissible temperature gradient. The scale of the cratering that produces the radiation patterns can then be obtained directly from this calculation. This follows from the observation that the depth-to-diameter ratio increases in the smaller craters. The resulting scale is of the order of a millimeter. It should be emphasized that the depth-to-diameter ratio for this millimeter scale cratering can be uniquely determined from the radiation patterns. In addition, the density is given by the full moon limb darkening curve. We thus have a fairly complete picture of the millimeter scale roughness.

Data from observations at visible and microwave wavelengths have also been interpreted as being due to surface roughness. Work by Hapke (1963) and others have shown that very complex structures are required to produce the lunar photometric function. Such structures have very deep and intricate passages at the scale of a few microns. At the other end of the spectrum, Evans and Pettengill(1963) and Rea et al. (1964) have found average slopes from radar returns to be about 1:5 for wavelengths of 3.6 cm and 68 cm. Combining these with our interpretation of infrared data, we can construct a table that shows that the Moon's surface appears to have an abrupt increase in roughness as the scale decreases below a few centimeters.

ROUGHNESS SCALE	DEPTH/DIAMETER
10 — 100 cm	1:10 (depth/diameter $\approx$ av. slope/2)
1 mm	1:2
10 — 100 microns	$\sim$ 5:1

Photographs from the Surveyor satellite show a fairly rough surface on a millimeter scale, particularly when illuminated by the setting Sun. However, individual craters are difficult to distinguish and the resolution is at best a millimeter. Hence, we can conclude that our model fits in with most evidence on the surface roughness of the Moon, although the photographic evidence is somewhat vague. Consequently, additional infrared data would be particularly important in further refining our results and in determining the variation in roughness across the lunar surface.

There is some difficulty in constructing a model that is both physically realistic and capable of a mathematical solution. We have tried to present some of the techniques by which a model of the surface characteristics can be obtained from the infrared data. Since the relationship between a particular infrared measurement and the resulting surface model is not completely unique it is important to have data from several different types of experiments. This is particularly true of more elaborate representations of the lunar surface. The model used by Winter (1965) has one parameter (the density, or number of cracks), while our model has two parameters in order to give an

idea of the depth-to-diameter ratio as well as the density of the roughness. We then use the two sets of data obtained by Pettit and Nicholson to determine these parameters. As an alternative set of parameters, we might have chosen the mean and variance of a gaussian distribution of depth-to-diameter ratio for the crater. In either case, one encounters the problem of making a model for those craters that are deeper than a hemisphere. A cylinder model has been discussed. A cone, paraboloid, or ellipsoid model could have been tried, but the mathematics of reradiation would have been difficult. For the shallower craters, a sphere is the best choice from the mathematical standpoint, and it represents a good physical approximation.

A very significant prediction of our study of cratering is the existence of large temperature variations in small craters. Pettit and Nicholson measured the subsolar point and found that the "temperature" that is observed decreases for very large observing angles. We have shown that this can be explained by the presence of hemispherical craters, which cause the infrared emission to be maximum in the direction of illumination. Such anomalous radiation patterns are produced by a temperature distribution that decreases toward the rim. Under normal illumination the distribution is symmetric with the maximum temperature at the center. The temperature variation can sometimes exceed 100° K over a distance smaller than 1 cm. Thus the individual variations cannot be observed from the Earth, where the resolution of an area on the Moon is at best 1 km. However, the variations will have an effect on the observed temperature of an area, as is the case with the subsolar point. It is very important

to realize that these temperature variations are real and that the observed temperature is a rough average for the surface. It is actually an equivalent brightness temperature, which would give the the same observed flux in the 10 — 12 μ window. This brightness temperature always will be somewhat higher than the average temperature. Thus one should be very careful about what is meant by temperature with respect to infrared observations of the Moon.

Shorthill and Saari have observed a large number of thermal anomalies during the lunar eclipse. Very little is known about these areas except that generally they are associated with features that are bright at full moon. Some of the thermal anomalies, such as Tycho, also are radar anomalies. This implies that the area in and around the crater Tycho must be either much rougher or much denser than other parts of the Moon. None of the other suggestions that have been made explain the fact that Tycho is both a radar anomaly and a thermal anomaly. However, there is one difficulty in that the radar brightness contours for Tycho do not match the infrared eclipse contours (Shorthill and Saari 1965). It may be that several of the mechanisms suggested are responsible for producing the thermal anomalies. The anomaly associated with Tycho has been observed to be 50° K warmer than the surrounding area. If the anomaly is caused by roughness, we have shown that the structures needed to produce such a large anomaly would have to have a depth/diameter >1.0, even with a relative crater density of 1.0. This degree of roughness should be very apparent in an infrared study of Tycho under various angles of illumination. As we have indicated, the depth-to-diameter ratio of the roughness is

related directly to the anomalous radiation patterns that the area produces. Until observations are made of the radiation pattern in the region of an anomaly, it is difficult to do more than speculate about the origin of thermal anomalies. Shorthill and Saari have begun such a study by publishing maps of the Moon at a few different phases.

There are several areas of lunar investigation in which it is possible to apply our cratering model. Most of the lunar models used to explain the radar backscattering have been statistical models. It would be interesting to see how well the radar data could be fit with a specific model, such as the one that we used to interpret the infrared data. This would require establishing a cratering model at a scale of 10 — 100 cm, with one or two parameters to be determined. The craters probably would be relatively shallow, and the individual surface elements would be mostly specular in their reflection characteristics, with a small diffuse component. It might be possible to obtain the depth/diameter ratio for such a model. However, one of the difficulties is that the radar geometry is equivalent to the full moon experiment of Pettit and Nicholson in that the source and detector are located at the same angle with respect to the surface. In the infrared case there were a number of models that were capable of predicting the infrared limb darkening. A bistatic radar experiment using an orbiting satellite would therefore be very useful in sorting out the various radar models. Another application is in interpreting the passive microwave observations. It would be interesting to calculate the effect of cratering on the microwave temperature variation. This would mean considering the very inhomogenous

surface temperature distribution that excites the thermal wave, as well as the effect of the roughness on the microwave emission. The lunation variation, as well as the pole darkening, could be studied.

A cratering model can also be used to account for the visual observations. As one goes to very small-scale roughness, the structures become very deep and intricate. Studies of the lunar photometric function have shown that is is probably the result of shadowing of light in a very complex three-dimensional structure. If the surface albedo of the individual reflecting elements is not too low, one would also expect some multiple scattering within the structure. In one possible model for such scattering, one would set up micron scale cylinders that have a large depth-to-diameter ratio such as we have done for studying the infrared radiation. If we make the assumption that the scattering from each element of surface in the cylinder is diffuse (isotropic approximation), the equations giving the infrared brightness in a particular direction are the same equations one would derive for the visual brightness (Eq. 35 and Eq. VI-20). Hence the optical brightness will be given by the radiation patterns we have calculated (Fig. 16), since the same assumption is made about both reradiation and diffuse reflection from a surface element, namely that they obey the Lambert cosine law. Therefore, the curves in Figure 16 can be used to determine approximately the depth-to-diameter ratio of the microscopic roughness. Comparing these curves with typical photometric data show the depth to diameter to be at least 2.0 (for a relative density of 1.0). Experimental studies of laboratory prepared surfaces indicate very deep geometries, so

that the depth is more likely to be 5 or 10 times the diameter. Even deeper structures are responsible for the very sharp back-scattering spike associated with the bright-rayed craters (Oetking 1966).

In making a study of the lunar surface, we have made much use of the early infrared data of Pettit and Nicholson (1930). Their results were obtained prior to 1930 when they made extensive observations of both the illuminated Moon and a lunar eclipse on June 14, 1927. Since that time there have been extensive studies of the dark Moon, both during an eclipse (Saari and Shorthill 1963) and during the lunar night (Murray and Wildey 1964). Except for some observations of Sinton (1962), very little has been done to continue the work of Pettit and Nicholson on the illuminated Moon, even though this would be relatively easy to do using present infrared astronomy equipment. Possibly additional studies have not been done because of a lack of understanding of the importance of these experiments in determining the nature of the small-scale lunar surface. Pettit and Nicholson only looked at two out of an infinite number of arrangements of the Sun, Earth, and Moon. Infrared measurements should be made for a number of different geometric arrangements. There are also difficulties with the fact that the data correspond to the average characteristics of the Moon because each point was taken from a different part of the surface. It would be extremely interesting to compare the amount of small-scale cratering in various parts of the Moon, particularly in the region of thermal anomalies. One experiment has already been suggested that should give some indication of the depth-to-diameter ratio for a

specific area. Many similar experiments can be devised to investigate the radiation patterns and spectrum of emission from the surface, particularly when satellites become available for infrared measurements.

The small-scale roughness of the lunar surface apparently increases very rapidly in the centimeter and millimeter range. We have attempted to give some idea of the nature of this small-scale roughness by interpreting the infrared observations as being the result of micrometeorite craters of millimeter dimensions. These craters contain very large temperature variations when they are illuminated by the Sun. In addition, we have suggested that the thermal anomalies observed by Shorthill and Saari may be caused by very deep craters whose dimensions must be at least a few centimeters. These would in turn explain the very strong radar echo that is received from Tycho, if the crater dimensions are larger than a wavelength. We have proposed several experiments that would give a better picture of the millimeter cratering. It is hoped that these experiments would also resolve the question of the mechanism behind the thermal anomalies. The main problem at present is the lack of data about the Moon. There is a need for experimental observations that would allow us to determine uniquely the characteristics of the small-scale lunar surface.

APPENDIX I — Effects of Albedo

The solar flux illuminating a particular element of area dA is (Fig. 33):

$$\text{incident flux} = f_s \cos\psi \qquad (I\text{-}1)$$

f_s = solar constant

ψ = angle of incidence

a = visible albedo

Of this flux, a fraction (1-a) is absorbed and a fraction "a" is reflected.

$$\begin{aligned} \text{absorbed flux} &= (1-a)\ f_s \cos\psi \\ \text{reflected flux} &= a\ f_s \cos\psi \end{aligned} \qquad (I\text{-}2)$$

Except for a small part that is conducted into the surface, all the flux absorbed is emitted from the surface as infrared radiation. In the infrared we assume the local surface to be an ideal black body having a cosine dependence for the emitted radiation. The visible flux that is reflected is also assumed to have a cosine dependence. Both of these are called the reradiation flux, some of which will be intercepted by another element of area dA′. The reradiation flux incident at dA′ consists of the following two parts (Fig. 33):

$$\begin{aligned} \text{infrared reradiation} &= K(1-a) f_s \cos\psi \cos\phi \qquad K = \text{geometric factor} \\ \text{visible reradiation} &= K a f_s \cos\psi \cos\phi \end{aligned} \qquad (I\text{-}3)$$

The amount of this flux that is absorbed at dA' is determined by our assumption that the infrared albedo is zero and the visible albedo is a:

$$\left.\begin{aligned} \text{infrared absorbed} &= K(1-a) f_s \cos\psi \cos\phi \\ \text{visible absorbed} &= (1-a) Ka f_s \cos\psi \cos\phi \end{aligned}\right\} \text{reradiation absorbed}$$
$$\text{visible reflected} = aKa f_s \cos\psi \cos\phi \qquad \text{(I-4)}$$

Therefore, the reradiation flux absorbed by dA' is:

$$\text{reradiation absorbed} = K(1-a^2) f_s \cos\psi \cos\phi \qquad \text{(I-5)}$$

Because the albedo is approximately 0.1, Eq. I-5 shows that 99% of the reradiation flux is absorbed at a point in the crater. Hence with little error we may assume that all of the reradiation flux is absorbed at dA'. Note that we have not chosen a specific geometry for the crater. The isotropic approximation for the photometric function (Fig. 3) is very good despite the narrow back-scattering. The angular distribution of power is rather wide because the amount of spherical area increases as $\sin\theta$. Hence the power is distributed fairly isotropically.

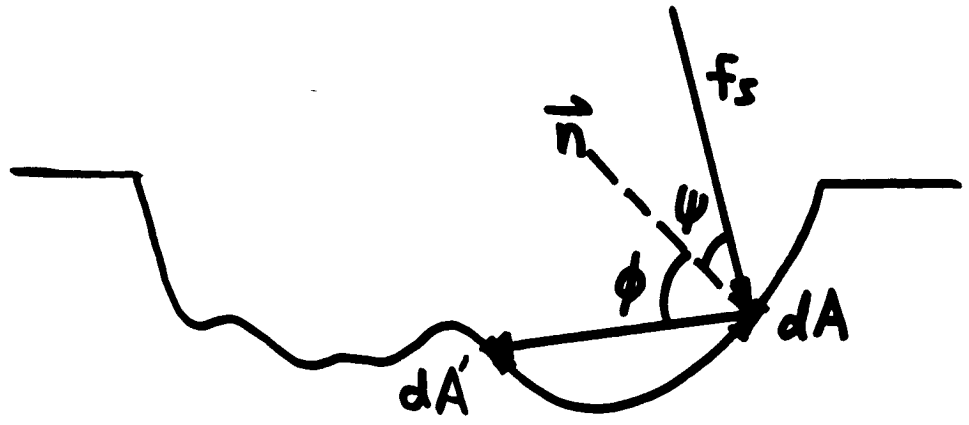

FIG. 33. Effects of albedo

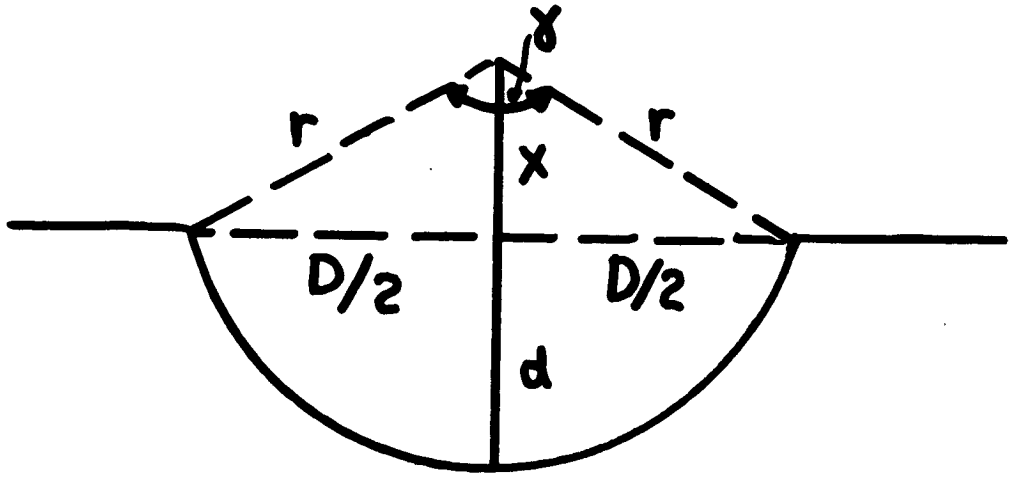

FIG. 34. Geometry of a spherical crater

APPENDIX II — Geometrical Relations for a Spherical Crater

For the spherical crater shown in Figure 34, the following relationships can be stated:

$$x = r \cos \gamma/2$$
$$D/2 = r \sin \gamma/2$$
$$x + d = r$$

where:

- D = diameter of crater
- d = depth of crater
- r = radius of sphere defining crater
- γ = crater angle

(II-1)

From these we can obtain the depth to diameter ratio as:

$$\frac{d}{D} = \frac{1 - \cos \gamma/2}{2 \sin \gamma/2} \tag{II-2}$$

The area of the crater surface can be obtained from integrating a spherical element of area:

$$A_c = \int dA = \int_0^{\gamma/2} \int_0^{2\pi} r^2 \sin\theta \, d\phi \, d\theta$$

$$A_c = 2\pi r^2 (1 - \cos \gamma/2) \tag{II-3}$$

The aperture area is:

$$A_a = \frac{\pi D^2}{4} = \pi r^2 \sin^2 \gamma/2 \tag{II-4}$$

The geometrical constant in Section III-2.2 is

$$C = \frac{A_c}{4\pi r^2} = \tfrac{1}{2}(1 - \cos \gamma/2) \qquad \text{(II-5)}$$

The ratio of crater aperture to surface area is:

$$\frac{A_a}{A_c} = \frac{\pi r^2 \sin^2 \gamma/2}{2\pi r^2 (1 - \cos \gamma/2)} = \frac{1 - \cos^2 \gamma/2}{2(1 - \cos \gamma/2)} = \frac{1 + \cos \gamma/2}{2} \qquad \text{(II-6)}$$

Note that this is just:

$$(1 - C) = 1 - \tfrac{1}{2}(1 - \cos \gamma/2) = \tfrac{1}{2}(1 + \cos \gamma/2) \qquad \text{(II-7)}$$

Therefore, we have:

$$\frac{A_a}{A_c} = 1 - C \qquad \text{(II-8)}$$

$$\frac{A_c}{4\pi r^2} = C \qquad \text{(II-9)}$$

In addition:

$$\frac{A_a}{4\pi r^2} = \frac{A_a}{A_c}\,\frac{A_c}{4\pi r^2} = C(1 - C) \qquad \text{(II-10)}$$

APPENDIX III — Shadow Boundary

The angles that determine the shadowing for the cross section of the crater we have chosen are shown in Fig. 8b. The angle θ_o is taken to be negative as the sun rises from the left and positive as it sets to the right. The angles at which the sun rises and sets for the element of area dA are θ_a and θ_b. The position of dA is given by the angle α, which is positive to the right of the center of the crater. The apex angle is the angle between the normal to dA and the normal to the crater rim (① or ②). We can now obtain the shadowing angles from the triangles in Fig. 8b.

θ_a:

$$\text{apex angle} = \gamma/2 + \alpha \qquad \text{(III-1)}$$

For any triangle the sum of the angles is 180°; hence:

$$\gamma/2 + \alpha + 2\phi = 180^\circ \qquad \text{(III-2)}$$

Note that θ_a is negative so that the sum of the angles about ① is

$$(-\theta_a) + \gamma/2 + \phi = 180^\circ \qquad \text{(III-3)}$$

From Eqs. III-2 and III-3 we have the shadowing angle θ_a as:

$$\theta_a = -90^\circ + \gamma/4 - \alpha/2 \qquad \text{(III-4)}$$

The derivation of θ_b proceeds identically, hence:

$$\theta_b = 90^\circ - \gamma/4 - \alpha/2 \qquad \text{(III-5)}$$

Hence the direct solar flux term is zero for:

$$\theta_o < -90^\circ + \gamma/4 - \alpha/2$$

or

$$\theta_o > 90^\circ - \gamma/4 - \alpha/2 \qquad \text{(III-6)}$$

APPENDIX IV — $\int \cos\psi \cos\psi' \, dA$

In order to perform this integral over the unshadowed region as shown in Figs. 11 and 12, we must express the integral in terms of the spherical coordinates of the element of area dA. From spherical trigonometry, the angles ψ and ψ' (Fig. 11a) can be expressed as:

$$\cos\psi = \cos\theta \tag{IV-1}$$

$$\cos\psi' = \cos\theta_o \cos\theta + \sin\theta_o \sin\theta \cos(\phi - \phi_o)$$

After rotating the crater so that the observer is on the z-axis (in Fig. 11b note that ϕ_o has been rotated by 180°), we have:

$$\cos\psi' = \cos\theta_o \cos\theta - \sin\theta_o \sin\theta \cos(\phi - \phi_o) \tag{IV-2}$$

$$\cos\psi' = \cos\theta$$

Substituting Eq. IV-2 into the integral, we find:

$$\int \cos\psi \cos\psi' dA = \int \left[\cos\theta_o \cos^2\theta - \sin\theta_o \sin\theta \cos\theta \cos(\phi - \phi_o)\right] \tag{IV-3}$$

The spherical element of area is

$$dA = r^2 \sin\theta \, d\theta \, d\phi \tag{IV-4}$$

Since θ_o is not a function of position in the crater, we can remove those factors that contain θ_o. We can also take $\phi_o = 0$ for the x-axis chosen in Fig. 12.

$$\int \cos\psi \cos\psi' \, dA = r^2 \cos\theta_o \iint \cos^2\theta \sin\theta \, d\theta \, d\phi$$

$$- r^2 \sin\theta_o \int\int \sin^2\theta \cos\theta \cos\phi \, d\theta \, d\phi \qquad \text{(IV-5)}$$

This can now be directly integrated over θ for the shadow-rim boundary limits derived in Appendix V.

$$\int \cos\psi \cos\psi' \, dA = \frac{r^2 \cos\theta_o}{3} \int_o^{2\pi} (\cos^3\theta_1 - \cos^3\theta_2) \, d\phi$$

$$- \frac{r^2 \sin\theta_o}{3} \int_o^{2\pi} (\sin^3\theta_2 - \sin^3\theta_1) \cos\phi \, d\phi \qquad \text{(IV-6)}$$

The integrals themselves in Eq. IV-6 have been tabulated in Table I for various crater angles and solar incidence angles.

APPENDIX V — Shadow-Rim Integration Limits

The shadow rim contour is generated by the intersection of an elliptical cylinder with the sphere defining the crater (Fig. 12). The base of the elliptical cylinder is the projection of the crater rim on the X - Y plane. The rim is tilted at an angle θ_o. The intersection of the cylinder with the sphere defines two circles that together make up the shadow-rim contour.

To evaluate the integration limits we must find the spherical coordinates of the contour. This general shadow-rim boundary for various depth craters can be found by solving a quadratic equation in $\sin \theta_s$. This can be derived by considering a crater whose angle is γ and whose tilt is θ_o (Fig. 11). In the case of craters less than hemispherical, the contour of θ_s has symmetry about the X - Z plane only and the elliptical cylinder (Fig. 12) moves off center to the left as the observer angle θ_o increases.

The equation of the elliptical base of the cylinder, and therefore of the cylinder, is:

$$\frac{(x + c)^2}{a^2} + \frac{y^2}{b^2} = r^2 \qquad \text{(V-1)}$$

$a = \cos \theta_o \sin \gamma/2$

$b = \sin \gamma/2$

$c = r \sin \theta_o \cos \gamma/2$

$r =$ radius of sphere

In cylindrical coordinates (ρ, ϕ, z):

$$\frac{(\rho \cos \phi + c)^2}{a^2} + \frac{\rho^2 \sin^2 \phi}{b^2} = r^2 \qquad \text{(V-2)}$$

In spherical coordinates (r, ϕ, θ):

$$\frac{(r \sin\theta \cos\phi + r \sin\theta_o \cos\gamma/2)^2}{\cos^2\theta_o \sin^2\gamma/2} + \frac{r^2 \sin^2\theta \sin^2\phi}{\sin^2\gamma/2} = r^2 \qquad \text{(V-3)}$$

The intersection of this cylinder with the sphere is obtained automatically since r is the radius of the sphere. Multiplying Eq. V-3 by $\frac{\left(\cos^2\theta_o \sin^2\gamma/2\right)}{r^2}$, we obtain

$$(\sin\theta \cos\phi + \sin\theta_o \cos\gamma/2)^2 + \sin^2\theta \sin^2\phi \cos^2\theta_o = \cos^2\theta_o \sin^2\gamma/2 \qquad \text{(V-4)}$$

Collecting like powers of $\sin\theta$, we have

$$\sin^2\theta(\cos^2\phi + \sin^2\phi\cos^2\theta_o) + 2\sin\theta(\cos\phi \sin\theta_o \cos\gamma/2) + \sin^2\theta_o \cos^2\gamma/2 - \cos^2\theta_o \sin^2\gamma/2 = 0 \qquad \text{(V-5)}$$

The coefficients of this quadratic equation in $\sin\theta$ are:

$$A = \cos^2\phi + \sin^2\phi\cos^2\theta_o = 1 - \sin^2\phi\sin^2\theta_o = \cos^2\theta_o + \cos^2\phi\sin^2\theta_o$$

$$B = \cos\phi \sin\theta_o \cos\gamma/2 \qquad \text{(V-6)}$$

$$C = \sin^2\theta_o \cos^2\gamma/2 - \cos^2\theta_o \sin^2\gamma/2 = \cos^2\gamma/2 - \cos^2\theta_o$$

In terms of these, the roots for $\sin\theta$ are:

$$\sin\theta_s = \frac{\left(-B \pm \sqrt{B^2 - AC}\right)}{A} \qquad \text{(V-7)}$$

These are the points on the contour of θ_s and they are evaluated numerically. The appearance of two roots in Eq. V-7 occurs when the elliptical cylinder does not contain the origin, i.e. $c > ar$ in Eq. V-1. Each value of ϕ then gives two values of θ_s, which are then the upper and lower limits of the integral (θ_2 and θ_1) in Eq. 32. When there is only one root to Eq. V-7, the lower limit of the integral (θ_1) is zero.

APPENDIX VI — The Integral Equation for a Cylindrical Crater

To make the problem easier to solve we have assumed that the temperature across the bottom of the cylindrical crater is a constant.

$$\sigma T_b^4 = f_o \text{ crater bottom} \qquad \text{(VI-1)}$$

Essentially we have ignored the effects of reradiation on the temperature of the bottom. These might provide some distribution of temperature across the bottom, but this would have a small effect on the resulting radiation patterns. For very deep cylinders the bottom is only visible when the surface is observed normally. Any elevation in temperature of the entire bottom due to reradiation effects will simply multiply the radiation patterns by a constant factor. This merely changes the normalization.

With the sun at zenith, the side walls of the crater receive no direct solar flux. The element of area dA will be heated by reradiation flux from the bottom and from other parts of the wall (Fig. 35). The contribution from the bottom is just the integral over the solid angle subtended by the area of the bottom (Ω). This can be seen by considering the area dA to be surrounded by a sphere of radius z. Reradiation flux from the bottom can be considered to be coming from that part of the sphere contained in the solid angle Ω. The amount of reradiation at dA will be the same whether the bottom or part of the sphere is at a temperature T_b.

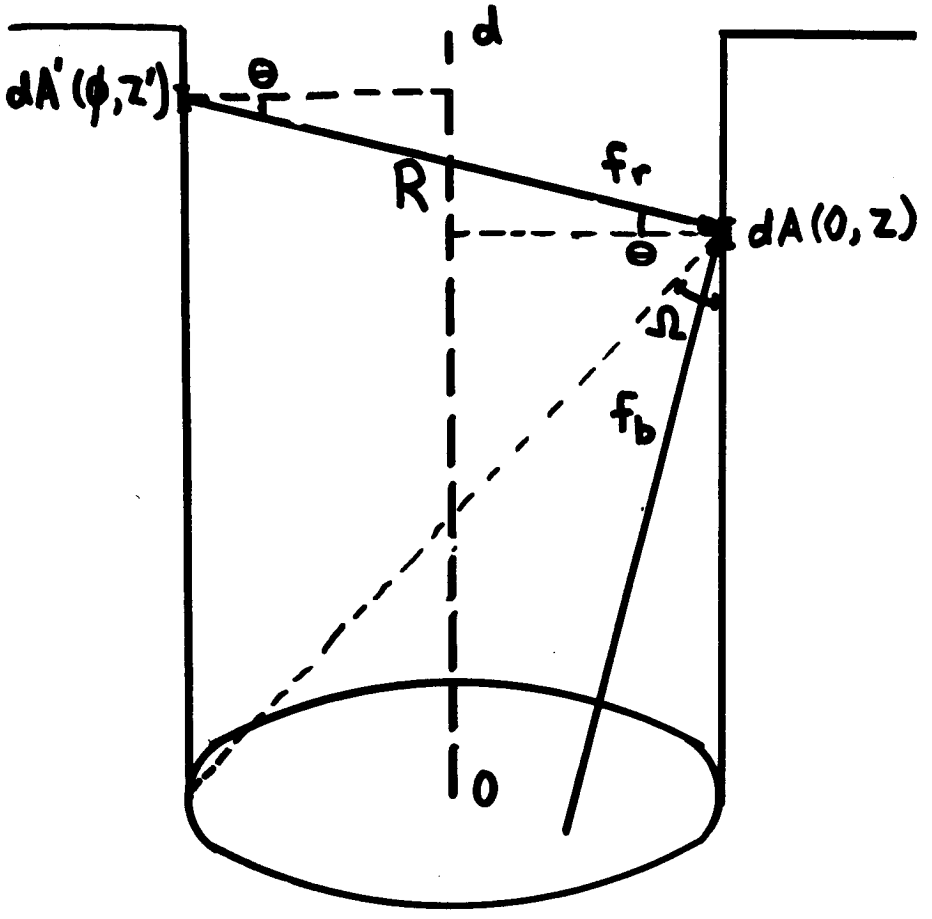

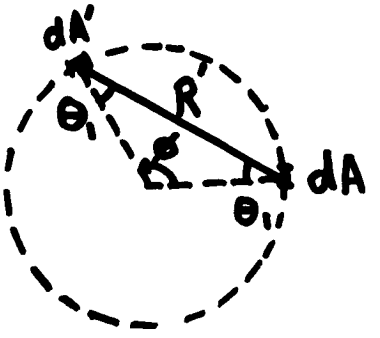

Cross-section of cylinder at dA

FIG. 35. Cylindrical crater

Hence, the reradiation flux at dA from the bottom is equivalent to the element of area being partially surrounded by a black body at a temperature T_b. The flux from this black body at dA is:

$$f_b = \int_\Omega \frac{1}{\pi} \sigma T_b^4 \cos\theta \, d\Omega = \frac{f_o}{\pi} \int_{-\phi_1}^{\phi_1} \int_{\theta_1}^{\theta_2} \cos\theta \sin\theta \, d\theta \, d\phi \qquad \text{(VI-2)}$$

The spherical coordinates of the circle defining the bottom (θ_1 and θ_2) as seen from dA can be obtained by writing the cartesian coordinates for the circle (Fig. 35).

$$z = \text{constant}$$
$$(x-1)^2 + y^2 = 1 \qquad \text{(VI-3)}$$

which is in spherical coordinates (note θ is wrt X-axis and ϕ wrt Z-axis).

$$(r\cos\theta - 1)^2 + (r\sin\theta\sin\phi)^2 = 1$$
$$r\sin\theta\cos\phi = z \qquad \text{(VI-4)}$$

Combining Eqs. 4, we get the spherical coordinates as:

$$\left(\frac{z\cot\theta}{\cos\phi} - 1\right)^2 + (z\tan\phi)^2 = 1$$
$$\cot\theta = \frac{\cos\phi}{z}\left(1 \pm (1 - z^2\tan^2\phi)^{\frac{1}{2}}\right)$$
$$\cot\theta_{1,2} = \frac{1}{z}\left(\cos\phi \mp (\cos^2\phi - z^2\sin^2\phi)^{\frac{1}{2}}\right) \qquad \text{(VI-5)}$$

The integral over the bottom is then:

$$f_b = \frac{f_o}{2\pi} \int_o^{\phi_1} (\cos 2\theta_2 - \cos 2\theta_1)\, d\phi \qquad \text{(VI-6)}$$

The upper limit of the ϕ integral is just the point on the circle (X = 1, Y = 1), which is:

$$\cot \phi_1 = z \qquad \text{(VI-7)}$$

Eqs. VI-5 through -7 are then used to evaluate the reradiation flux from the bottom of the crater at a distance z from the bottom.

The reradiation flux from other parts of the wall of the crater is obtained by an integral similar to the one for the spherical crater (Eq. 9, text). Taking the element of area dA as having cylindrical coordinates (0, z) and dA′ as (ϕ, z′), we first obtain the distance R (Fig. 35). The projection of R on a plane passing through dA (parallel to the bottom) is:

$$R' = 2 \sin \frac{\phi}{2} \qquad \text{(VI-8)}$$

R′ is related to R by

$$R^2 = R'^2 + (z' - z)^2 = 4 \sin^2 \frac{\phi}{2} + (z' - z)^2 \qquad \text{(VI-9)}$$

Note that the two angles (θ) of the surface normals with respect to R are equal as in the case of the spherical crater. Taking the angle of R′ with respect to the surface normals as θ_1 and the angle of R with

respect to R' as θ_2, we have

$$\cos\theta_1 = \sin\frac{\phi}{2}$$

$$\cos\theta_2 = R'/R \qquad \text{(VI-10)}$$

From spherical trigonometry:

$$\cos\theta = \cos\theta_1 \cos\theta_2 = \frac{2\sin^2\frac{\phi}{2}}{R} \qquad \text{(VI-11)}$$

We can now calculate the amount of reradiation flux at dA. The angle subtended by dA is:

$$d\Omega' = \frac{dA\cos\theta}{R^2} \qquad \text{(VI-12)}$$

The brightness of dA' is

$$B = \frac{\sigma T^4}{\pi} \qquad \text{(VI-13)}$$

The reradiation flux at dA is then (Eq. 6 text)

$$\Delta f_r = B\cos\theta\,\frac{d\Omega'\,dA'}{dA} = \frac{\sigma T^4}{\pi}\cos\theta\,\frac{dA\cos\theta\,dA'}{R^2\,dA}$$

$$f_r = \int \frac{\sigma T^4}{\pi}\,\frac{\cos^2\theta}{R^2}\,dA' \qquad \text{(VI-14)}$$

Substituting Eq. VI-9 for R and Eq. VI-11 for cos θ, we have the reradiation from the crater walls as:

$$f_r = \int_0^d \int_0^{2\pi} \frac{\sigma T^4(z')}{\pi} \left[\frac{2 \sin^2 \phi/2}{(z - z')^2 + 4 \sin^2 \phi/2}\right]^2 d\phi \, dz' \qquad \text{(VI-15)}$$

The temperature of dA is determined by the flux balance:

$$\sigma T^4 (z) = f_b + f_r = f_b(z) + \int_0^d K(z, z') \sigma T^4 (z') \, dz' \qquad \text{(VI-16)}$$

This is the integral equation for the temperature on the walls where the kernel is:

$$K(z, z') = \int_0^{2\pi} \frac{1}{\pi} \left[\frac{2 \sin^2 \phi/2}{(z - z')^2 + 4 \sin^2 \phi/2}\right]^2 d\phi \qquad \text{(VI-17)}$$

Thus after numerically calculating the reradiation flux from the bottom (Eqs. VI-5 through -7) we can obtain the wall temperatures by numerically solving the integral equation (Eqs. VI-16 and -17).

To obtain the radiation patterns we must integrate over the visible part of the cylinder the brightness in the direction of the observer.

$$\overline{B} = \frac{1}{\pi \cos \theta_0} \int B \cos \psi' \, dA \qquad \text{(IV-18)}$$

For a cylinder the angle of the observer with respect to the local surface normal (ψ') is just

$$\cos \psi' = \sin \theta_o \cos \phi \qquad \text{(VI-19)}$$

where ϕ is a cylindrical coordinate for the element of area. Since T is only a function of the coordinate z, we have:

$$\overline{B} = \left(\frac{2 \tan \theta_o}{\pi^2} \int_{z_1}^{d} \sigma T^4 (z) \int_{o}^{\phi_1} \cos \phi \, d\phi \, dz \right) \qquad \text{(VI-20)}$$

The two integration limits are functions of the angle of the observer and are:

$$\cos \phi_1 = \frac{d - z}{2 \cot \theta_o}$$

$$z_1 = d - 2 \cot\theta_o \cot \theta_o < d/2 \qquad \text{(VI-21)}$$

$$z_1 = 0 \qquad \cot \theta_o > d/2$$

These can be used in Eq. VI-20 to give the brightness of the walls. In addition when $\cot \theta_o > d/2$, some of the bottom of the cylinder will be visible. The amount of this area is (Eq. VIII-1):

$$A_b = (\theta_1 - \sin \theta_1)$$

where: $\qquad \text{(VI-22)}$

$$\cos \frac{\theta_1}{2} = \frac{d \tan \theta_o}{2}$$

The radiation pattern is then the sum of Eqs. VI-22 and VI-20 with the appropriate normalization:

$$RP = \frac{2 \tan \theta_o}{f_o \pi} \int_{z_1}^{d} \sigma T^4 (z) \int_{o}^{\phi_1} \cos \phi \; d\phi \, dz + \frac{1}{\pi} (\theta_1 - \sin \theta_1) \qquad \text{(VI-23)}$$

The integrals were evaluated numerically and the results are plotted in Fig. 16.

APPENDIX VII — $\overline{T^4} = (\overline{T})^4$

While the crater is illuminated the amount of conducted flux is negligible. Therefore, the approximation $\overline{T^4} = (\overline{T})^4$ is only necessary for calculating the eclipse or nighttime behavior of the crater. The relevant boundary condition for the average cooling is obtained from Eqs. 22d and 22f.

$$\sigma \overline{T^4} = \frac{A_c}{A_a} \quad k \quad \frac{\overline{dT}}{dz} \tag{VII-1}$$

where the average is over the crater surface, not z or t . Solving this equation requires that:

$$\overline{T^4} = (\overline{T})^4 \tag{VII-2}$$

giving the equation for the average temperature as:

$$\sigma \ (\overline{T})^4 = \frac{A_c}{A_a} \quad \frac{d\overline{T}}{dz} \tag{VII-3}$$

Evaluating the reradiation flux also requires that $\overline{T^4} = (\overline{T})^4$. From Eq. 18 in the text the reradiation is:

$$f_r = C\sigma \ \overline{T^4} = C\sigma(\overline{T})^4 \tag{VII-4}$$

To show that the equality in Eq. VII-2 is justified, we consider the first of the lunation temperature profiles shown in Fig. 25b, since it can be considered the most extreme case. Obviously Eq. VII-2 is

true for a constant temperature throughout the crater, which is the last of the profiles in Fig. 25b. We will approximate the temperature distribution by taking 10% of the crater area at 180° K and 90% at 140° K, as shown in Fig. 36. The average temperature is then:

$$\bar{T} = 0.1\ (180^{\circ}) + 0.9\ (140^{\circ}) = 144^{\circ}\ K \qquad \text{(VII-5)}$$

The average fourth power of the temperature is:

$$\overline{T^4} = 0.1\ (180)^4 + 0.9\ (140)^4 = 4.5 \times 10^8$$

$$(\overline{T^4})^{\frac{1}{4}} = 145.7^{\circ} \qquad \text{(VII-6)}$$

Thus in making the approximation in Eq. VII-2 , we have made an error of 1.7° in the fourth root of the average fourth power of the temperature. Such an error enters into the reradiation term of Eq. 22c. It will cause less than 1° K error in the final temperature determined for a point since the reradiation term is the same size as the conduction term. Therefore, the approximation $\overline{T^4} = (\bar{T})^4$ is sufficiently valid for our calculations of crater cooling.

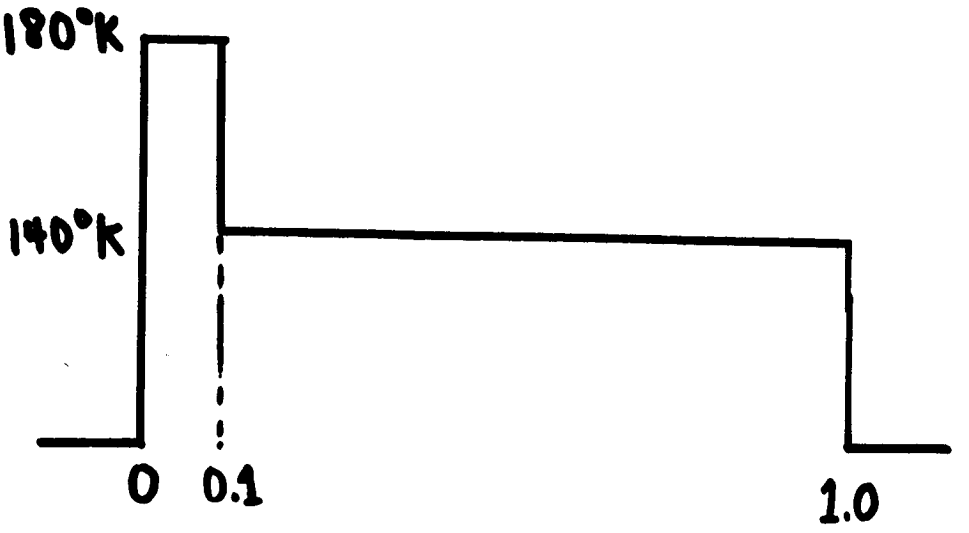

FIG. 36. Temperature approximation

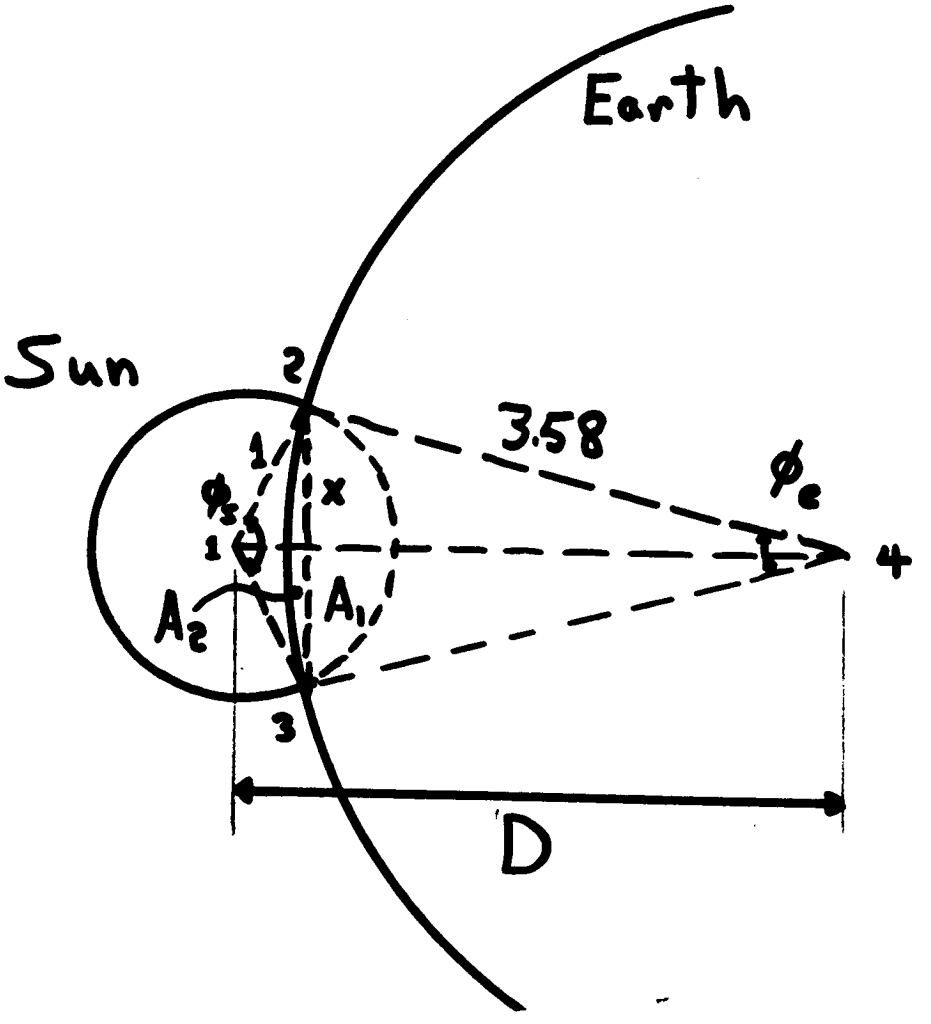

FIG. 37. Geometry of an eclipse

APPENDIX VIII — Eclipse Illumination Function

The geometry of an eclipse is shown in Fig. 37. The radius of the earth as seen from the moon is 3.58 times the radius of the sun. Therefore, totality lasts for a motion of the sun equal to 3.58 solar diameters. In addition, part of the sun is obscured by the earth for $\frac{1}{2}$ a diameter on either side of totality. The amount of solar disc visible during this period can be calculated by considering the amount of obscured area to the left and right of the dotted line in Fig. 37. The area on the right is just the area of the pie-shaped section of the solar disc minus the triangular area 1 — 2 — 3.

$$A_1 = \pi r^2 \left(\frac{\phi_s}{2\pi}\right) - \tfrac{1}{2}\left(2 r^2 \cos\frac{\phi_s}{2} \sin\frac{\phi_s}{2}\right)$$

$$A_1 = \tfrac{1}{2}\left(\phi_s - \sin\phi_s\right) \qquad \text{(VIII-1)}$$

Similarly the obscured area on the left is

$$A_2 = \pi r^2 \left(\frac{\phi_e}{2\pi}\right) - \tfrac{1}{2}\left(2 r^2 \cos\frac{\phi_e}{2} \sin\frac{\phi_e}{2}\right)$$

$$A_2 = \frac{(3.58)^2}{2}\left(\phi_e - \sin\phi_e\right) \qquad \text{(VIII-2)}$$

The two angles are related by the common side, which is shown dotted in Figure 37

$$x = \sin\frac{\phi_s}{2} = 3.58 \sin\frac{\phi_e}{2} \qquad \text{(VIII-3)}$$

The angle ϕ_s can be obtained from the law of cosines, which gives

$$(3.58)^2 = 1 + R^2 - 2R \cos \frac{\phi_s}{2}$$

$$\cos \frac{\phi_s}{2} = \frac{1 - (3.58)^2 + R^2}{2R} \qquad \text{(VIII-4)}$$

where the variation of R (in solar radii) is given by the rate of motion of the Sun. Expressed in solar diameters, Eq. VIII-4 is:

$$\cos \frac{\phi_s}{2} = \frac{1 - (3.58)^2 + 4D^2}{4D} \qquad \text{(VIII-5)}$$

where D changes at the rate of 0.954 solar diameters per hour.

The amount of flux incident on the subsolar point is the solar constant times the fraction of area visible around the Earth. The total area of the disc is π:

$$f_e = f_s \frac{1}{\pi} (\pi - A_1 - A_2)$$

$$f_e = f_s \left[1 - \frac{1}{2\pi} (\phi_s - \sin \phi_s) - \frac{(3.58)^2}{2\pi} (\phi_e - \sin \phi_e) \right] \qquad \text{(VIII-6)}$$

This, together with Eqs. VIII-3 and -5, can be used to obtain the variation in the eclipse illumination.

REFERENCES

Baldwin, R.B. The Measure of the Moon. The University of Chicago Press, Chicago, 1963.

Baldwin, R.B. The Crater Diameter-Depth Relationship from Ranger VII Photographs, Astron. J., 70, 545-547, 1965.

Bastin, J.A. Lunar Hot Spots, Nature, 207, 1381-1382, 1965.

Bennet, A.L. The Photovisual Investigation of the Brightness of 59 Areas on the Moon, Astrophys. J., 88, 1-26, 1938.

Brinkmann, R.T. Lunar Crater Distribution from the Ranger VII Photographs, J. Geophys. Res., 71, 340-342, 1966.

Brown, H. The Density and Mass Distribution of Meteoritic Bodies in the Neighborhood of the Earth's Orbit, J. Geophys. Res., 65. 1679-1683, 1960.

Evans, J.V., and G.H. Pettengill. The Scattering Behavior of the Moon at Wavelengths of 3.6, 68, and 784 Centimeters, J. Geophys. Res., 68, 423-447, 1963.

Fudali, R.F. Implications of the Nonuniform Cooling Behavior of the Eclipsed Moon, Icarus, 5, 536-544, 1966.

Gault, D.E., W.L. Quaide, and V.R. Oberbeck. Luna IX Photographs: Evidence for a Fragmental Surface Layer, Science, 153, 985-988, 1966.

Gear, A.E., and J.A. Bastin. A Corrugated Model for the Lunar Surface, Nature, 196, 1305, 1962.

Glaser, P.E., and A.E. Wechsler. Small-Scale Structure of the Lunar Surface, Icarus, 4, 104-105, 1965.

Hapke, B., and H. Van Horn. Photometric Studies of Complex Surfaces, with Applications to the Moon, J. Geophys. Res., 68, 4545-4570, 1963.

Hapke, B. A Theoretical Photometric Function for the Lunar Surface, J. Geophys. Res., 68, 4571-4586, 1963.

Harris D. L. Planets and Satellites. The University of Chicago Press, Chicago, Ch. 8, 1961.

Jaffe, L.D. Lunar Dust Depth in Mare Cognitum, J. Geophys. Res., 71, 1095-1103, 1966.

Kuiper, G.P., R.G. Strom, K.S. LePoole, and E.A. Whitaker. Russian Luna IX Pictures: Provisional Analysis, Science, 151, 1561-1563, 1966.

Low, F.J. Lunar Nighttime Temperatures Measured at 20 Microns, Astrophys. J., 142, 806-808, 1965.

Minnaert, M. Photometry of the Moon, Planets and Satellites. The University of Chicago Press, Chicago, Ch. 6, 1961.

Murray, B.C., and R.L. Wildey. Surface Temperature Variations During the Lunar Nighttime, Astrophys. J., 139, 734-750, 1964.

Oetking, P. Photometric Studies of Diffusely Reflecting Surfaces with Applications to the Brightness of the Moon, J. Geophys. Res., 71, 2505-2515, 1966.

Orlova, N.S. Photometrical Relief of the Lunar Surface, Astron. Zurn., 33, 93-100, 1956.

Pettengill, G.H., and J.C. Henry. Radar Measurements of the Lunar Surface, The Moon. Academic Press, London, 1962a.

Pettengill, G.H., and J.C. Henry. Enhancement of Radar Reflectivity Associated with the Lunar Crater Tycho, J. Geophys. Res., 67, 4881-4885, 1962b.

Pettit, S.B., and E. Nicholson. Lunar Radiation and Temperatures, Astrophys. J., 71, 102-135, 1930.

Pettit, S.B. Radiation Measurements on the Eclipsed Moon, Astrophys. J., 91, 408-420, 1940.

Piddington, J.H., and H.C. Minnett. Microwave Thermal Radiation from the Moon, Australian J. Sci. Res., 2, 63-77, 1949.

Rackham, T.W. A Note on Lunar Ray Systems, Icarus, 4, 544-546, 1965.

Rea, D.G., and W.J. Welch. The Reflection and Emission of Electromagnetic Radiation by Planetary Surfaces and Clouds, Space Sci. Res., 2, 558-617, 1963.

Rea, D.G., N. Hetherington, and R. Mifflin. The Analysis of Radar Echoes from the Moon, J. Geophys. Res., 69, 5217-5223, 1964.

Saari, J.M., and R.W. Shorthill. Thermal Anomalies on the Totally Eclipsed Moon of December 19, 1964, Nature, 205, 964-965, 1965.

Saari, J.M., and R.W. Shorthill. Isotherms of Crater Regions on the Illuminated and Eclipsed Moon, Icarus, 2, 115-136, 1963.

Shorthill, R.W., H.C. Borough, and J.M. Conley. Enhanced Lunar Thermal Radiation During a Lunar Eclipse, Publs. Astron. Soc. Pacific, 72, 481-485, 1960.

Shorthill, R.W., and J.M. Saari. Nonuniform Cooling of the Eclipsed Moon: A Listing of Thirty Prominent Anomalies, Science, 150, 210-212, 1965.

Sinton, W.M. Physics and Astronomy of the Moon. Academic Press, New York, Ch. 11, 1962.

Sitinskaja, N.N., and V.V. Shavonov. Uc. Zap. Leningrad-Gosudarst Univ., No. 153, 114, 1952.

Troitsky, V.S. Radio Emission of the Moon, Its Physical State, and the Nature of Its Surface, The Moon. Academic Press, London, 1962.

Troitsky, V.S. Investigation of the Surfaces of the Moon and Planets by the Thermal Radiation, Radio Science, 69D, 1585-1612, 1965.

Van Diggelen, J. Photometric Properties of Lunar Crater Floors, Rech. Astron. Observ. Utrecht, 14, No. 2, 1960.

Warren, C.R., Surface Material of the Moon, Science, 140, 188-190, 1963.

Welch, W.J., D.D. Thornton, and S. Winter. The Variation of Lunar Radio Emission During an Eclipse, J. Geophys. Res., 70, 2793-2798, 1965.

Wesselink, A.J. Heat Conductivity and Nature of the Lunar Surface Material, Bull. Astron. Insts. Netherlands, 10, 351-363, 1948.

Winter, D.F. Transient Radiative Cooling of a Semi-Infinite Solid with Parallel-Walled Cavities, Boeing Document D1-82-0449, 1965.

Winter, D.F. Note on the Nonuniform Cooling Behavior of the Eclipsed Moon, Icarus, 5, 551-553, 1966.